Tampere University

PAXTON JUUTI

Development of Aerosol Measurement and Synthesis Technology for Functional Materials

Tampere University Dissertations 113

Tampere University Dissertations 113

PAXTON JUUTI

Development of Aerosol Measurement and Synthesis Technology for Functional Materials

ACADEMIC DISSERTATION
To be presented, with the permission of
the Faculty of Engineering and Natural Sciences
of Tampere University,
for public discussion in the Auditorium SA203 (S2)
of the Sähkötalo Building, Korkeakoulunkatu 3, 33720 Tampere,
on the 13th of September 2019, at 12 o'clock.

ACADEMIC DISSERTATION
Tampere University, Faculty of Engineering and Natural Sciences
Finland

Responsible supervisor and Custos
Professor
Jyrki Mäkelä
Tampere University
Finland

Supervisor
Professor
Jorma Keskinen
Tampere University
Finland

Pre-examiners
Docent
Anna Lähde
University of Eastern Finland
Finland

Doctor of Science (Technology)
Christof Asbach
Institute of Energy and Environmental Technology
Germany

Opponent
Associate professor
Maria Messing
Lund University
Sweden

Cover design: Roihu Inc.

ISBN 978-952-03-1209-1 (print)
ISBN 978-952-03-1210-7 (pdf)
ISSN 2489-9860 (print)
ISSN 2490-0028 (pdf)
http://urn.fi/URN:ISBN:978-952-03-1210-7

PunaMusta Oy – Yliopistopaino
Tampere 2019

Abstract

Nanomaterials are used widely for their improved material properties, compared to bulk, and there are multiple ways of manufacturing them. Aerosol methods are versatile and up-scalable, making them one of the most promising routes to produce contaminant free nanomaterials. As more sophisticated applications emerge, the precise control over the whole process becomes more necessary. The process steps are interlinked in the sense that altering the precursor can have profound effects on the performance of the final application and without measurements, it is hard to say what changes actually took place. This thesis considers the whole synthesis process of generating nanoparticles in gas phase and presents not only new results that improve different steps in this process, but also functionalized surfaces, prepared by depositing nanoparticles made with flame aerosol generation method.

One big problem in nanoparticle synthesis, when spraying is involved, is the generation of residual particles that consume most of the produced mass, decreasing the number of nanoparticles produced. The generation process was optimized by tuning the precursor solution to increase the heat of combustion, which enables the evaporation of the residual particles. This process was characterized with aerosol instrumentation and the absence of residual particles verified with gravimetric analysis and electron microscopy. Structural information was gained by measuring the effective density of the generated particles. Building upon the usefulness of the density measurement, a new sensor-type instrument, density monitor (DENSMO) was developed. Here it is presented for synthesis monitoring purposes. The density of particles is monitored during synthesis to evaluate the stability of the system as well as characterize the shape of the generated particles. Further tuning of the produced nanoparticles' morphology is conducted with real-time monitoring.

Two kinds of surface functionalization were achieved with the deposition of nanoparticles: anti-icing and anti-bacterial. The anti-icing surface was accomplished with a slippery liquid-infused porous surface (SLIPS) structure, where a silicone oil is held on the surface by a porous nanoparticle layer. The wetting behavior of the surface can also be changed with this kind of coating. The produced SLIPS is shown to exhibit excellent anti-icing performance. The anti-bacterial coating is implemented on a fiber filter by the deposition of silver nanoparticles. The performance of the prepared material is tested against *Staphylococcus aureus* and *Escherichia coli* bacteria. Further optimization on the anti-bacterial property is required in order to eradicate the *S. aureus* bacteria, but the material here was quite effective against *E. coli*, showing the viability of the presented method. The utilized methods are tunable and scalable, therefore these results create a foundation for countless options for future materials and applications.

Preface

The work for this thesis was started in 2015 at the Aerosol Physics Laboratory of Tampere University of Technology (TUT) and was finalized in Tampere University. First, I would like to thank Prof. Jyrki Mäkelä for seeing something in me and hiring me in the beginning of my studies to be a part in the synthesis group, and guiding me through the academic world to this point. Second, I thank Prof. Jorma Keskinen for letting me learn all about instrumentation, for affecting my view of the world and for the entire laboratory. Furthermore, I thank the pre-examiners for giving this thesis the final touch and setting my mind at ease. This work would not have been possible without the gracious funding I have received from TUT's graduate school, EU funded projects BUONAPART-E and caLIBRAte, TEKES project ROLLIPS and travel grants from the Finnish Foundation for Technology Promotion (TES) and Emil Aaltonen foundation.

I have had the privilege to work with highly skilled people, without whom this work would not have been possible. Special thanks go to Dr. Juha Harra, who taught me the basics of practically everything aerosol related and is still the quality standard of academic writing for me. Mr. Janne Haapanen I want to thank for the introduction to flame synthesis, as well as for the countless hours spent cutting and coating all manner of materials that do not feel so long in retrospect. Dr. Anssi Arffman I want to thank for the spark for inventions and for the measurement trips that went without a single problem. I thank Dr. Antti Rostedt for showing how things should be done and demystifying electronics. Mr. Miika Sorvali and Mr. Markus Nikka I thank for invaluable help in the laboratory and for the extended discussions and debates during the years. Also, a thank you goes to all of the Aerosol Physics Laboratory personnel who make the work environment as welcoming and supporting as it is. I thank Prof. Takafumi Seto for inviting me to his laboratory in Kanazawa, where I learned a lot about air filtration and international collaboration. The people of former Department of Materials Science and Physics workshop are acknowledged for being paramount in the success of this work, instrument development and material characterization would not have been possible without you.

For the relentless support and encouragement since the beginning, I want to thank my family. You have given me the foundation that has led me where I am now. I thank my friends for dragging me to experience life outside of studies and work, you know who you are. Last, but definitely not least, I thank my wife Sanni for pushing me to do better and keeping me and my work on this side of insanity.

Tampere, July 2019
Paxton Juuti

Contents

Symbols and abbreviations

Ag	Silver
Al_2O_3	Aluminium oxide, Alumina
AMD	Aerodynamic median diameter
APS	Aerodynamic particle sizer
CAT	Centrifugal adhesion test
CMD	Count median diameter
CPC	Condensation particle counter
DENSMO	Density monitor
DLPI	Dekati low pressure impactor
DMA	Differential mobility analyzer
DOS	Dioctyl sebacate
EHA	Ethyl hexanoic acid
ELPI	Electrical low pressure impactor
ESP	Electrostatic precipitator
FCUP	Faraday cup electrometer
GMD	Geometric mean diameter
GSD	Geometric standard deviation
LFS	Liquid flame spray
LPI	Low pressure impactor
MOUDI	Multiple orifice uniform deposition impactor
NaCl	Sodium chloride
NSAM	Nanoparticle surface area monitor
QCM-MOUDI	Quartz crystal microbalance MOUDI
ROS	Reactive oxygen species
SCAR	Single charge aerosol reference
SEM	Scanning electron microscope
SLIPS	Slippery liquid infused porous surface
SMPS	Scanning mobility particle sizer
TEM	Transmission electron microscope
TEOM	Tapered element oscillating microbalance
TiO_2	Titanium dioxide, Titania
TTIP	Titanium tetraisopropoxide
UV	Ultraviolet
WCA	Water contact angle
WSA	Water sliding angle

η	Gas viscosity
$\eta(d_a)$	Collection efficiency of low pressure impactor
$\eta(d_b)$	Collection efficiency of mobility analyzer
χ	Shape factor
λ	Mean free path
ρ_{eff}	Effective density
ρ_0	Unit density
ρ_g	Gas Density
ρ_p	Particle density
A	Area
B	Mechanical mobility
C_c	Cunningham's slip correction factor
C_D	Drag coefficient
d	Diameter
d_{pp}	Primary particle size
d_a	Aerodynamic diameter
d_b	Mobility diameter
d_f	Fractal dimension
d_s	Stokes diameter
D	Diffusion coefficient
e	Elementary charge
E	Electric field
F_{Th}	Thermophoretic force
F_D	Drag force
F_E	Electric force
F_g	Gravitational force
g	Gravitational acceleration
H	Coefficient for thermal force
k	Boltzmann's constant
L	Length
m	Mass
n	Number of charges
N	Number of particles
n_{ave}	Average charge (effective charge)
p	Gas pressure
P	Penetration
p_s	Saturation vapor pressure
Pn	Penetration and charging efficiency
S	Stopping distance
S_R	Saturation ratio
T	Temperature
U	Collection voltage
v	Velocity
v_{TS}	Settling velocity
v_0	Initial velocity
V	Volume
Z	Electrical mobility

List of publications

The following four scientific journal articles are part of this compound thesis. The author collaborated in the making of these publications and takes credit only on the parts that the author was responsible for. These publications are cited based on their labels below.

Paper I Juuti, P., Arffman, A., Rostedt, A., Harra, J., Mäkelä, J.M. and Keskinen, J., "Real-time effective density monitor (DENSMO) for aerosol nanoparticle production," *Aerosol Science and Technology*, 50:5, 487 – 496, 2016.

Paper II Harra, J., Kujanpää, S., Haapanen,. J., Juuti, P., Hyvärinen, L., Honkanen, M. and Mäkelä, J.M., "Aerosol analysis of residual and nanoparticle fractions from spray pyrolysis of poorly volatile precursors," *AIChE Journal*, 63:3, 881 – 892, 2016.

Paper III Juuti, P., Haapanen, J., Stenroos, C., Niemelä-Anttonen, H., Harra, J., Koivuluoto, H., Teisala, H., Lahti, J., Tuominen, M., Kuusipalo, J., Vuoristo, P. and Mäkelä, J.M., "Achieving a slippery, liquid-infused porous surface with anti-icing properties by direct deposition of flame synthesized aerosol nanoparticles on a thermally fragile substrate," *Applied Physics Letters*, 110, 161603, 2017.

Paper IV Juuti, P., Nikka, M., Gunell, M., Eerola, E., Saarinen, J.J., Omori, Y., Seto, T. and Mäkelä, J.M., "Fabrication of fiber filters with antibacterial properties for VOC and particle removal," *Aerosol and Air Quality Research*, 19:, 1892 – 1899, 2019.

Author's contribution

The author's contributions on these four collaborated research papers are listed below.

Paper I The author collaborated on the instrument design and made optimizations to the structure based on the initial calibration measurements, which were also done by the author. All of the test and calibration aerosols were synthesized by the author. The data analysis and manuscript preparation was also done by the author.

Paper II This publication has two main points: the reduction of residual particles and the gravimetric analysis of the mass-size distribution. The author was responsible for the synthesis of the alumina and silver particles, as well as the optimization of the ethylhexanoic acid content. The powder sample collection for the SEM imaging and the effective density calculations were also done by the author. Lastly, the author collaborated in the writing of the article.

Paper III The LFS coatings and the preparation of the SLIPS structure were produced by the author. Data analysis and the measurement of the water contact angle and the water sliding angle were done by the author. Most of the publication was written by the author.

Paper IV The filter structures were designed by the author in collaboration with the co-authors. Particle penetration and methanol adsorbtion measurements and silver nanoparticle coating with real-time monitoring were done by the author. Data analysis from all of the measurements were done by the author, who also wrote most of the publication.

1 Introduction

Nanoparticles are building blocks for new cutting-edge materials, and the use of nanoparticles in the last ten years has seen exponential growth. The benefits of using nanometer-sized subdivisions of materials have been known since antiquity (Sciau, 2012) and there are still many common use cases that date back decades, the most notable possibly being white pigment titania (Maile et al., 2005) and carbon black used in tires (Stark et al., 2015). As the understanding and know-how of material properties in nano-scale have increased, so have the applications and production volumes. Now almost every industry enjoys the benefits of nanomaterials. (Aitken et al., 2006)

The performance of nanoparticles is obviously linked to the substance that it is made out of, but interestingly the size of the material unit has a big impact on it as well. For example, catalyst materials in car exhausts see a decrease in conversion rates as they age, which can be credited to the diffusion of material and thus the increase of particle size of palladium or platinum nanoparticles on its surface. Bigger particles mean less surface area for chemical reactions. (Honkanen et al., 2016) This is a case where the property already exists in bulk, but is increased when there is more surface area. However, shrinking materials to nano-scale can have drastic impact on the properties that we are familiar with. In the case of water suspension of gold nanoparticles, the color of the liquid is determined by the size of the nanoparticles (Zheng et al., 2004).

This process of altering properties can be advantageous as the changed properties can be very useful and wanted, but it poses some new questions. Say, if we want a certain property from a nanomaterial that manifests in 10 nm, we must answer the question of how this material can be produced with precision and repeatability. One answer to this is to utilize gas phase synthesis and the many processes that come with it. By producing nanomaterials in the gas phase, the end result is an aerosol where the individual particles are suspended in the selected gas. After this, there are many ways to manipulate and alter the shape and size of the produced particles, still in the gas phase, and then direct them where they are needed. This process facilitates the manufacturing of powders (Pratsinis, 1998; Stark and Pratsinis, 2002; Strobel et al., 2006), coatings (Brobbey et al., 2017; Haapanen et al., 2015; Harra et al., 2012), quantum dots (Didenko and Suslick, 2005; Heath et al., 1994) and many other materials for wide range of applications.

The characterization of the produced materials is an important step in the synthesis process. In the case of aerosol nanoparticles, the characterization can be done in the gas phase or after their deposition with offline methods. There are numerous different aerosol instruments that are capable of measuring the properties of nanoparticles, ranging from the size and shape to the chemical composition. Most commonly used instruments are particle counters and spectroscopic measurement devices, which give information on the concentration and the number size distribution of the particles, respectively. On

the other hand, chemical composition is measured with e.g. SP-AMS (single particle aerosol mass spectrometer (Onasch et al., 2012)) and APi-ToF (atmospheric pressure interface time of flight mass spectrometer Tofwerk AG). For monitoring purposes, simpler sensor-type instrumentation are widely used. These include air-quality and personal exposure assessment applications (Bhattacharya et al., 2012; Steinle et al., 2015). Offline characterization of nanoparticles typically employs established material analysis methods from gravimetric analysis to electron microscopy. The online methods are unbeatable when it comes to real-time capabilities, but if the structure of the generated nanoparticles is under investigation, studying individual particles with electron microscopy is the way to go. Crystal structure, multicomponent material distribution and hollowness are just a few examples of what can be measured (Cui et al., 2013; Guo et al., 2009; Sun et al., 2012). In synthesis of aerosol nanoparticles, there is a trade-off between the quickness of the analysis method and the available information, which brings its own challenge into the process.

The concept of ”product by process” (Kutsovsky, 2018) is a recent one in aerosol synthesis, where the process parameters and its scale are linked to the performance of the produced nanomaterial. This implies that there is a need to understand and measure the effects of different process parameters, if better performing materials are desired to be synthesized. Up until now, it seems that just producing materials with higher and higher throughput, but which perform "well enough”, has been sufficient. The whole process from selecting the precursor and generation method to synthesizing the nanoparticles and finally incorporating them to different applications is increasingly important, as more demanding applications emerge.

This thesis comprises of a summary of five chapters and four appended scientific research papers. After this introduction, Chapter 2 covers the measurement and manipulation of the nanoparticles in the gas phase, as well as gathers the properties of nanoparticles relevant to this thesis. Chapter 3 focuses on the synthesis of nanoparticles from solid and liquid phase starting points, including generators that are used to achieve this. After this the deposition mechanisms from gas phase to surfaces is discussed. Also, the three application areas of this thesis: instrument development, synthesis tuning and surface functionalization, are linked to the relevant broader subject. These theme areas are then carried over to the result section of Chapter 4. The last portion of this thesis then gathers the conclusions and presents some future outlook in Chapter 5.

1.1 Aim and scope

The purpose of this thesis is to provide new information, building upon the general understanding of the whole nanoparticle synthesis process in gas phase from precursors to applications. An integral part of this process is also the measurement of the synthesized nanoparticles. The results of this thesis focus on the the following objectives:

- Development of measurement techniques to characterize nanoparticles during the synthesis process
- Tailoring the size and morphology of aerosol nanoparticles by exploiting temperature-dependent properties of materials
- Applying specifically made nanoparticles for instrument calibration in the gas phase and for surface functionalization

Instrument development for aerosol nanoparticle sythesis monitoring is done in **Paper I**, where a new density monitor (DENSMO) is introduced. DENSMO is utilized as a monitor in the synthesis process of **Paper IV**, in conjunction with a SMPS-ELPI method, both relying on the same fundamental approach. The complementary method is also used in the measurements of **Paper II**.

The aerosol nanoparticle size and morphology is controlled in **Paper I**, where instrument calibration requires the synthesis of nanoparticles in a wide size range. The precise knowledge of the shape and density is also vital in this application. In **Paper II**, the volatility of the used precursor is increased to suit the available flame temperature, which increases the amount of nanoparticles produced in the process. The formation process of nanoparticles in elevated temperatures is interrupted in **Paper III**, where a thermally fragile surface is coated with nanoparticles, producing a highly porous metal oxide layer. Individual and spherical silver nanoparticles are produced in **Paper IV**, where flame-generated nanoparticles are sintered in a residence tube.

Nanoparticles with effective densities ranging from 0.9 to 10.5 g/cm^3 are produced in **Paper I**, where they are used in the instrument calibration and verification of operation. Highly porous surface coating is achieved in **Paper III** by utilizing the agglomerated structure of titania nanoparticles. In **Paper IV**, anti-bacterial effect is introduced to a fiber filter material by coating it with silver nanoparticles and the filtration efficiency is exploited by synthesizing particles that readily diffuse.

2 Measurement of nanoparticles in gas phase

2.1 Properties of airborne particles

There are many properties defining the structure and behavior of nanoparticles. Properties covering the structure determine what the nanoparticle looks like and what material properties it has. Properties that are dependent on the surroundings, on the other hand, describe how the nanoparticle behaves in relation to e.g. external forces. Table 2.1 shows a list of these properties, which will be discussed in this chapter. In addition to single particle properties, there are ones that describe a whole population of nanoparticles as a distribution. Average and statistical values can be determined to the distribution to assist in the handling of large number of particles at once, which most still stem from the individual particle properties discussed in this chapter.

Table 2.1: A list of properties defining nanoparticles and examples of instruments used for the their characterization. The dependencies show what other more fundamental parameters can be used to calculate them.

Property	Symbol	Equation	Dependensies	Instrument example
Area	A	$\frac{\pi}{2}d_p^2$	d_p	NSAM
Charge number	n	—	—	FCUP
Density	ρ	m/V	d_p, V, m	DENSMO
Diameter	d_p	—	—	SMPS
Electrical mobility	Z	neB	d_p, n	DMA
Fractal dimension	d_f	—	V, m, d_{pp}	—
Mass	m	ρV	d_p, ρ, V	TEOM
Mechanical mobility	B	$\frac{C_c}{3\pi\eta d_p}$	d_p	—
Number	N	—	—	CPC
Primary particle size	d_{pp}	—	—	TEM
Settling velocity	v_{TS}	$\frac{\rho d_p^2 g C_c}{18\eta}$	d_p, B, ρ	—
Stopping distance	S	Bmv_0	d_p, B, m, ρ	APS
Volume	V	$\frac{\pi}{6}d_p^3$	d_p	—

The most intuitive of physical properties are the ones relating to the geometry of the nanoparticles. These include surface area A, volume V and number N, which can be linked together if we consider spherical nanopartricles with a diameter d_p. Considering individual particles, the number of particles is trivially just one. The number of particles, as a property, has more merit when whole distributions are considered. Additionally, estimating nanoparticles as spherical is not completely without merit, as the smallest nanoparticles and the smallest structure units of agglomerates (primary particles, d_{pp})

are often spherical. Agglomerates can thus be estimated to be N number of spherical primary particles with diameters of d_{pp}. The calculations and dependencies are also more straightforward due to this thought process. The actual structure of nanoparticles can also be taken into account later with parameters such as dynamic shape factor χ, which can be used to correct the drag force experienced by non-spherical particles.

Adding density ρ, and with it mass m, into the list, the structure of a spherical nanoparticle can be quite exhaustively described. However, similar mass agglomerates can still vary greatly in structure without having parameters describing them. This time it is useful to consider agglomerates as fractals, where the defining parameter is a (mass) fractal dimension d_f, which tells to what power the mass of the agglomerate depends on the distance from the center-of-mass of the given agglomerate. This parameter can have a value ranging from 1 to 3, for e.g. a fiber of length L and a sphere with a diameter d_p respectively. The fractal dimensions of agglomerates are typically around 2, but vary greatly based on the material and synthesis method (Bushell et al., 2002). Given the formation process of nanoparticles, the density as a function of the particle diameter can be related to the fractal dimension with the following equation

$$\rho(d_p) \propto d_p^{d_f - 3}, \tag{2.1}$$

(DeCarlo et al., 2004) where the proportionality depends on the bulk density of the material and the primary particle size, the first defining the maximum density achievable and the second defining the point after which the density starts to drop with a slope defined by the fractal dimension (Skillas et al., 1998; Virtanen et al., 2004). How the particle formation dictates the structure of the agglomerates will be discussed in the next chapter.

Lastly, there is charge n, which enables the electric properties of nanoparticles, but which in itself is a physical property. The charge of a nanoparticle is always a multiple of the elementary charge, thus the charge state of nanoparticles is denoted with a whole number factor with a sign denoting the polarity.

Term "dynamic" links force to motion, so it is only logical to examine what kind of velocity v can be produced by imparting a force on a nanoparticle. If the force in question is gravity, the particle experiences terminal settling velocity v_{TS} in stable conditions. The proportionality factor between these two parameters is called the mechanical mobility B, which is inversely related to the particle diameter. The mechanical mobility is also the link between the stopping distance S of a particle with an initial velocity of v_0 (Hinds, 1999).

Similar to, and based on, the mechanical mobility is the electrical mobility Z, which this time links electrical force to the movement of the nanoparticle. The value of electrical mobility can be calculated by multiplying the mechanical mobility by the charge of the nanoparticle, meaning the friction force is the same in both situations but the driving force is multiplied by the electric interaction.

All of these have been properties of individual particles. Most often than not, nanoparticles are not found alone, but in large quantities that interact dynamically. Deposition and agglomeration, among many other processes, shape the overall aerosol so that the number of particles as a function of their diameter follows a typical shape, called log-normal distribution. The analysis of aerosol particles as units of a distribution helps in calculations, as distribution-based parameters can be used to describe the the whole ensemble: count

median diameter (CMD), total number of particles (N) and geometric standard deviation (GSD).

The main property of nanoparticles relevant to this thesis is the particle density that has been measured in **Paper I**, **Paper II** and **Paper IV**. The measured density has enabled the determination of the structure of the produced nanoparticles, as well as worked as a link to the nanoparticle mass concentration. Particle diameter has been determined in all of the papers with online and offline methods.

2.2 Manipulating particle size distributions

As many of the properties of nanoparticles are a function of size, it is desirable to be able to select a specific portion of the whole nanoparticle distribution. Electrical and inertial classifications are the two most common ways to achieve this. If, however, all or most of the particles need to be collected for later use or for cleaning air flows, filtration is typically used. Figure 2.1 shows four ways to affect a particle number size distribution, which are based on the previously mentioned methods. The simplest way to utilize an

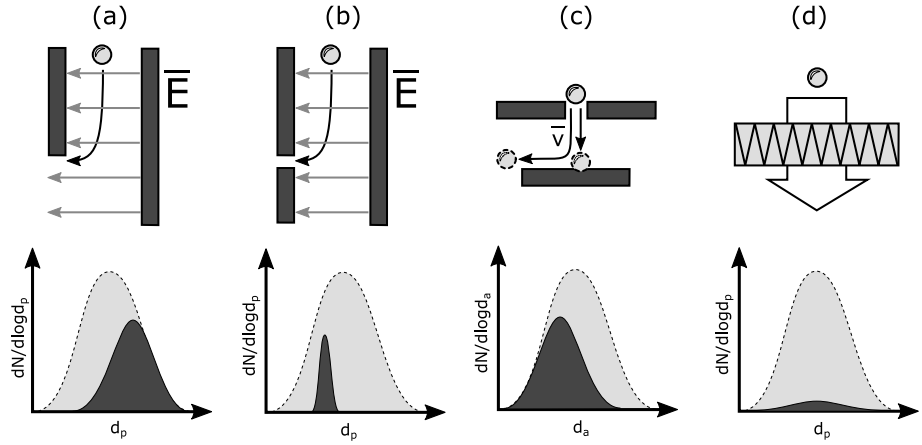

Figure 2.1: Manipulating particles in the gas phase: (a) mobility analyzer, (b) differential mobility analyzer, (c) impactor and (d) filter. The distributions illustrate the effect these manipulations have on the number-size distribution of the initial aerosol particles.

electric field to collect nanoparticles is to have two plates or cylinders with an electrical potential difference between them. Depending on the use case, this setup can be used for mobility analysis (Tammet et al., 2002) or as an electrostatic precipitator (ESP, David and Fraser (1956)). The purpose of ESP is to collect all of the charged particles, while the mobility analyzer collects only a portion of the particles with the highest electrical mobility. If a certain narrow range of electrical mobility is desired to be characterized, a differential mobility analyzer (DMA, Hewitt (1957)) can be used, where one of the electrodes has a small slit that lets the specific particles through. The construction of a DMA is more complex than its simpler counterpart: the addition of a sheat flow that constricts the incoming particles into a tight path improves the resolution of the device. For example, the collection efficiency of a mobility analyzer, $\eta(d_b)$, can be calculated with the following equation

$$\eta(d_b) = \frac{2\pi ZUL}{Qln\frac{r_o}{r_i}}, \tag{2.2}$$

where Q is the flow rate through the mobility analyzer, L the measurement zone length, and r is the radius of the inner or outer cylinder, depending on the subscript.

The particles of interest can be non-charged or of unknown charge, taking electric manipulation off the list. In this case, the particles can be characterized based on their inertia. For example, a low pressure impactor (LPI, Marple and Willeke (1976)) accelerates the incoming gas flow in its nozzle and then bends it rapidly with an obstruction. By designing its geometry carefully, it can be used to collect particles with higher inertia than a certain cutpoint value. However, given too much kinetic energy during the acceleration, the impacted particles can exhibit bouncing from the collection surface (Arffman et al., 2015; Kuuluvainen et al., 2013). The collection efficiency of a low pressure impactor can be expressed with the following equation

$$\eta(d_a) = \left(1 + \left(\frac{d_{50}}{d_a}\right)^{2s}\right)^{-1}, \tag{2.3}$$

where d_{50} is the diameter of a particle corresponding to 50% collection, so-called cutpoint diameter, and s is a steepness parameter for the function (Winklmayr et al., 1990).

Collecting both the largest and the smallest particles at the same time is possible by using a filter. However, depending on the filter design, particles with a size around 100 nm tend to pass through as they have rather small inertia and thus they do not impact easily. Additionally, the size is large enough to warrant poor diffusion. High efficiency filters combat these phenomena with nanoscale fibers that leave smaller gaps for the particles to go through and by increasing the time particles spend inside the filter, thus increasing the change of being collected (Choi et al., 2017).

The manipulation of nanoparticles with an electric field and a low pressure impactor are the bases for the instrument development in **Paper I**. The electrical classification and low pressure impaction are utilized in **Paper I**, **Paper II** and **Paper IV**, where the used measurement instrumentation operate based on these mechanisms. Filtration is used for measurement purposes in **Paper I** and **Paper IV**, and, additionally, for a coating application in **Paper IV**.

2.3 Counting and measuring particles

Online methods

Having successfully selected certain nanoparticles, let's say with a DMA, the next logical step is to count how many particles are being passed through. The number concentration of particles per cubic centimeter of gas can easily vary from a few individual particles to upwards of billions (Friedlander, 1983), depending on the synthesis method and the present dynamics. To measure these kinds of concentrations in real-time, there are three types of methods utilized: charge, optical and oscillation based techniques, which are depicted in Figure 2.2. The charging state of a nanoparticle can be linked to its size and surface area if the used charger is well characterized, like is the case with an electrical low pressure impactor (ELPI, (Keskinen et al., 1992) and ELPI+ (Järvinen et al., 2014)) and nanoparticle surface area monitor (NSAM, Shin et al. (2007)), respectively. The performance of these chargers can be evaluated with e.g. a Pn product, which describes the penetration and charging efficiency. In these instruments, a corona charger is used to get a stable charge distribution. In the case of ELPI, after the charging the particles are deposited onto subsequent impactor stages, where the charge carried by the particles is

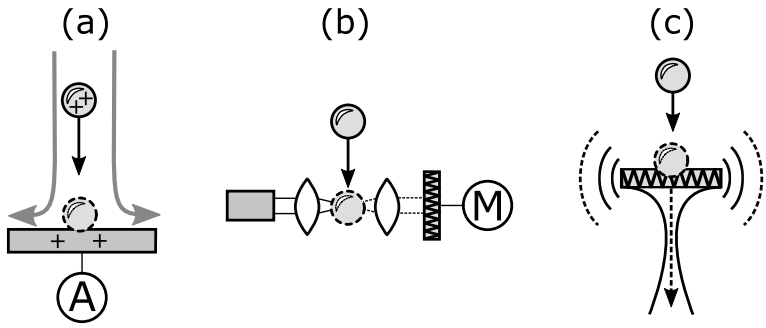

Figure 2.2: Measuring methods for particles: (a) current measurement from impaction, (b) optical counting and (c) mass change of an oscillating filter.

measured. In this manner, the stages give information on the size of the particles, while the measured charge tells about the number of particles measured. Another approach is to produce particles with systems such as a single charge aerosol reference (SCAR, Yli-Ojanperä et al. (2010)), which, as the name implies, generates particles with one unit charge. This is achieved by first synthesizing 10 nm particles that have negligible probability to be multiply charged, which then are grown by condensation to the desired size. Now the charge can be measured with e.g. a Faraday cup electrometer (FCUP, e.g. Liu and Pui (1974)), which is now analogous with the number of measured particles.

Counting the number of particles is also possible with optical methods. At low concentrations, individual particles can be counted as they produce a scatter pulse by crossing a light beam. However, the particles need to be large enough to interact with visible light, so they are generally grown to optically relevant sizes. A condensation particle counter (CPC, Aitken (1888); McMurry (2000)) is an instrument that uses e.g. butanol to grow particles and then counts them. At higher concentrations, multiple particles scatter at the same time, making identification of single pulses difficult. To overcome this, instead of counting pulses, the total scattering intensity is measured, which correlates with the number of particles.

Another way to estimate the particle size is to first size select them with any of the previously mentioned methods and then do the counting with electrical or optical means. An example of this is a scanning mobility particle sizer (SMPS, Wang and Flagan (1990)), which uses a DMA to select particles based on their electrical mobility, scanning over a distribution, and then a CPC to do the counting. Noteworthy in this approach is that there are multiple definitions of particle diameters. If we use the settling velocity as the measured property, we can choose the density and get different diameters with the same velocity. This can be seen in the following equation

$$v_{TS} = \frac{\rho_p d_e^2 g}{18\eta\chi} = \frac{\rho_0 d_a^2 g}{18\eta} = \frac{\rho d_s^2 g}{18\eta}, \tag{2.4}$$

where ρ_p, ρ_0 and ρ are the particle's actual density, density of water (1 g/cm^3) and bulk density, respectively. The diameters corresponding to these densities are the equivalent volume diameter (d_e), the aerodynamic diameter (d_a) and the Stokes diameter (d_s). The aerodynamic diameter is commonly in use, as it can be used to describe the behavior of particles in gas streams without having to know the shape or the density of the particle. ELPI and APS (aerodynamic particle sizer, Baron (1986)) being two examples

of instruments that utilize aerodynamic diameter. There is also a connection between the mobility diameter and the aerodynamic diameter of a particle, namely the effective density, which can be calculated with the following equation

$$\rho_{eff} = \rho_0 \frac{C_C(d_a) d_a^2}{C_C(d_b) d_b^2}. \tag{2.5}$$

To measure the mass of particles online, there are two main ways: measuring the change of an oscillator as its mass changes due to deposited particles, and measuring two dynamic properties that are related by the density of the particle. Instruments such as a quartz-crystal microbalance multiple-orifice uniform-distribution impactor (QCM-MOUDI, Chen et al. (2016)) and a tapered element oscillating microbalance (TEOM, Ruppecht et al. (1992)) utilize the change of oscillation in an impactor stage and in a filter, respectively. Having multiple stages, the QCM-MOUDI gives information on the mass distribution in addition to the mass concentration. The other approach of utilizing dynamic properties to measure the mass of particles is to combine e.g. size and number count information with density. Measuring both aerodynamic and mobility diameters yields information on the density of particles based on the Equation 2.4, which can be done with the parallel usage of e.g. ELPI and SMPS (DeCarlo et al., 2004).

The current measurement is used as the particle detection method in the developed instrument of **Paper I**. Otherwise, all of the three presented counting methods are involved in the operation of the used measurement instruments in **Paper I**, **Paper II** and **Paper IV**.

Instrument development

Almost any aerosol instrument can be used for measuring synthesis processes, given appropriate cooling and sampling lines. However, some particle properties might not be measurable with a single instrument that is commercially or otherwise available to use. Having an understanding on ways to manipulate particles in the gas phase as well as the parameters that need to be measured gives a foundation for instrument development.

The density of particles is one such parameter (Kelly and McMurry, 1992). Measurement of particle density can be done e.g. by combining responses from an electrical mobility device and an aerodynamic diameter measuring device, such as an SMPS and an ELPI (Ristimäki et al., 2002; Virtanen et al., 2004). Taking the basic principles from these instruments, namely mobility analysis and low pressure impaction, comparable information can be gained with a much simpler construction. In **Paper I**, these principles have been utilized in the development of DENSMO. It is important to keep in mind, however, when measuring densities of particles that only spherical particles, such as primary particles, have effective densities equal to the material density. Agglomerates, on the other hand, exhibit lower measured density values than the material density. Distinguishing between spherical and agglomerated particles based on the measured density requires *a priori* information on the produced particles.

Instrument development benefits from controlled particle synthesis, as calibrating instrumentation requires precise knowledge of the particles being measured, size and charge being the most important for instrumentation that relies on the electric detection of particles. Reference sources like SCAR are invaluable in these situations.

Offline methods

The characterization of nanoparticles can be done also after their collection, offline from the main flow of the aerosol. Qualitatively the deposition of particles can be confirmed with visual inspection, if there is a thick enough layer or the coating affects the color of the surface, e.g. through plasmon resonance (Mock et al., 2002). Quantitative information from the collected particles can be gained with e.g. gravimetric analysis and electron microscopy. Filter weighing is probably the most used method to assess the mass of the collected sample of particles, which, however, has noticeable uncertainty in the case of nanoparticles, if the collected mass is small compared to the mass of the filter.

Imaging of nanomaterials can be done with electron microscopy, as the wavelength of visible light is not sufficient to interact with structures in the lower nanometer range. There are two main types of electron microscopes: scanning electron microscope (SEM) and transmission electron microscope (TEM). Both of these imaging techniques rely on the interactions of accelerated electrons with the studied sample. The different interactions electrons can have with matter are depicted in Figure 2.3, with macroscopic and atomic scale.

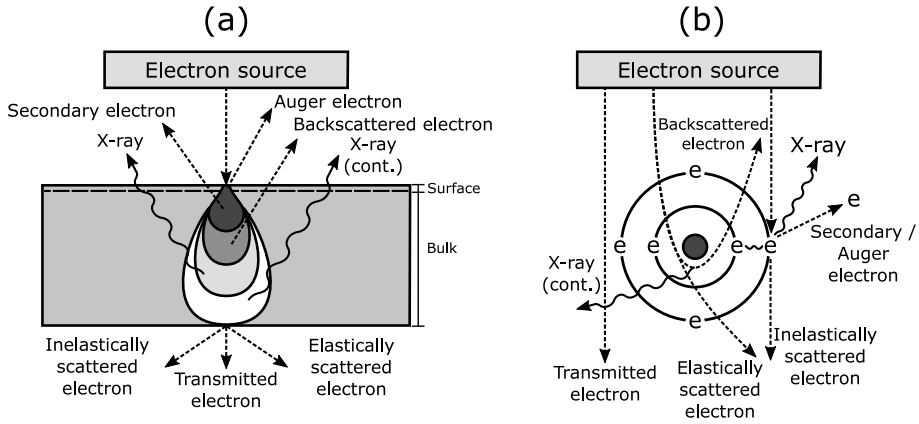

Figure 2.3: Interactions of accelerated electrons with (a) bulk material and (b) individual atom.

TEM mostly utilizes the transmitted electrons and elastically scattered electrons to produce structural information from the imaged sample. In order to have these electrons pass the sample, it has to be thin enough so all of the electrons do not get absorbed. Nanoparticles on purpose-made microscopy grids are ideal for this kind of imaging. SEM on the other hand is more suited for imaging surfaces of thicker samples, like nanoparticle coatings on bulk materials. This is due to SEM typically utilizing backscattered electrons, secondary electrons and auger electrons, which are produced in the sample and can be emitted in almost any angle. These electrons do not have to travel all the way through the sample, but can come back up from the interaction volume they were produced in. Backscattered electrons and secondary electrons are electrons that have been redirected through coulombic repulsion, which also produces continuum X-ray radiation. The incident electrons can also give enough energy during the scattering process to free electrons from the material being imaged, which creates a secondary electron and a hole in the electron structure. If the hole gets filled by an electron from a higher energy level, X-ray photon is then additionally emitted. This X-ray has a probability to be recaptured

by an outer shell electron in the same atom, which in turn gets ejected, creating an auger electron. If the incident electron, coming from the electron source, experiences these inelastic interactions and then passes through the sample, it is considered an inelastically scattered electron. (Hawkes and Reimer, 2013)

In addition to structural information, electron microscopy can be used to analyze chemical composition, as many of the described interactions are dependent on the mass and electron structure of the studied material. Different aspects of the material are studied with different detectors that focus on electrons or X-ray detection. The scanning capability also enables mapping of the chemical composition over a wider area.

The gravimetric analysis is utilized in the detection of residual particles in **Paper II**. Electron microscopy is used to image the produced particles in **Paper II** and the coated surfaces in **Paper III** and **Paper IV**.

3 Synthesis and applications of nanoparticles

3.1 Formation routes and generation of nanoparticles

Producing nanoparticles from bulk materials needs energy. This energy goes into phase changes and creating new surface area by breaking bonds between atoms and molecules in the solid or liquid phase structure of the bulk material. Schematic of phase transitions and routes for nanoparticle formation is depicted in Figure 3.1.

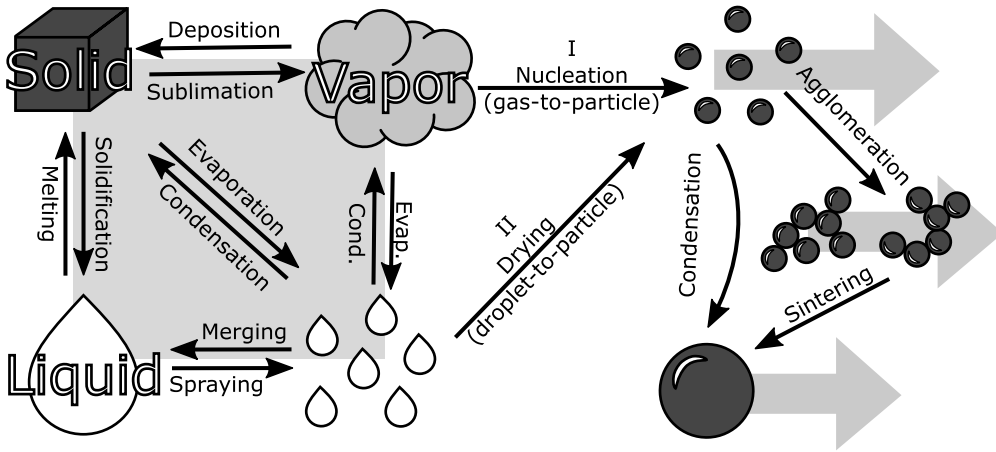

Figure 3.1: The phase and structure changes of materials relevant to the synthesis of nanoparticles in this work. Generation of nanoparticles usually follows the gas-to-particle route. The process temperature generally dictates what phase transitions can happen. After the particle formation, all producible morphologies are utilized in different applications.

When one considers the gas-phase synthesis of nanoparticles, there are two typical ways to introduce bulk material into a carrier gas: as a gas or vapor, and as droplets (Gurav et al., 1993). These require either the spraying of liquid materials or the heating of solid materials. When nanoscale particles are being synthesized, the sprayed droplets at this stage are generally too large and they require further processing. To decrease the size further, the droplets can be evaporated into vapor or dried up to leave a solute residual. However, depending on the concentration of the initial liquid, the residuals can still be in the micron range.

The advantage of getting the material into gaseous phase comes from the bottom-up

approach of growing the nanoparticles from individual atoms into larger particles and structures. At what rate the material can change phase from solid or liquid into gaseous depends on the temperature and the material properties. Generally the material needs to be melted first to get any significant amount of evaporation, after which the saturation vapor pressure p_s of the material keeps increasing exponentially. As an example, the temperature dependency of the vapor pressure of melted silver is given in Equation 3.1 (Alcock et al., 1984).

$$log(p_s) = 5.752 - \frac{13840}{T} \tag{3.1}$$

The vaporized material then has multiple routes to change phase: condensation onto bulk liquid or onto existing liquid and solid particles in the gas phase, deposition onto solid surfaces or, most importantly in the scope of this thesis, nucleating into new particles. The critical parameter governing this process is the saturation ratio S_R, which is defined as the ratio of the partial vapor pressure p to the saturation vapor pressure at the given temperature p/p_s (Fuchs, 1964). The saturation ratio increases if the temperature of the vapor decreases, or if there are chemical changes in the vapor. One example of a chemical change where the saturation vapor pressure decreases significantly is the thermal decomposition of titanium tetra isopropoxide (TTIP) into titanium dioxide, also called titania, which can also be seen in the change of the melting points from $\sim 15^oC$ to 1855^oC (Haynes, 2016).

After the nucleation has taken place, different processes start to change the morphology of the particles. They can grow by condensation with the original vapor or by other condensable vapor, two processes for which terms homogeneous nucleation and heterogeneous nucleation can be used, respectively (Dunning, 1960). Given high enough concentration of particles, they can also grow by forming joined structures through agglomeration, where the individual primary particles are held together with van der Waals forces. The way these agglomerates form affects the fractal dimension, and thus how porous the structure is. These processes range from the loosest packed structure formed by diffusion-limited cluster-cluster agglomeration to the densest packed structure formed by ballistic particle-cluster agglomeration (Schaefer and Hurd, 1990). Further strengthening the structure, the primary particles can sinter together through diffusive mass transfer in elevated temperatures. This sintering process first achieves neck formation, producing chemically bonded aggregates, and at a later stage fully coalesced particles (Koch and Friedlander, 1990).

Particle generators

There are multiple ways of producing nanoparticles that all employ the phase and structure changes discussed above. The devices that produce nanoparticles from bulk material sources are called generators. Here we focus on generators that produce nanoparticles in gas phase, either from solid or liquid precursors. The four generator types used for making nanoparticles in this work are depicted in Figure 3.2.

The first type of generator is a tubular furnace (also known as a hot-wall reactor), which is used for melting and then evaporating e.g. salts (Chen and Chein, 2006) and metals (Harra et al., 2012) placed inside the furnace, or heating materials that are already suspended in the carrier gas. This evaporation-condensation method for these materials was originally developed by Scheibel and Porstendörfer (1983). The advantage of tubular

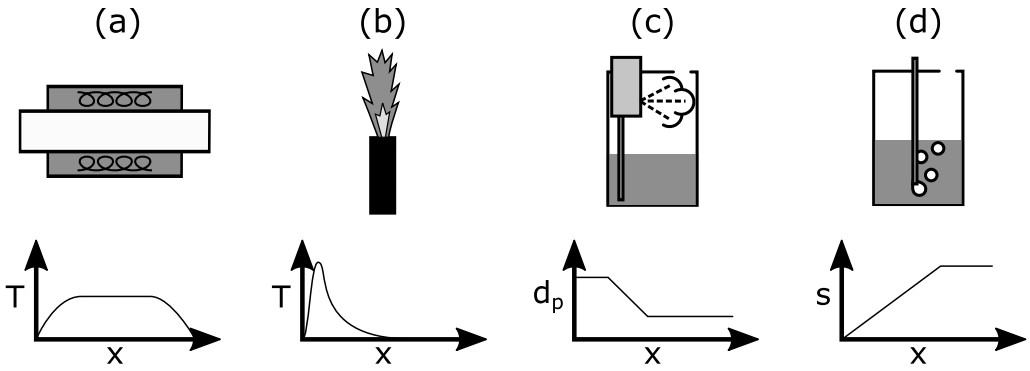

Figure 3.2: Generators used to produce particles from bulk materials: (a) tubular furnace, (b) flame, (c) atomizer and (d) bubbler. Under the generators a key behavior is plotted: (a) & (b) temperature profile, (c) drying of the atomized droplets and (d) saturation of the vapor in the bubbles.

furnaces is the high controllability of the process parameters: temperature, residence time, flow rate and in multizone furnaces even the temperature gradient. The temperature is typically constant in the middle of the furnace with heating and cooling gradients at either ends. Having control over the temperature in the gas flow allows for precise changes in the sintering and production rates. Multicomponent particles can also be made by connecting multiple generators in series.

Another generator type employing high temperatures is a flame generators, of which liquid flame spray (LFS) (Mäkelä et al., 2017; Tikkanen et al., 1997) is one variation, where a hydrogen oxygen flame is the heat source. The gases also function as the means to spray the used liquid precursor into the flame. Single construction design of this generator makes it ideal for scale-up, but high production rates can be achieved even with one generator. The high temperature of the flame ($\sim$ 3000 K) (Pitkänen et al., 2005) can evaporate the precursor, thermally decompose it if applicable, and depending on the produced material, even affect the sintering state of the particles.

Atomizers spray a liquid precursor with the aid of high pressure gas, producing a wide size range of droplets. The largest ones hit the side of the generator and are removed from the gas flow, leaving behind a fine mist. The sprayed droplets can then be dried to leave behind a solute fraction of e.g. salt from liquid solution (Okuyama and Lenggoro, 2003), or the aerosol can be introduced into a tubular furnace to have a similar particle formation route as in the LFS (Mädler, 2004). The latter combination is known as the evaporation condensation generator (Liu and Lee, 1975), where the generation of the particles is achieved with homogeneous nucleation and does not typically involve chemical changes in the produced material.

Volatile precursor vapors can be produced with a bubbler (e.g. Deppert and Wiedensohler, 1994), where gas bubbles are passed through a liquid. The saturation process can involve heating the precursor liquid, if the vapor pressure is not high enough or if increased saturation ratio is wanted. The saturated vapor can then be directed e.g. into a furnace for thermal decomposition or mixed with existing particles to grow them by condensation.

The main route for nanoparticle formation in this thesis is through the vapor phase, which typically produces the smallest particles. In **Paper II**, **Paper III** and **Paper IV**, the used generator is LFS, which optimally forms the produced nanoparticles through

the vapor phase. **Paper I** uses multiple generators and thus multiple routes to form the nanoparticles, where the generation of sodium chloride (NaCl) particles with an atomizer is the only exception to the otherwise unifying formation route, as they are formed through a drying process from liquid droplets.

Test aerosols

Evaluating the performance of instruments requires tailored particles from controlled synthesis sources. Being able to produce particles not only with varying size but also with different morphologies and densities enables the generation of wide range of test aerosols. Figure 3.3 shows how the particle density depends on its structure and size.

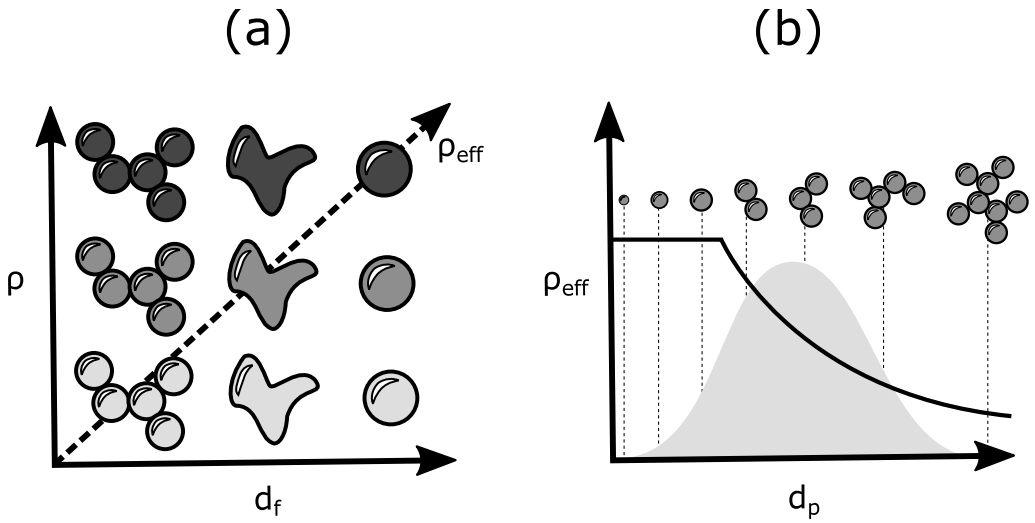

Figure 3.3: Illustration of particle density as a function of (a) fractal dimension and (b) particle diameter. This distinction is important in the sense that solid particles tend to form agglomerates and liquid particles stay mostly spherical. The effective density arrow in (a) shows the direction of greatest change and structural changes perpendicularly to it cause no change in the effective density. Over a number size distribution, the primary particles have bulk densities, while as the agglomerates grow their densities start to decrease.

For calibration purposes, liquid particles are generally produced as they form spheres naturally, so that there is less uncertainty about the structure and less deviation between the particle density and the bulk density, and the same generation setup can be used in a wide size range (Järvinen et al., 2018). Liquid particles also exhibit less bounce than solid particles, thus also reducing the chance of wrongly estimating collection efficiencies. This may happen because particles are not being collected, or they are miscounted due to the charge transfer processes, which, however, can be prevented with other means (van Gulijk et al., 2003). On the other hand, solid particles enable the measurement of instrument responses as a function of particle density or fractal dimension. Depending on the application, being able to measure agglomerates might also be more relevant.

Test aerosols can also be produced for dispersion (Mäkelä et al., 2009) and exposure (Sahu and Biswas, 2010) studies. In these cases, the source can be studied as is, or it can be tuned to produce desired particle morphologies and concentrations. Continuous and stable sources work best for the dispersion applications. In exposure studies, pulse-type

sources, where the production can be instantaneous or short in duration, work as well, given that the production yield is known. All of the different generation methods can be used for these purposes, but the study parameters may dictate what generators are suitable.

Most test aerosols were produced in **Paper I**, where a wide range of particle sizes and densities were required. Agglomerates and solid spherical particles of silver and titania were produced, along with NaCl and liquid dioctyl sebacate (DOS) particles. The DOS particles were also singly and multiply charged during the calibration of DENSMO. In **Paper II**, the generated alumina particle aerosol was used as the test aerosol as it contained both nanoparticles as well as residual particles.

Powders

Incorporating nanoparticles into functional products require large quantities of them. This entails the need to collect nanoparticles as powders. The most important quantity in this kind of synthesis is the amount of material producible, whether it is by mass or by surface area. Flame synthesis routes are widely used for generating nanoparticle powders, due to the scalability and high syntesis temperature. By selecting appropriate precursors and tuning the process parameters, powders ranging from catalyst nanoparticles (Strobel et al., 2006) to multicomponent decorated particles (Harra et al., 2015) can be produced. The produced powders can be collected by utilizing any of the deposition methods, though most commonly by filtration and electric fields.

Some low volatility precursors, however, cause problems in nanoparticle powder production by not evaporating fully after the spraying process. By reacting as a liquid precursor droplet, significant portion of the material mass is spent on these residual particles. (Strobel and Pratsinis, 2011) If, for example, a 2 µm particle was split up to 20 nm particles, you would get one million nanoparticles yielding 10000 times more surface area.

The optimization of powder production was achieved in **Paper II**, where the high production rate of LFS was tuned so that the mass lost in the residual particles could be turned into nanoparticles. Other produced nanoparticles in this thesis could also be collected as powders, with varying production rates, though the focus in those processes is not in powder generation.

3.2 Deposition of particles from gas phase to surfaces

The deposition mechanisms utilized in this thesis are well known and no new results are presented on the matter. However, for a better understanding of the underlying phenomena of the papers in this thesis and to elaborate on the connectedness of the presented results, the relevant portions of the theory are introduced below. In essence, this section creates a link between the airborne nanoparticles and their surface deposits.

Nanoparticles can spend extended periods of time suspended in the gas phase. Depending on the size of the particle, the time can range from seconds to months (Baskaran and Shaw, 2001), if no effort is being made to remove it from the gas phase. The magnitudes and types of forces present in any given situation depend on the size and material of the particles and on the surrounding conditions. A range of deposition mechanisms of particles to surfaces and fibers are depicted in Figure 3.4

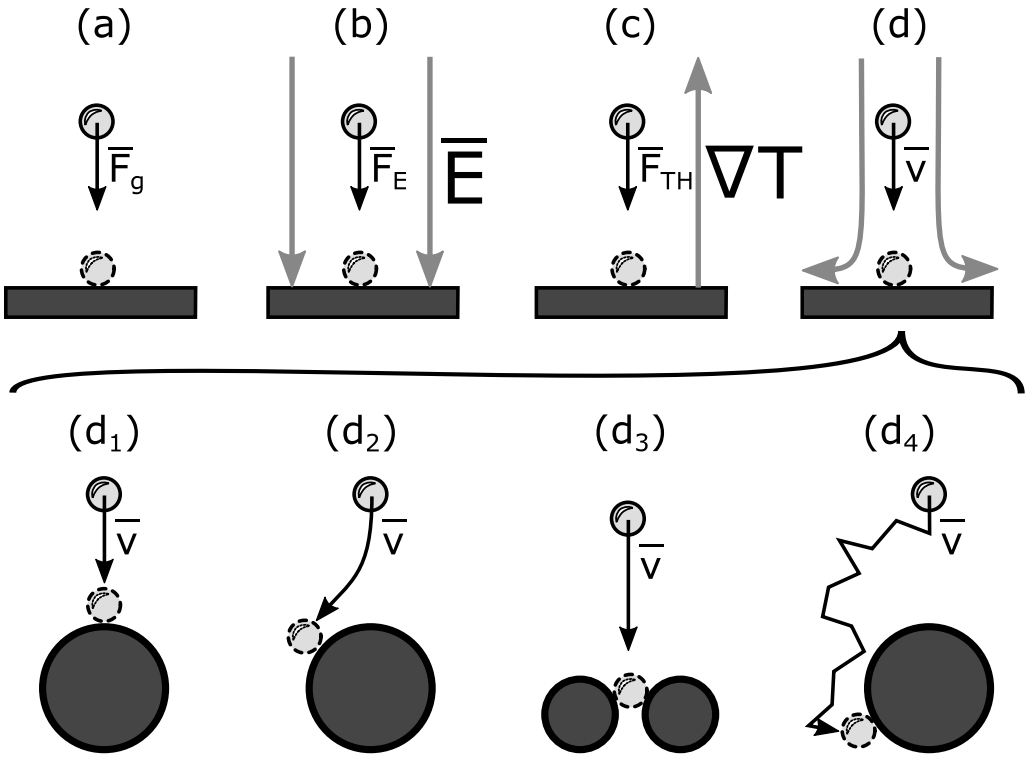

Figure 3.4: Deposition mechanisms for aerosol particles from gas phase to surfaces: (a) gravitational settling, (b) electrostatic precipitation, (c) thermoforesis and (d) impaction. The four main collection mechanisms of fibers: (d_1) impaction, (d_2) interception, (b_3) sieving and (d_4) diffusion. The diffusion has an effect during most of the other deposition mechanisms, and is typically taken into account in the loss term.

Gravity is a force that is always present, and its quantity F_g can be calculated with the familiar equation of

$$F_g = mg, \tag{3.2}$$

where m is the mass of the particle and g is the gravitational acceleration (Kulkarni et al., 2011). It can be clearly seen that this force diminishes quickly as the particle size shrinks, mass being a function of particle diameter d to the third power. Because of this, the gravitational force can typically be neglected for nanoparicles if there is other external forces being applied and there is no need to balance out forces for stable conditions. Particle levitation is one example where the force of gravity needs to be taken into account (Davis, 1997).

Another way to impart a force on a particle is to have it in an electric field of strength E. For the electric field to have an effect, the particle needs to be charged, either positively $+n$ or negatively $-n$. The particles can be charged with purpose-built chargers, utilizing either radioactive decay and producing a bipolar charge distribution (Wiedensohler and Fissan, 1991), or electric discharge giving a unipolar charge distribution (Hewitt, 1957). However, most naturally occurring particles are typically already charged (Jayaratne et al., 2016), as are synthesized particles originating from high temperature sources (Magnusson

et al., 1999). The electric force F_E can be calculated as follows

$$F_E = neE, \tag{3.3}$$

where e is the elementary charge. The magnitude of this force is dependent only on the charge state of the observed particle and the electric field strength, which means that there is no direct dependency on the particle size. However, the available charge states the particle can be in are dependent on the particle diameter. There are upper limits based on the size, material and charging method (Rayleigh, 1882), as well as probability distributions for the exact charge level.

In addition to having particles in potential fields, changes in temperature T can also apply a force on a particle, in this case called a thermophoretic force F_{Th}. The force is caused by the difference in the kinetic energy of the surrounding gas having dissimilar temperatures on the different sides of the particle. This difference in temperature can be expressed as the temperature gradient ∇T. The quantity of the force can be calculated with the following equations

$$F_{Th} = \frac{-p\lambda d^2 \nabla T}{T}, d < \lambda \tag{3.4}$$

$$F_{Th} = \frac{-9\pi d\eta^2 H \nabla T}{2\rho_g T}, d \geq \lambda \tag{3.5}$$

$$\tag{3.6}$$

where p is the gas pressure and λ is the mean free path. For particles bigger than the mean free path, the equation has more parameters characterizing the surrounding gas (gas viscosity η and gas density ρ_g) and a coefficient H. These are needed as the temperature gradient inside the particle starts to affect the surrounding gas temperature, so the coefficient takes into account the size and thermal conductivities. (Talbot et al., 1980; Waldmann and Schmitt, 1966)

In cases where there is relative velocity v between a particle and the gas surrounding it, there is drag force F_D trying to balance the velocities. The equation characterizing this is

$$F_D = \frac{C_D}{C_c}\frac{\pi}{8}\rho_g d^2 v^2, \tag{3.7}$$

where C_D is the drag coefficient, whose value is dependent on the flow regime. The flow around the particle can be laminar, turbulent or transitioning somewhere in between. How momentum can be transferred between the gas flow and the particle changes depending on the flow regime, thus also changing the imparted force.(Hinds, 1999) The interaction of particles and the surrounding gas in the nanometer range is also not straightforward. As the particle diameter gets closer to the mean free path of the surrounding gas, the collisions cannot be examined as continuum processes. To correct the granularity of the collisions and the particles "slipping" through the gas molecules, a Cunningham's slip correction factor C_c needs to be used to get the correct force (Allen and Raabe, 1985). The following equation gives the value of the correction factor

$$C_c = 1 + \frac{\lambda}{d}(2.34 + 1.05\exp(-0.39\frac{d}{\lambda})), \tag{3.8}$$

which has an effect of less than 5% for particles larger than 3 µm in typical conditions, but starts to increase rapidly for smaller particles.

The drag force tries to keep the suspended particles following the gas flow. However, there are several cases where it fails to do so. Impaction occurs when the gas flow takes a sudden turn due to an obstruction and there is not enough time for the drag force to change the moving direction of the particle to match. The excess momentum thus carries the particle over the flow lines of the gas and into the obstruction. The obstruction can be e.g. a flat surface or a fiber. Particles can still deposit even if the drag force manages to keep them following the gas flow. Especially larger particles can brush against obstructions and be intercepted due to the particle's path going partially through it. Tight channels and pores can also sieve particles if they physically cannot fit in them.

As particles move in gas phase, it is easy to imagine them moving straight as described by the previous forces. However, the thermal movement of the gas molecules around the particle is stochastic. The collisions between the particle and the gas molecules then makes the movement of individual particles actually quite random. This random movement of particles is called Brownian motion (Einstein, 1905). To characterize the magnitude of Brownian motion and the tendency of a collection of particles to spread out along the concentration gradient, diffusion coefficient D can be used

$$D = \frac{kTC_c}{3\pi\eta d}, \tag{3.9}$$

where k is the Boltzmann's constant (Hinds, 1999). Based on this, it can be said that the diffusion in the gas phase is greater for smaller particles, and so is the diffusion deposition to surfaces.

Some of the deposition mechanisms are practically always prevalent, namely diffusion and gravitational settling. However, the magnitude of these is so dependent on size that mainly the diffusion has an effect on the results of this thesis, as diffusion typically contributes to the loss of particles. Thermophoresis is used for a similar coating process in **Paper III**, where the high temperature gradient between LFS and the room temperature substrate is exploited.

3.3 Surface functionalization with nanoparticles

The interactions between bulk materials and the surrounding gas phase happen on surfaces. By coating surfaces, more functionality can be introduced to materials and structures. The coating can make the surface e.g. anti-bacterial or change its wetting behavior. Examples of these kind of coatings are shown in Figure 3.5, where the first shows a slippery liquid infused porous surface structure (SLIPS, Kim et al. (2012)) made with nanoparticles and the second nanoparticle decorations on fibers.

Wetting and icing of surfaces

There are two geometric aspects to the wetting of a surface: the contact angle between the surface and the wetting liquid, whether it is the apparent or actual angle (Teisala et al., 2018), and the penetration of the liquid into a porous structure. The wetting angle of over 90 degrees denotes low surface free energy and a phobic surface. Comparably, a wetting angle of less than 90 degrees denotes high surface free energy and a philic surface. The wetting behavior can be measured by using goniometry (Young, 1805), where dynamics of introducing and removing water droplets from the surface, as well as the sliding of water droplets on an inclined surface, reveal the interacting forces between the studied phases.

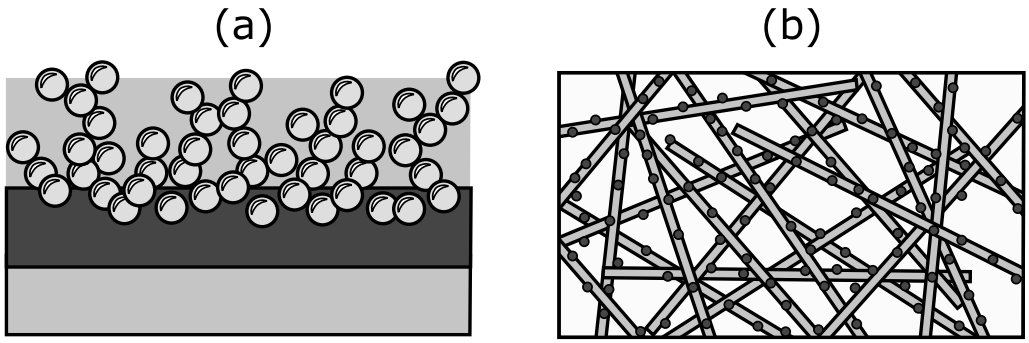

Figure 3.5: Cross-sections from (a) SLIPS functionalized and (b) anti-bacterial surfaces, illustrating surface coatings made in this work. The anti-bacterial coating consists of silver nanoparticles on fibers and the SLIPS structure consists of a porous titania nanoparticle layer on top of LDPE that has been infused with silicon oil.

Depending on the surface free energy and how the liquid is introduced on the porous surface, the liquid can permeate in the pores and cavities in the surface and be locked in place. Wenzel and Cassie-Baxter states are used to describe the penetration of liquid into a porous structure. In the SLIPS structure, the pores are filled with a lubricant, which can change the surface free energy, and thus the wetting behavior, as well as keep other liquids from entering the pores. A SLIPS structure was prepared in **Paper III**, where LFS-generated titania nanocoating was used as the porous layer. Schematics of the different wetting states are shown in Figure 3.6.

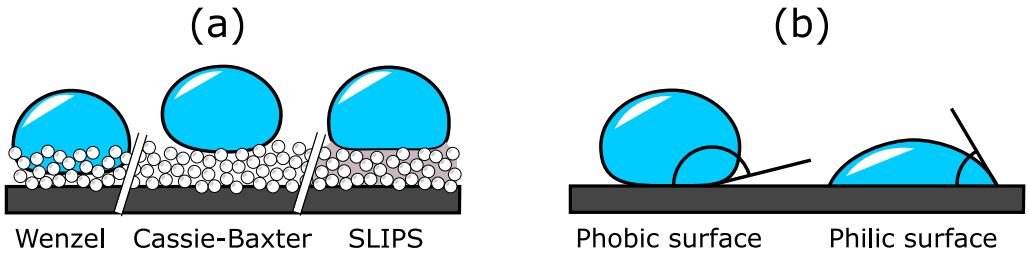

Figure 3.6: Wetting behavior relevant to the SLIPS structure: (a) Three wetting states of a porous surface and (b) contact angle of over 90° for phobic surface and under 90° for philic surface.

In colder environments, in addition to being wetted, surfaces can experience icing. In some applications it is necessary to be able to remove ice that has been accreted on a given surface, or prevent it from happening from the get-go. Preventing water from staying on the surface long enough to freeze is one option; another is to design the surface so that the ice has minimal attachment force and can thus be removed with ease if desired. This force between a surface and the ice covering it can be measured with a centrifugal adhesion test (CAT, (Koivuluoto et al., 2015)), where the sample is rotated on the end of a beam with increasing velocity until the ice is removed from the surface.

Anti-bacterial surfaces

Contamination of surfaces with bacteria is a growing problem, especially in hospital environments where antibiotic resistant bacteria threaten lives (Tenover, 2006). Nanoparticles have been found to still have an effect on these kinds of bacteria, giving a possible way to fight them. However, they should be studied thoroughly before any widespread implementation into commercial products, as to not generate nanoparticle resistant strains of bacteria. Anti-bacterial activity can be introduced to a surface by the addition of nanoparticles made out of e.g. silver (Sotiriou and Pratsinis, 2010), copper oxide (Jadhav et al., 2011) or zinc oxide (Sirelkhatim et al., 2015), of which silver nanoparticles were utilized in the functionalization of fiber filters in **Paper III**. Figure 3.7 shows how silver nanoparticles interact with bacteria.

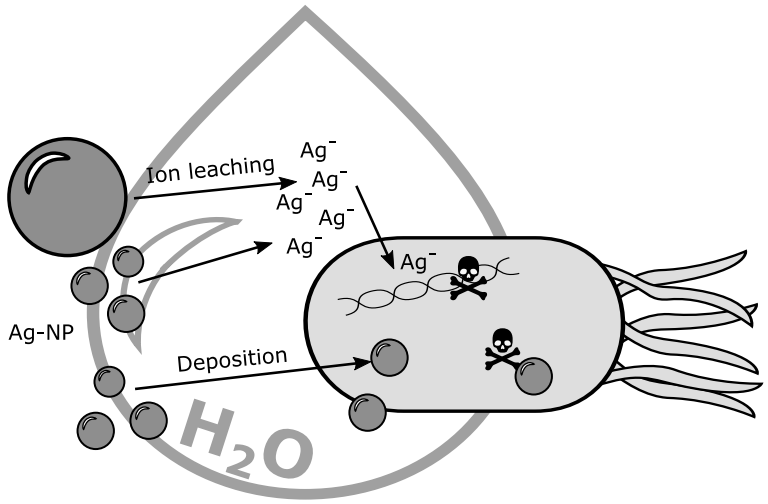

Figure 3.7: Anti-bacterial activity of silver nanoparticles. In humid conditions silver ions and small nanoparticles are free to diffuse and interact with bacteria. The ions and nanoparticles then interfere with the vital functions of the bacteria.

The anti-bacterial activity of silver nanoparticles can mostly be attributed to the leaching of silver ions, but small nanoparticles can also attach on the surface of bacteria, which both can block DNA replication and disrupt the cell membrane's ability to transport vital molecules (Morones et al., 2005). Both of these mechanisms benefit from the presence of water. Another mechanism nanoparticles can utilize in the destruction of bacteria is photo catalysis, applicable for example with zinc oxide and titania (Nikkanen et al., 2013). The photo catalysis produces reactive oxygen species (ROS) by exciting electrons in materials with appropriate band gaps (Maness et al., 1999). Depending on the application, band gaps corresponding to visible light or UV-light wavelengths can be used.

4 Results and discussion

The results of this thesis are organized in three parts, following the main points of the aim given in the introduction. First, the structure and calibration of DENSMO is discussed in the point of view of instrument development. The use of DENSMO as a synthesis monitor gives information on the tuning of the produced aerosol, which is discussed second. The control of the synthesis process contains, in addition to the effective density measurements, the removal of residual particles and the mass measurement results. Lastly, results pertaining to the functional coatings are discussed, which include SLIPS and anti-bacterial coatings. An overview of the used methods and materials is listed in the Table 4.1 with a synthesis characterization focus. For more detail on the measurement setups, consult the included papers.

Table 4.1: A compendium of the whole synthesis process for each of the included papers, containing a list of the instruments and methods used for the characterization and the production of nanoparticles and their applications.

	Paper I	**Paper II**	**Paper III**	**Paper IV**
Generators	Atomizer Furnace Bubbler SCAR	LFS	LFS	LFS
Materials	Ag DOS NaCl TiO_2	Ag Al_2O_3	TiO_2	Ag
Utilized deposition	Electric field Filtration Impaction	Electric field Impaction	Thermoforesis	Electric field Filtration Impaction
Instrumentation	DENSMO ELPI SMPS	DLPI ELPI SMPS TEM SEM	CAT Goniometer SEM	DENSMO ELPI SMPS TEOM QCM-MOUDI
Measured quantity	Effectice density Number Size Charge	Effective density Mass Number Size	Contact angle Sliding angle Ice adhesion	Effective density Mass Number Size
Application (for particles)	Test aerosol	Nano powder	SLIPS	Anti-microbial coating

4.1 Density monitor

The structure of the instrument developed in **Paper I**, DENSMO, is depicted in Figure 4.1. The function of DENSMO is to measure the effective density with electrical means, and the structure mirrors this. Going with the aerosol flow through the instrument, there are four main parts to the operation: charging, mobility sizing, aerodynamic sizing and filter collection. Thus, the particles are charged to a known charge state, after which the last three sections collect particles and three currents are measured. Ratios of these currents correspond to the collection efficiencies of the mobility sizer and the aerodynamic sizer, which give information on the median sizes and ultimately on the effective density of the particles. Similar approaches can be found in commercial aerosol sensors such as DiscMini (Matter Aerosol) and Partector (Naneos), which focus on the measurement of particle surface area, but DENSMO and its predecessor (modification to ELPI, Rostedt et al. (2009)) are the only instruments which encompass both the mobility sizing and the aerodynamic sizing in one instrument.

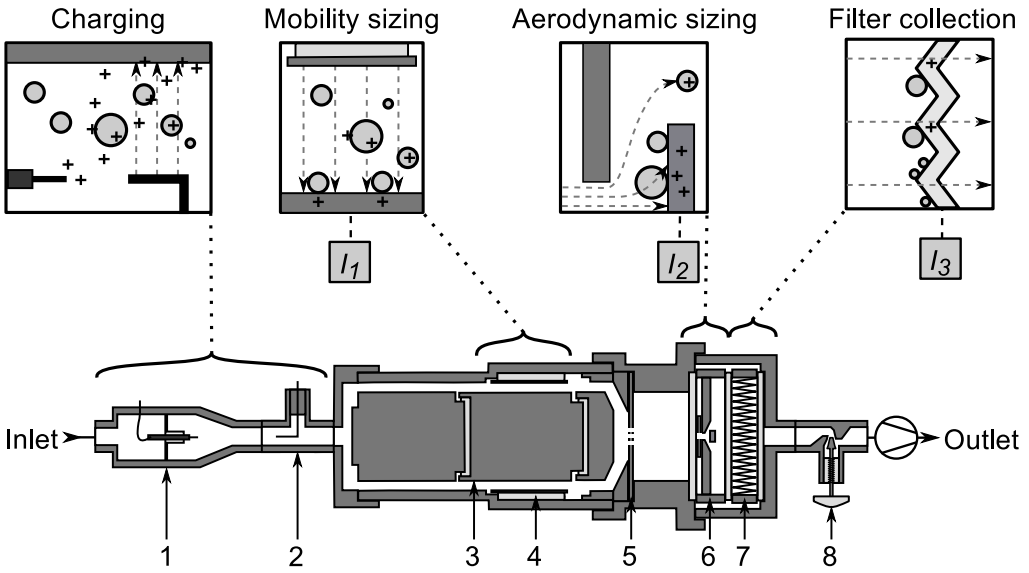

Figure 4.1: Cross-section of the structure of DENSMO. The numbered labels indicate: 1. corona charger, 2. ion trap, 3. mobility analyzer collection cylinder, 4. mobility analyzer voltage cylinder, 5. critical orifice plate, 6. low pressure impactor, 7. filter and 8. needle valve. The illustrations on top of the figure show the function of the main parts, with the measured currents denoted with I_1 to I_3. (**Paper I**)

Before a developed instrument can be used for its intended purpose, it needs to be calibrated. The calibration results of the mobility analyzer and the low pressure impactor are shown in Figure 4.2, where each measurement point corresponds to a singly-charged monodisperse aerosol with that given size.

The collection efficiency of the mobility analyzer $\eta(d_b)$ is proportional to the electrical mobility, but the charge state must be known before the connection to the mobility diameter can be made. This is why it is convenient to have particles that are singly charged. Another benefit comes from the straight relation between the particle number concentration and the measured current, which becomes more apparent in the calibration

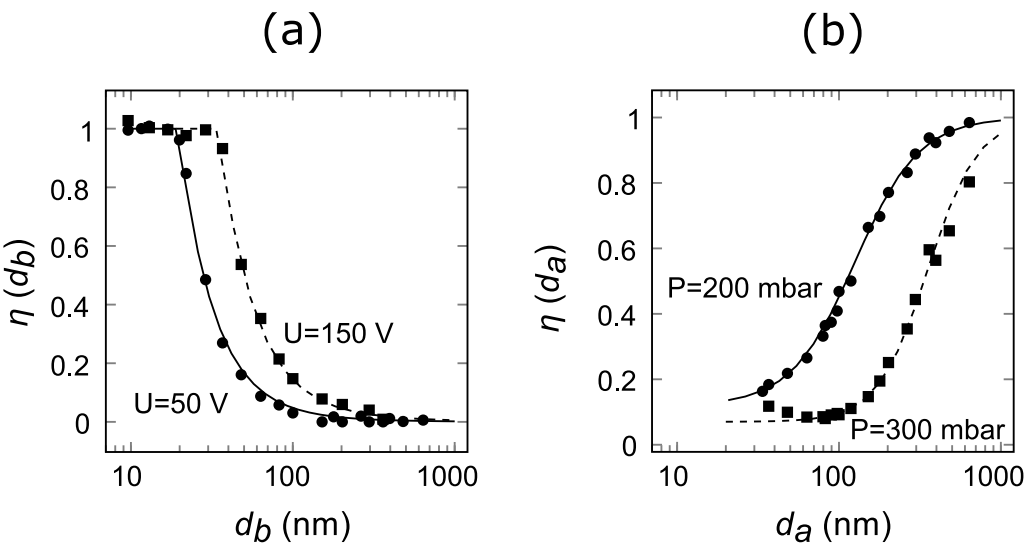

Figure 4.2: The calibration results of (a) the mobility analyzer and (b) the low pressure impactor of DENSMO, for singly charged particles. The collection efficiencies of the mobility analyzer and the low pressure impactor are controlled by altering the used voltage and pressure, respectively. (**Paper I**)

of the corona charger. The collection efficiency of the low pressure impactor $\eta(d_a)$ is dependent on the aerodynamic diameter, thus the effective density of the size selected particles needs to be known. By using liquid particles here, the shape of the particles is spherical due to surface tension, and moreover, the effective density is the bulk density of the used material. So in essence, the calibration of both the mobility analyzer and the low pressure impactor can be done in series if e.g. singly charged DOS particles are used, which was the case with the calibration of DENSMO. As can be seen from Equations 2.2 and 2.3, which characterize the operation of the mobility analyzer and the low pressure impactor, DENSMO can be optimized to measure certain size and effective density ranges by changing the used collection voltage and the pressure of the impactor. The difference in the collection efficiency can be seen in Figure 4.2. This enables the use of the steepest section of the collection efficiency curves, where the instrument is most sensitive and the available measurement range is also more broad for mobility and aerodynamic diameters as well as, consequently, the effective density.

The calibration results of the corona charger are shown in Figure 4.3. The effective charge (here denoted as average charge n_{ave}, for further discussion on the exact difference see e.g. Rostedt et al. (2017)) and the Pn product have been calibrated with the aforementioned DOS particles. The corona charger produces a charge distribution, which means that particles with the same physical size can have different mobility diameters, thus producing a different response on the mobility analyzer. The effective charge links the charge distribution, produced with the corona charger, to the collection efficiency of the mobility analyzer. As the mobility analyzer only measures charged particles, the effective charge must be over one for all particle sizes. The losses and charging efficiency of the corona charger, which can be used to convert the measured current back to the measured number concentration, are merged into one factor: the Pn product (e.g. Marjamäki et al., 2000).

The utilization of DENSMO as a synthesis monitor and the results are discussed in the

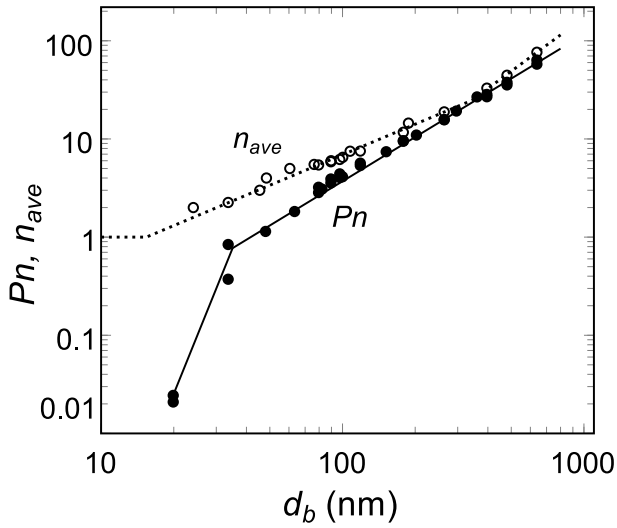

Figure 4.3: The calibration results of the corona charger used in DENSMO. The effective charge and the Pn product values are shown. Note that the average charge cannot be under 1, due to the measurement only taking charged particles into account. (**Paper I**)

next section. These calibration results, however, give foundation to the operation of the instrument and limit its operation range. The lower limit is mainly set by the charger efficiency to 20 – 30 nm, depending on the number concentration. The sharp corner in the collection efficiency of the mobility analyzer affects the measurement, depending on the geometric standard deviation of the measured particle distribution. The upper limit is set by the collection efficiency of the low pressure impactor for high density particles and by the mobility analyzer for lower densities. The electrical mobility starts to rise again after about 300 nm, which increases the collection efficiency of the mobility analyzer and the unique solution is lost. For optimal response, the collection efficiencies should be around 0.5, where the smallest change in particle diameters causes the largest change in the measured collection efficiency.

4.2 Density and mass of particles

Effective density of individual particles

A wide range of nanoparticles with different sizes and densities were produced in this thesis and an overview of them can be seen in Figure 4.4. The most diverse selection of generation methods was used in **Paper I**, where DOS particles were produced with an evaporation-condensation generator, NaCl by atomizing and then drying aqueous salt solution, titania by thermally decomposing bubbled TTIP vapor and silver with a typical tubular furnace setup. The generator used in the nanoparticle production in **Paper II**, **Paper III** and **Paper IV** was the LFS, producing alumina (Al_2O_3), titania and silver particles, respectively.

The structure of the generated solid particles can be altered from the state that they come out in straight from the generator. Here, the morphology was controlled by using either a residence time chamber or a sintering furnace to change the effective density through agglomeration and sintering, respectively. In **Paper I**, the large agglomerates

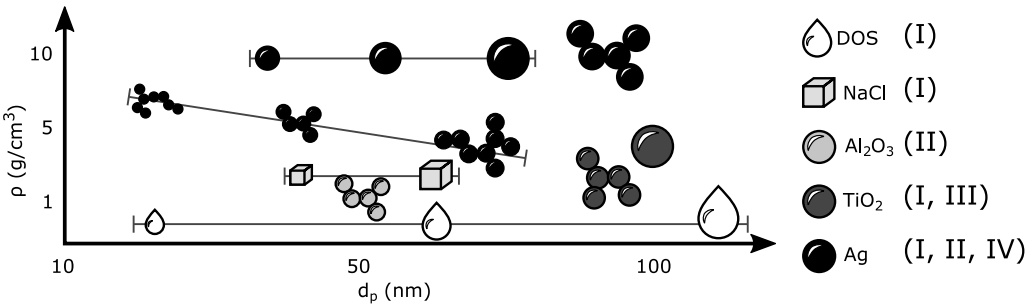

Figure 4.4: Produced particle morphologies. The relevant paper is listed in the legend. Lines connecting different points in the figure show the range of particles produced in any given instance, for example the DOS particles were generated for the calibration of DENSMO with the whole particle diameter range.

and the large spherical particles were produced by first letting the aerosol agglomerate, growing the diameter of the particles. The large agglomerates could then be sintered to more spherical morphology. In **Paper IV**, the LFS generated nanoparticles are guided through a residence tube, in which the gas temperature stays higher longer, sintering the silver particles spherical. This does not happen without the residence tube, as is reported in several previous studies (**Paper II**,Aromaa et al. (2012); Rostedt et al. (2009)).

DENSMO was used in **Paper I** and **Paper IV** in conjunction with the combined use of SMPS and ELPI. A comparison of the effective density measurement results given by these methods are shown in Figure 4.5. The measured effective densities fall mostly inside the estimated uncertainty of ±20%, but a few measurements with greater deviation show the effect of particle bounce, which is caused by problematic particle morphologies and, possibly, the impactor loading due to high concentration.

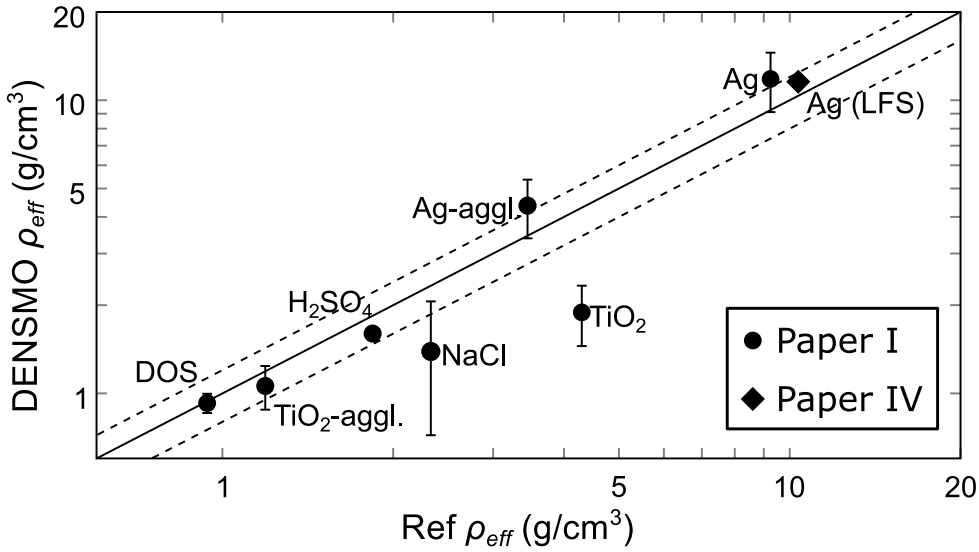

Figure 4.5: Effective density measurements made with DENSMO. The results are from **Paper I** and **Paper IV**. The SMPS-ELPI method was used as the reference. Dashed lines denote ±20% uncertainty. (Adapted from **Paper I**)

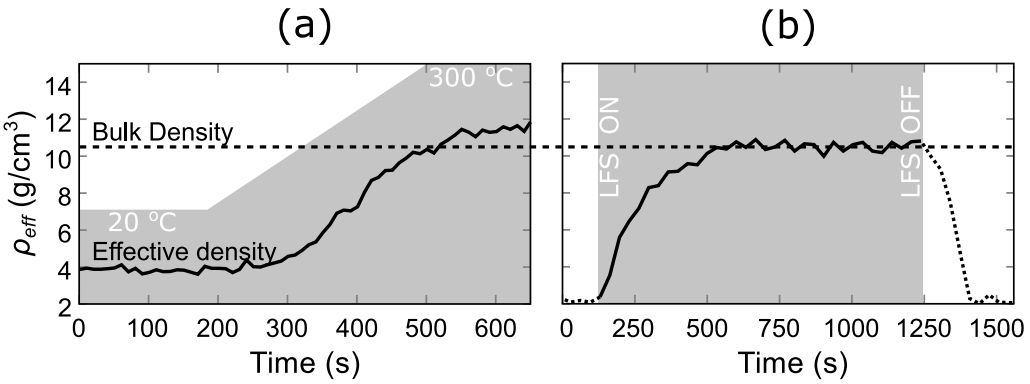

Figure 4.6: Real-time measurements from transient processes: (a) the sintering of silver nanoparticles and (b) generating silver nanoparticles with LFS. The sintering took place during a continuous heating from 20°C to 300°C illustrated with the dark background, which in the LFS generation shows the start and end of the synthesis process. (Adapted from **Paper I**)

All in all, DENSMO is a capable measurement instrument when the effective density is the relevant value. As a monitor, the effective density measured by DENSMO can be used alone to see important stages of the synthesis process. Figure 4.6 shows the results of (a) the sintering of silver agglomerates in **Paper I** and (b) one synthesis cycle of silver nanoparticles in **Paper IV**. In the case of LFS synthesis, a clear transient period can be seen after the ignition of the LFS, showing as a steady increase in the effective density in Figure 4.6 (b), which is caused by stabilizing temperature.

Mass size distribution of nanoparticles

The reduction of residual particles is achieved in **Paper II** by the addition of ethylhexanoic acid (EHA), which aids the evaporation of the precursor liquid. TEM images of the produced powder are shown in Figure 4.7. The effect the addition of EHA has on the distribution of mass to the residual mode and on the nanoparticle mode is clearly visible. Without the addition of EHA, several micron-wide residual particles can be seen to contain most of the alumina that was collected. Previously, the residual removal has been achieved by adding excessive amount of EHA to the precursor solution (e.g. Mädler et al., 2006; Rosebrock et al., 2013), however as little as 5% was shown to be enough. As the EHA is added the coverage of the nanoparticles can be seen to increase dramatically on the TEM images.

The transfer of mass from the residual mode to the nanoparticle mode increases the number concentration of the nanoparticles only to a certain point, until the coagulation of the nanoparticles starts to increase the particle diameter with the cost of number concentration. This can be seen in the aerosol measurement results in Figure 4.8, where number size distributions from SMPS and ELPI are shown.

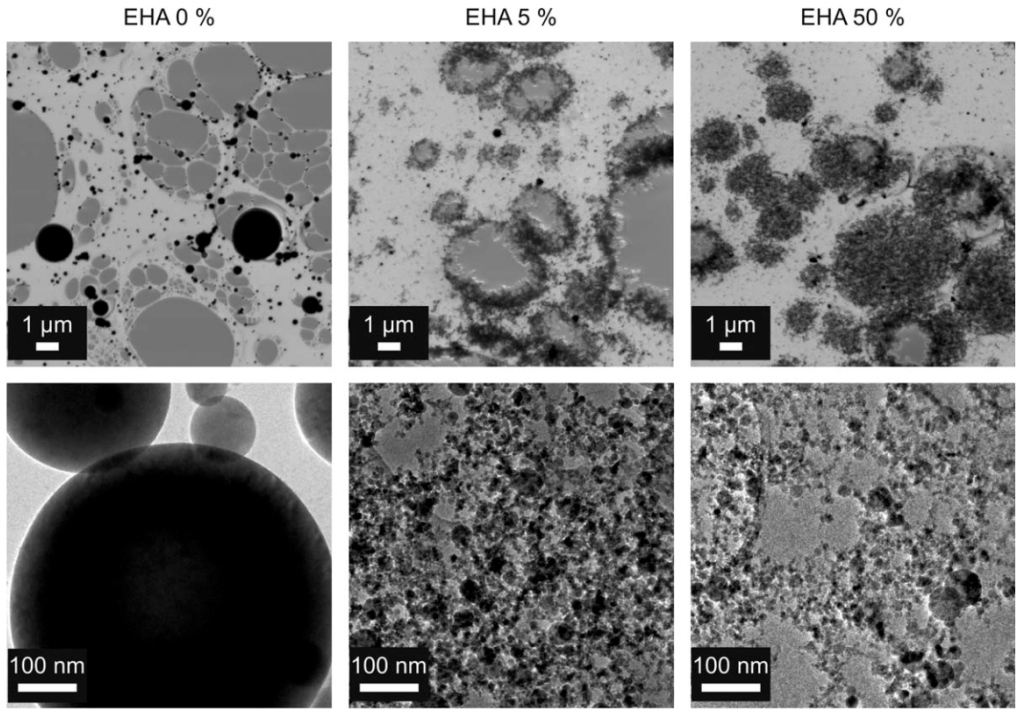

Figure 4.7: Powder optimization by addition of EHA to remove residual particles from the produced alumina nanoparticle powder. The absence of the residual particles is evident after the addition of 5% of EHA, and higher amounts do not change the nanoparticle size any further. The difference in the amount of nanoparticles can be explained by the image position on the grid and the collection time of the sample. (**Paper II**)

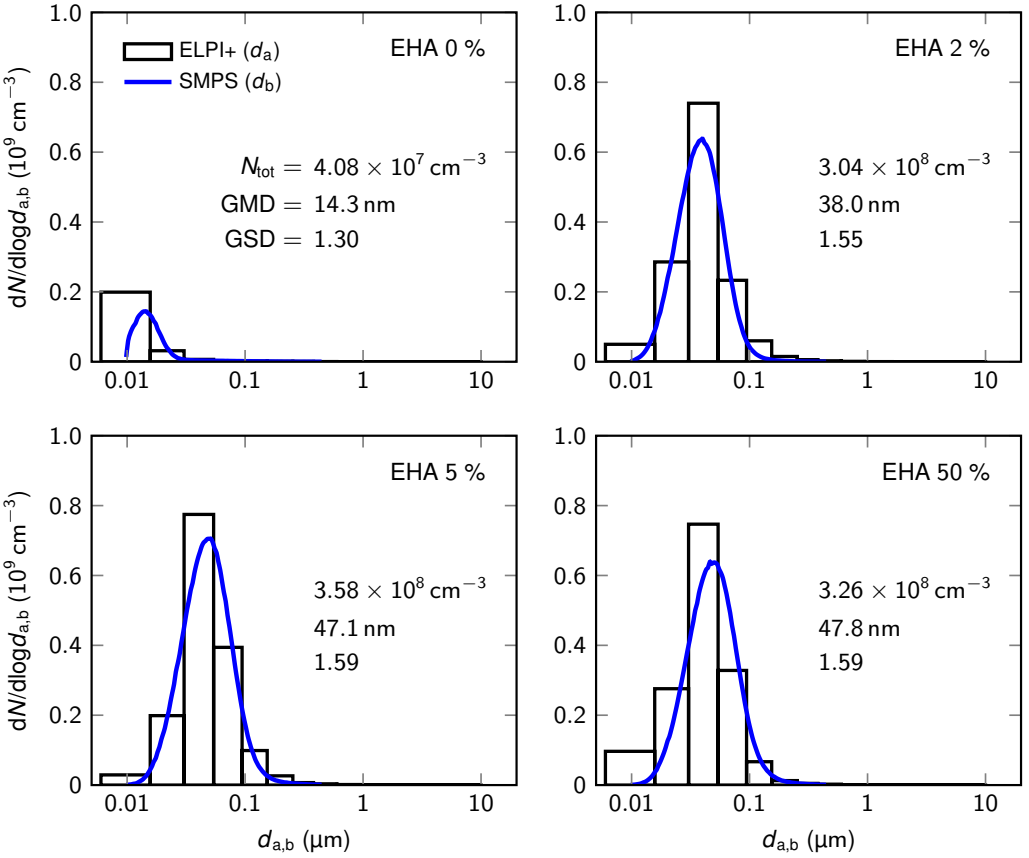

Figure 4.8: The change in the number-size distribution of alumina particles as a function of added EHA. The ELPI+ and SMPS distributions overlapping here indicate an effective density of close to one. Additionally, the number concentration and the mean particle diameter do not change noticeably after the addition of 5% of EHA. (**Paper II**)

Here, the number concentration of the alumina nanoparticles is limited to about 3×10^8 cm^{-3}, whereas the geometric mean diameter of the produced agglomerates keeps increasing to 47.1 nm. Other aspect that can be deduced from the aerosol measurements is that the SMPS and ELPI measurements overlap, even though the bulk density of alumina is 3.99 g/cm^3, indicating that the produced nanoparticles are highly agglomerated. SMPS-ELPI fitting procedure yields an effective density value of 0.7–0.9 g/cm^3, which was used in calculating the mass of the nanoparticle mode as a function of the EHA vol-%. These results are shown in Figure 4.9 with the DLPI measured masses of the nanoparticle mode and the residual mode. The trade of mass from the residual mode to the nanoparticle

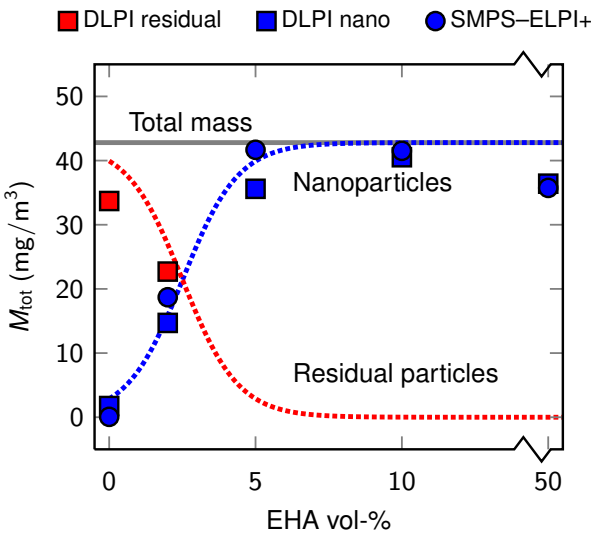

Figure 4.9: Powder optimization by addition of EHA to remove residual particles. The transfer of mass from the residual particles to the nanoparticles increases quite linearly as a function of the added EHA, until almost all of the mass generated is in the nanoparticle mode, at around 5% of EHA. (**Paper II**)

mode as a function of the added EHA is again evident. In addition, the limit where residual particles are removed with this synthesis process can be determined. Interestingly, there is no need to actually measure the residual particles in order to determine this limit; instrumentation measuring only the nanoparticles from the aerosol is enough to see the appearance or the absence of residual particles.

4.3 Slippery and anti-bacterial surfaces

SLIPS

In **Paper III**, a gas phase synthesis method, LFS, was used for the first time to produce a hierarchical SLIPS structure on a thin LDPE coated paper material. The aim was to make an anti-icing surface without the use of perfluorinated lubricants, which have been found to be harmful for the environment (Suja et al., 2009), with a highly scalable process (Haapanen et al., 2018). The wide adoption of these kinds of surfaces have been bottle-necked by the cost of manufacturing.

The porous titania nanoparticle coating produced here consists of agglomerates with a primary particle size of 20 – 30 nm. SEM image of this structure is shown in Figure 4.10. As the substrate is passed through the flame, the formation of the nanoparticles is not complete before they are deposited to the surface. Here, the main driving force for the depostion is thermophoretic force, due to room temperature substrate being quickly introduced into a several thousand kelvin flame. For multiple coating cycles, the already deposited porous coating undergoes sintering to some degree, which depends on the particle material and the coating distance. The substrate being coated also experiences heating, which needs to be controlled, unless the substrate is meant to be burned. The rapid and short coating process allows the minimization of heat flux to the substrate, which enables the coating of thermally fragile substrates such as plastic (**Paper III**) and paperboard (Stepien et al., 2013).

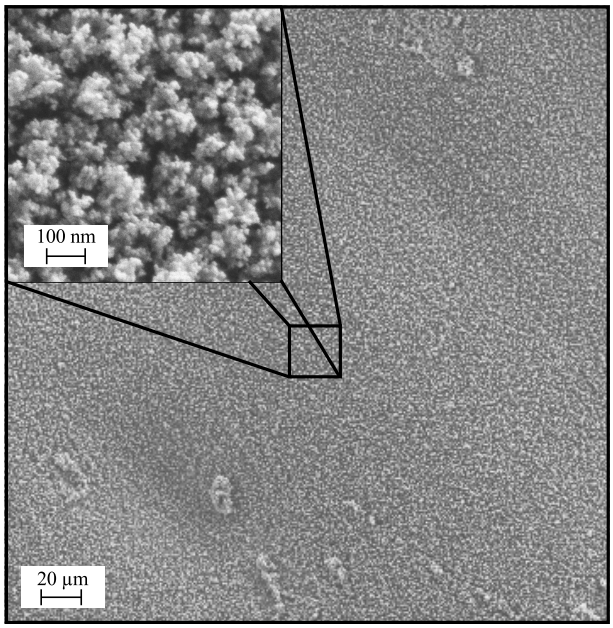

Figure 4.10: SEM image from the SLIPS surface structure. The primary particle size can be seen to be around 20 – 30 nm. The coverage of the nanoparticle layer is rather uniform over the deposition area. (**Paper III**)

To complete the SLIPS structure, the porous titania coating is impregnated with a lubricant, in this case silicon oil. The coating was tested for ice adhesion with four consecutive icing cycles, each containing an ice accumulation phase and then the centrifugal force measurement. The results from these measurements are shown in Figure 4.11. In these measurements, three reference materials were used: plain LFS generated titania coating, silicon oil lubricated LDPE substrate without the nanoparticle layer, and PTFE-tape (3M).

These results show two significant effects from the icing behavior of the nanoparticle coating: the manifestation of the wenzel state and the power of the SLIPS structure. The wenzel wetting state, where water on the surface penetrates the porous surface coating, allows the forming ice to mechanically attach itself on the surface, which significantly increases the ice adhesion force. In the SLIPS, the structure filling oil keeps this from

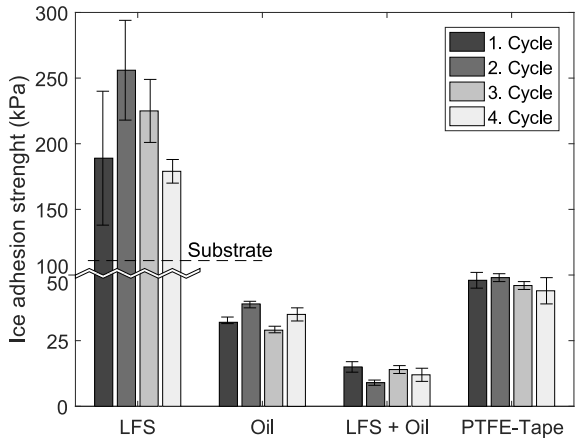

Figure 4.11: Ice adhesion strength for different tested surfaces for four consecutive ice accretion cycles. The mechanical attachment of the ice to the porours nanoparticle layer results in high adhesion strength values. The produced SLIPS structure, however, shows a significantly reduced adhesion strength. (**Paper III**)

happening. Conversely, the porous titania coating helps keep the oil from escaping underneath the forming ice, which can be seen in the difference of ice adhesion strengths between the oiled LDPE and the SLIPS.

The LFS-made SLIPS had quite consistent performance over the four test cycles, and exhibited the lowest ice adhesion strength value of 9 kPa. Similar and lower values have been reported e.g. by Niemelä-Anttonen et al. (2018) with surfaces made with perfluorinated oil and PTFE membranes yielding lowest value of 8 kPa and by Beemer et al. (2016) with PDMS gels yielding an ice adhesion strength of 5 kPa. However, former utilizing perfluorinated materials and latter having problems with scaling up the process.

The behavior of water on top of this coating was studied in the form of water contact angle and water sliding angle. The results of these tests are shown in Figure 4.12, which were measured before and after each of the ice adhesion tests.

These results confirm the mechanical interlocking that happens in the plain LFS titania coating, as the test water droplet does not slide from the surface even when tilted vertical. Additionally, the highest peaks from the porous structure are removed after every icing cycle, which reduces the roughness of the surface, lowering the contact angle between the coating and the water droplet. The oiled surfaces and their wetting behavior is mainly dominated by the chemistry between the used silicon oil and the water droplet. What deviates from this is the initial value for the SLIPS coating. Here, it is likely that the titania structures have protrusions over the oil layer reducing the contact area, which are removed after the first icing cycle.

Anti-microbial coating

The anti-bacterial coating made in **Paper IV** on a fiber filter was achieved by letting the fibers filter out the nanoparticles from the aerosol passing through it. A fiber filter consisting of both microfibers and nanofibers was coated and SEM images from a filter of

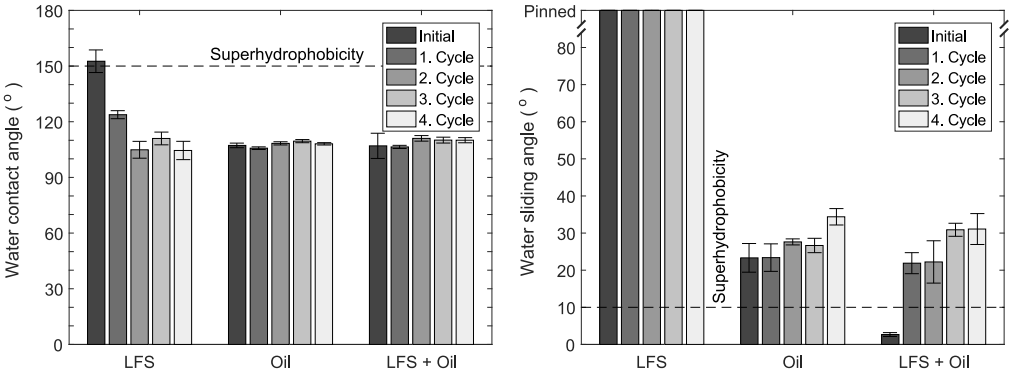

Figure 4.12: Water contact angles (left) and sliding angles (right) for different tested surfaces and after each ice adhesion test. The pinning of water droplets to the pure nanocoating and the wear of the highest peaks in the SLIPS structure show clearly in the water sliding angle measurements. (**Paper III**)

(a) only microfibers, (b) mix of both fibers and (c) coated mixed fiber filter are shown in Figure 4.13.

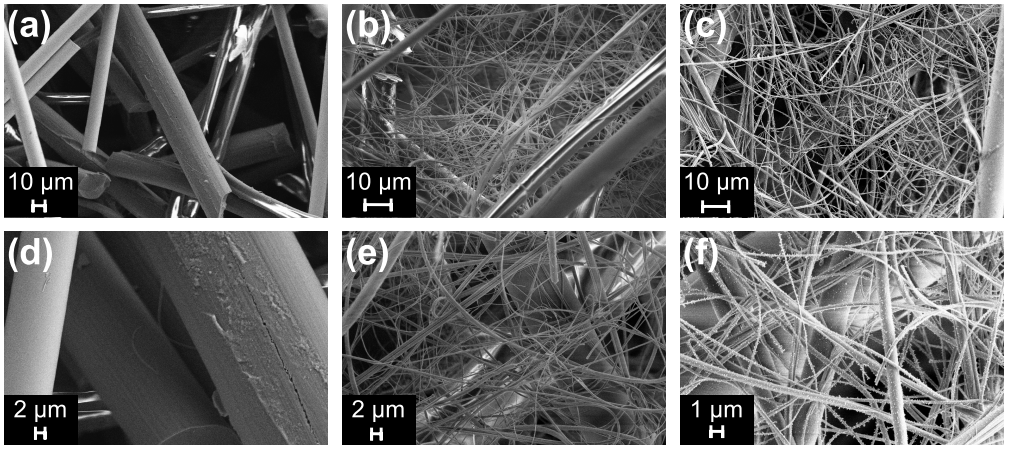

Figure 4.13: SEM images from produced (a,d) microfiber (b,e) mixed fiber and (c,f) coated mixed fiber filters, with higher and lower magnification. The nanoparticles can be seen to uniformly cover the fibers, and there is a clear contrast difference between the different microfiber materials. (**Paper IV**)

The microfibers used in the filter media were made from glass, polyvinyl alcohol (PVA) and activated carbon fiber (ACF), which form the base, bind all the fibers together and introduce adsorption capability, respectively. This maretial was used as the reference and is denoted as F0. In addition to these materials, nanoscale glass fibers were added to reduce the distance between the fibers and add surface area to the filter, forming sample F1. Both of these increase the collection efficiency of the filter for the smallest and largest particles. Third fiber filter sample F2, also included silver nanofibers. The penetration of the prepared filter media was tested from 30 nm to 7 µm, and a theoretical collection

efficiency was calculated based on the filter properties following the study by Choi et al. (2017). The filter penetration results are shown in Figure 4.14.

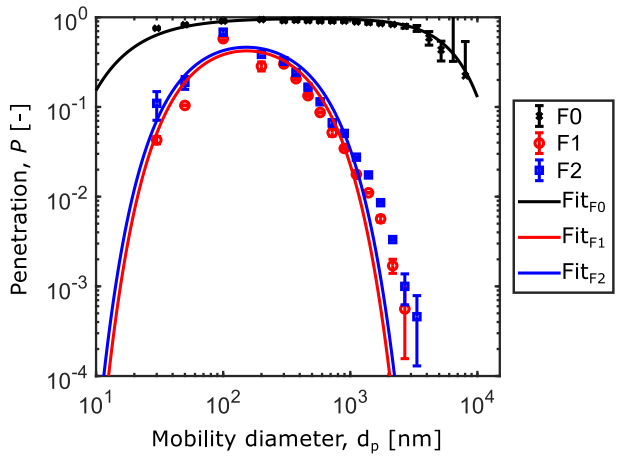

Figure 4.14: The collection efficiency of the produced filter media: F0, F1 and F2 denote mirofiber, mixed fiber and mixed fiber with added silver nanofibers, respectively. Adding the nanofibers increases the collection efficiency significantly for the nanoparticles, this is due to increased collection with diffusion. (**Paper IV**)

The penetration measurements clearly show the increase in the collection efficiency, as well as the difficulty of collecting particles near 100 nm, which do not easily collect due to either diffusion or impaction. However, the produced silver particles with a diameter of 43 nm saw a clear benefit from the addition of the nanofibers, as the collection efficiency increased from 20% to 85%. If desired, the collection efficiency can be increased further by using a thicker or multilayered filter of the material developed in this thesis, or changing the material further to optimize for collection efficiency. The silver nanoparticles were prepared by LFS to have a good mass production rate for the coating, as 1 m-% of silver loading was aimed for, creating sample F3. The LFS-generated silver nanoparticles were guided into a residence tube (Sorvali et al., 2018), where the maintained high temperature sintered the nanoparticles nearly spherical, which can be seen from the aerosol measurements done during the coating process. Aerodynamic and mobility number size distributions were measured with an ELPI+ and an SMPS, respectively, with DENSMO monitoring both in real-time on the side. The mass distribution was measured with a QCM-MOUDI and the total mass concentration with a TEOM. All of these results measured during the coating process, from a stable section of the synthesis process, are shown in Figure 4.15.

Based on these measurements, effective densities of 10.4 and 11.2 g/cm^3 were calculated for SMPS-ELPI+ combination and for DENSMO, respectively. These values indicate that the residence tube indeed sintered the produced silver nanoparticles to a significant degree. The effective density values could be further used in the calculation of the mass distribution, by changing the number size distribution measured with SMPS to a mass size distribution. The calculated mass size distribution compares well with the one measured with the QCM-MOUDI, and integrating over them gives total mass concentration values of 16.1 and 14.5 mg/m^3 respectively, which are also in agreement with the value of 15.6 mg/m^3 measured with TEOM.

The aerosol measurements also made possible the determinations of the required coating

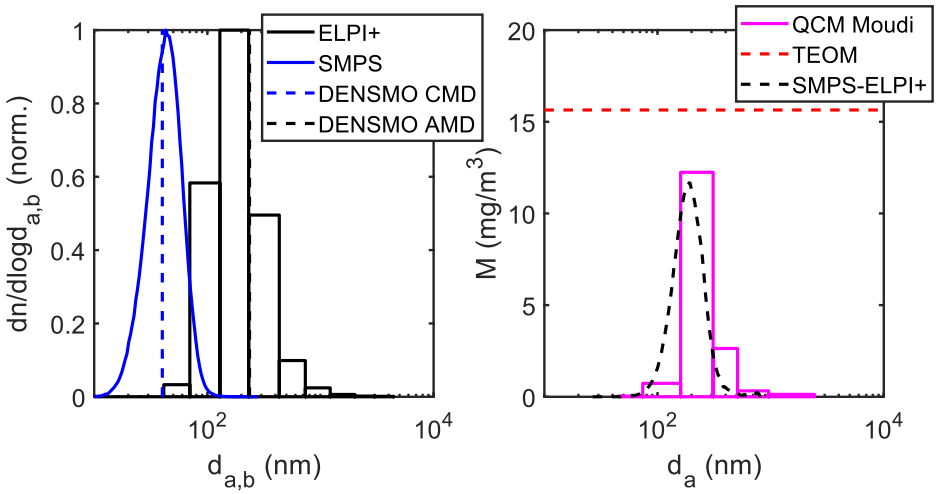

Figure 4.15: Number-size distributions and mass distributions of the silver aerosol. The mean particle diameters measured with DENSMO are in good agreement with the spectroscopic results. The large difference between the mobility and aerodynamic distributions indicate a high density for the measured nanoparticles. The mass distribution shapes are also in good agreement, of which the SMPS-ELPI+ one has been normalized. (**Paper IV**)

time to achieve 1 m-% mass loading of silver nanoparticles on the filter media. Knowing the number size distribution of the silver and the collection efficiency of the prepared filter media, two 12.5 min coatings were required, one per side, to achieve this loading. This mass loading was chosen for the coating because it was to be tested against a similar fiber filter media, but with 1 m-% of silver nanofibers embedded in the filter instead of nanoparticles.

To test whether or not the silver added to the filter media has the desired anti-bacterial effect or not, a touch test (Gunell et al., 2017) was performed against *Staphylococcus aureus (S. aureus)* and *Escherichia coli (E. coli)*, which are a gram positive bacteria problematic in medical environments, especially its antibiotic resistant strain, and a gram negative bacteria found typically in lower intestines. An example agar growth plate and the mean bacterial growths of all the tests are shown in Figure 4.16.

The tests were done for both of the silver containing filter media (F2 with silver fibers and F3 with silver nanoparticles) and, as a reference, to the mixed fiber filter (F1). The growth of the bacteria was not inhibited by the reference materials, which was to be expected. On the other hand, the silver nanofibers and nanoparticles showed significant increase of anti-bacterial activity against *E. coli* and a more moderate one against *S. aureus*. The difference between the two morphologies clearly has an effect on the antibacterial activity, as it cannot be explained by the equal amount of silver present in the filters. A larger material matrix should be tested to further identify the underlying reasons for this difference in the anti-bacterial activity.

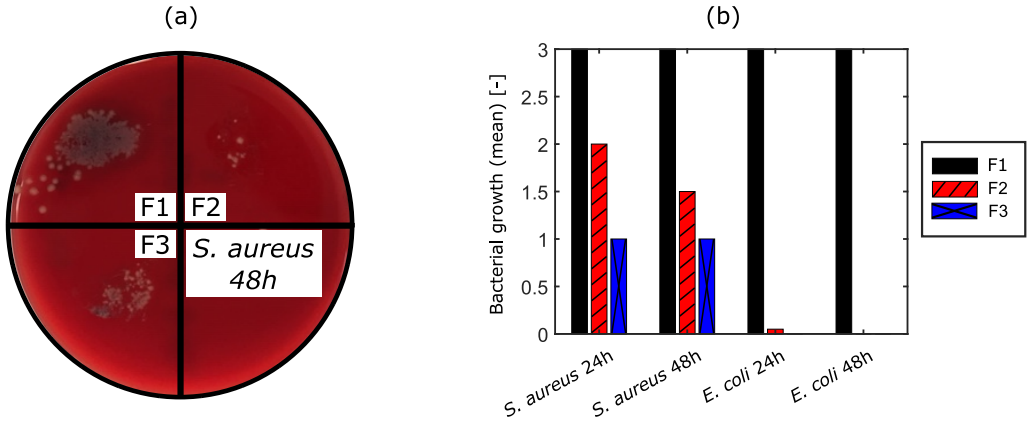

Figure 4.16: Anti-bacterial activity of the produced filters: (a) an example of the 48h incubated *S. aureus* on a blood agar plate and (b) the bacterial growths for both bacteria species with 24 and 48h incubation times tested with touch test. Results show the decrease in the growth of bacteria when silver fibers or nanoparticles are added to the filter media. The growth of the *E. coli* has almost completely been inhibited. F1 denotes the mixed fiber filter, F2 the silver nanofiber containing filter and F3 the silver nanoparticle containing filter. (Adapted from **Paper IV**)

5 Conclusions and Future Outlook

The synthesis of nanoparticles and their incorporation to new materials is a ever-growing field. One approach for the generation of nanoparticles is to use gas-phase synthesis route. For a complete understanding of nanoparticle synthesis and its applications, the whole synthesis process needs to be considered. Having a requirement for nanoparticles from the application end warrants knowledge from the point of view of synthesis. Additionally, measurement capability is needed to verify that the desired properties have been created. In this thesis the whole process has been studied, from the fundamental force interactions and parameters describing nanoparticles to monitored application of nanoparticles in functional coatings. A new instrument, DENSMO, was developed to monitor effective density, a precursor used by LFS was optimized to produce less residual particles, and two functional coatings were realized to bring anti-icing and anti-bacterial properties to material surfaces.

As the effective density of particles can tell quite a lot about the ongoing process and the structure of the produced particles, an instrument was developed to measure this quantity. Effective density can be measured with rather complex setups, but in **Paper I** the aim was to have a structurally simple sensor-type instrument that could be used for synthesis monitoring. The utilization of a mobility analyzer and a low pressure impactor to measure nanoparticles charged with a corona charger was the way to go. The calibration of this instrument also enabled the more in-depth synthesis control of the morphology of nanoparticles.

The synthesis optimization continued on the front of flame-generated nanoparticles. Producing higher quantities of nanoparticles cost-effectively can bring upon the problem of residual particles. Liquid precursors with low volatility can generate particles with a liquid-to-particle route instead of gas-to-particle, where the former typically produces particles in the micron range and the latter from individual atoms upwards to nanoparticles. In order to rid the nanoparticle synthesis process of these unwanted residual particles, EHA was added to the precursor to increase the available burning enthalpy, which in turn enabled the complete evaporation of the precursor droplets. With this approach, orders of magnitude more nanoparticles were able to be produced in **Paper II** without other changes to the synthesis setup.

Combining this high yield synthesis process with the structuring of surfaces made possible the creation of porous coatings for SLIPS applications in **Paper III**. The nanoparticle coating can have excess of 90% porosity, giving ample room for a lubricant to fill and move in the structure. Anything on top of this kind of coating has little contact to a solid structure, facilitating low adhesion of water and ice. Even though the produced coating is not superhydrophilic, the achieved low ice adhesion strength value is really competitive for a method that is so scalable and tunable. The coating can be applied to surfaces that

normally are considered not thermally robust, such as paper and plastics, as well as to the more obvious metals and glass. The variety of available precursors for the flame synthesis also leaves the material choice to be determined by the requirements of the application.

The wide range of possibilities for the synthesis of nanoparticles increases the need to measure and monitor the process. Synthesis monitoring was utilized in **Paper IV** during the functionalization of fiber filters, where a silver nanoparticle coating was used to add anti-bacterial properties. The mass loading and nanoparticle diameter were monitored to get a specified coating for comparable anti-bacterial testing. The tested silver nanoparticle-coated filter media showed a clear decrease in the growth of *S. aureus* and *E. coli*, eradicating the latter almost completely.

As such a wide field was studied, even though the results presented in this thesis are important on their own right, they also give a good starting point for further research. To start with, the measurement technology developed here has a lot of potential in synthesis monitoring and in instrument development, optimization of the response functions and data inversion being just a few possible directions. Additionally, the need for more nanomaterials in the future is sure to grow, thus increasing the need for high output and controllable synthesis methods, along with monitoring capabilities. New materials and combinations of materials are almost guaranteed to bring new challenges and opportunities with them, so material synthesis-based research will positively thrive in the future. Specific questions left in the wake of this thesis include: what is the optimal nanoparticle coating for anti-bacterial effect and what other materials can be used instead of silver, how can the SLIPS structure be improved and what requirements they have on the scaling-up of the process? In the end, there are several interesting research paths to be explored by future studies.

Bibliography

Aitken, J., "On the number of dust particles in the atmosphere," *Nature*, vol. 37, pp. 428 – 430, 1888.

Aitken, R. J., Chaudhry, M. Q., Boxall, A. B. A., and Hull, M., "Manufacture and use of nanomaterials: current status in the UK and global trends," *Occupational Medicine*, vol. 56, no. 5, pp. 300–306, 08 2006.

Alcock, C. B., Itkin, V. P., and Horrigan, M. K., "Vapour pressure equations for the metallic elements: 298-2500k," *Canadian Metallurgical Quarterly*, vol. 23, no. 3, pp. 309–313, 1984.

Allen, M. D. and Raabe, O. G., "Slip correction measurements of spherical solid aerosol particles in an improved millikan apparatus," *Aerosol Science and Technology*, vol. 4, no. 3, pp. 269–286, 1985.

Arffman, A., Kuuluvainen, H., Harra, J., Vuorinen, O., Juuti, P., Yli-Ojanperä, J., Mäkelä, J. M., and Keskinen, J., "The critical velocity of rebound determined for sub-micron silver particles with a variable nozzle area impactor," *Journal of Aerosol Science*, vol. 86, pp. 32–43, 2015.

Aromaa, M., Arffman, A., Suhonen, H., Haapanen, J., Keskinen, J., Honkanen, M., Nikkanen, J.-P., Levänen, E., Messing, M., Deppert, K., Teisala, H., Tuominen, M., Kuusipalo, J., Stepien, M., Saarinen, J., Toivakka, M., and Mäkelä, J., "Atmospheric synthesis of superhydrophobic tio_2 nanoparticle deposits in a single step using liquid flame spray," *Journal of Aerosol Science*, vol. 52, pp. 57–68, 2012.

Baron, P. A., "Calibration and use of the aerodynamic particle sizer (aps 3300)," *Aerosol Science and Technology*, vol. 5, no. 1, pp. 55–67, 1986.

Baskaran, M. and Shaw, G. E., "Residence time of arctic haze aerosols using the concentrations and activity ratios of 210po, 210pb and 7be," *Journal of Aerosol Science*, vol. 32, no. 4, pp. 443 – 452, 2001.

Beemer, D. L., Wang, W., and Kota, A. K., "Durable gels with ultra-low adhesion to ice," *J. Mater. Chem. A*, vol. 4, pp. 18 253–18 258, 2016.

Bhattacharya, S., Sridevi, S., and Pitchiah, R., "Indoor air quality monitoring using wireless sensor network," in *2012 Sixth International Conference on Sensing Technology (ICST)*, Dec 2012, pp. 422–427.

Brobbey, K. J., Haapanen, J., Gunell, M., Mäkelä, J. M., Eerola, E., Toivakka, M., and Saarinen, J. J., "One-step flame synthesis of silver nanoparticles for roll-to-roll

production of antibacterial paper," *Applied Surface Science*, vol. 420, pp. 558 – 565, 2017.

Bushell, G., Yan, Y., Woodfield, D., Raper, J., and Amal, R., "On techniques for the measurement of the mass fractal dimension of aggregates," *Advances in Colloid and Interface Science*, vol. 95, no. 1, pp. 1 – 50, 2002.

Chen, M., Romay, F. J., Li, L., Naqwi, A., and Marple, V. A., "A novel quartz crystal cascade impactor for real-time aerosol mass distribution measurement," *Aerosol Science and Technology*, vol. 50, no. 9, pp. 971–983, 2016.

Chen, T. M. and Chein, H. M., "Generation and evaluation of monodisperse sodium chloride and oleic acid nanoparticles," *Aerosol and Air Quality Research*, vol. 6, no. 3, pp. 305–321, 2006.

Choi, H.-J., Kumita, M., Hayashi, S., Yuasa, H., Kamiyama, M., Seto, T., Tsai, C.-J., and Otani, Y., "Filtration properties of nanofiber/microfiber mixed filter and prediction of its performance," *Aerosol and Air Qual. Res.*, vol. 17, pp. 1052–1062, 2017.

Cui, C., Gan, L., Heggen, M., Rudi, S., and Strasser, P., "Compositional segregation in shaped pt alloy nanoparticles and their structural behaviour during electrocatalysis," *Nature Materials*, vol. 12, pp. 765 EP –, Jun 2013.

David, A. and Fraser, M., "The collection of submicron particles by electrostatic precipitation," *American Industrial Hygiene Association Quarterly*, vol. 17, no. 1, pp. 75–79, 1956, pMID: 13292367.

Davis, E. J., "A history of single aerosol particle levitation," *Aerosol Science and Technology*, vol. 26, no. 3, pp. 212–254, 1997.

DeCarlo, P. F., Slowik, J. G., Worsnop, D. R., Dovidovits, P., and Jimenez, J. L., "Particle morphology and density characterization by combined mobility and aerodynamic diameter measurements. part 1: Theory," *Aerosol Science and Technology*, vol. 38, pp. 1185–1205, 2004.

Deppert, K. and Wiedensohler, A., "Aerosol particles from bubblers in metalorganic vapor phase epitaxy," *Cryst. Res. Technol.*, vol. 29, pp. 613–616, 1994.

Didenko, Y. T. and Suslick, K. S., "Chemical aerosol flow synthesis of semiconductor nanoparticles," *Journal of the American Chemical Society*, vol. 127, no. 35, pp. 12 196–12 197, 2005.

Dunning, W. J., "Nucleation; homogeneous and heterogeneous. nucleation processes and aerosol formation," *Discuss. Faraday Soc.*, vol. 30, pp. 9–19, 1960.

Einstein, A., "Investigations on the theofy of the brownian movement," *Ann. der Physik*, vol. -, pp. –, 1905.

Friedlander, S. K., "Dynamics of aerosol formation by chemical reaction," *Annals of the New York Academy of Sciences*, vol. 404, no. 1, pp. 354–364, 1983.

Fuchs, N. A., *The mechanics of aerosols*. Oxford: Pergamon press, 1964.

Gunell, M., Haapanen, J., Brobbey, K., Saarinen, J., Toivakka, M., Mäkelä, J., Huovinen, P., and Eerola, E., "Antimicrobial characterization of silver nanoparticle-coated surfaces by "touch test" method," *Nanotechnology, Science and Applications*, vol. 10, pp. 137–145, 2017.

Guo, S., Li, D., Zhang, L., Li, J., and Wang, E., "Monodisperse mesoporous superparamagnetic single-crystal magnetite nanoparticles for drug delivery," *Biomaterials*, vol. 30, no. 10, pp. 1881 – 1889, 2009.

Gurav, A., Kodas, T., Pluym, T., and Xiong, Y., "Aerosol processing of materials," *Aerosol Sci. Technol.*, vol. 19, pp. 411–452, 1993.

Haapanen, J., Aromaa, M., Teisala, H., Tuominen, M., Stepien, M., Saarinen, J., Heikkilä, M., Toivakka, M., Kuusipalo, J., and Mäkelä, J., "Binary tio2/sio2 nanoparticle coating for controlling the wetting properties of paperboard," *Materials Chemistry and Physics*, vol. 149-150, pp. 230 – 237, 2015.

Haapanen, J., Aromaa, M., Teisala, H., Juuti, P., Tuominen, M., Sillanpää, M., Stepien, M., Saarinen, J. J., Toivakka, M., Kuusipalo, J. *et al.*, "On the limit of superhydrophobicity: defining the minimum amount of tio2 nanoparticle coating," *Materials Research Express*, vol. 6, no. 3, p. 035004, 2018.

Harra, J., Mäkitalo, J., Siikanen, R., Virkki, M., Genty, G., Kobayashi, T., Kauranen, M., and Mäkelä, J. M., "Size-controlled aerosol synthesis of silver nanoparticles for plasmonic materials," *Journal of Nanoparticle Research*, vol. 14, no. 6, p. 870, Jun 2012.

Harra, J., Juuti, P., Haapanen, J., Sorvali, M., Roumeli, E., Honkanen, M., Vippola, M., Yli-Ojanperä, J., and Mäkelä, J. M., "Coating of silica and titania aerosol nanoparticles by silver vapor condensation," *Aerosol Science and Technology*, vol. 49, no. 9, pp. 767–776, 2015.

Hawkes, P. and Reimer, L., *Scanning Electron Microscopy: Physics of Image Formation and Microanalysis*, ser. Springer Series in Optical Sciences. Springer Berlin Heidelberg, 2013.

Haynes, W. M., Ed., *CRC Handbook of Chemistry and Physics*, 96th ed. Boca Raton, FL: CRC Press/Taylor and Francis, 2016.

Heath, J. R., Shiang, J. J., and Alivisatos, A. P., "Germanium quantum dots: Optical properties and synthesis," *The Journal of Chemical Physics*, vol. 101, no. 2, pp. 1607–1615, 1994.

Hewitt, G. W., "The charging of small particles for electrostatic precipitation," *Transactions of the American Institute of Electrical Engineers, Part I: Communication and Electronics*, vol. 76, no. 3, pp. 300–306, 1957.

Hinds, W. C., *Aerosol Technology: Properties, Behavior, and Measurement of Airborne Particles*, 2nd ed. New York, NY: John Wiley & Sons, Inc., 1999.

Honkanen, M., Kärkkäinen, M., Kolli, T., Heikkinen, O., Viitanen, V., Zeng, L., Jiang, H., Kallinen, K., Huuhtanen, M., Keiski, R. L., Lahtinen, J., Olsson, E., and Vippola, M., "Accelerated deactivation studies of the natural-gas oxidation catalyst–verifying the role of sulfur and elevated temperature in catalyst aging," *Applied Catalysis B: Environmental*, vol. 182, pp. 439 – 448, 2016.

Jadhav, S., Gaikwad, S., Nimse, M., and Rajbhoj, A., "Copper oxide nanoparticles: Synthesis, characterization and their antibacterial activity," *Journal of Cluster Science*, vol. 22, no. 2, pp. 121–129, Jun 2011.

Järvinen, A., Aitomaa, M., Rostedt, A., Keskinen, J., and Yli-Ojanperä, J., "Calibration of the new electrical low pressure impactor (ELPI+)," *Journal of Aerosol Science*, vol. 69, pp. 150–159, 2014.

Järvinen, A., Keskinen, J., and Yli-Ojanperä, J., "Extending the faraday cup aerosol electrometer based calibration method up to 5 um," *Aerosol Science and Technology*, vol. 52, no. 8, pp. 828–840, 2018.

Jayaratne, E. R., Ling, X., and Morawska, L., "Charging state of aerosols during particle formation events in an urban environment and its implications for ion-induced nucleation," *Aerosol and Air Quality Research*, vol. 16, no. 2, pp. 348–360, 2016.

Kelly, W. P. and McMurry, P. H., "Measurement of particle density by inertial classification of differential mobility analyzer-generated monodisperse aerosols," *Aerosol Science and Technology*, vol. 17, no. 3, pp. 199–212, 1992.

Keskinen, J., Pietarinen, K., and Lehtimäki, M., "Electrical low pressure impactor," *J. Aerosol Sci.*, vol. 23, pp. 353–360, 1992.

Kim, P., Wong, T.-S., Alvarenga, J., Kreder, M., Adorno-Martinez, W., and Aizenberg, J., "Liquid-infused nanostructured surfaces with extreme anti-ice and anti-frost performance," *ACS Nano*, vol. 6, pp. 6569–6577, 2012.

Koch, W. and Friedlander, S., "The effect of particle coalescence on the surface area of a coagulating aerosol," *Journal of Colloid and Interface Science*, vol. 140, no. 2, pp. 419–427, 1990.

Koivuluoto, H., Stenroos, C., Ruohomaa, R., Bolelli, G., Lusvarghi, L., and Vuoristo, P., "Research on icing behavior and ice adhesion testing of icephobic surfaces," in *Proceedings of 16th international workshop on atmospheric icing of structures*, Uppsala, Sweden, 28 June – July 3 2015, pp. 183 – 188.

Kulkarni, P., Baron, P. A., and Willeke, K., Eds., *Aerosol Measurement: Principles, Techniques, and Applications*, 3rd ed. Hoboken, NJ: John Wiley & Sons, Inc., 2011.

Kutsovsky, Y., "Industrialization of fine-particle-based "products by process" to enable demanding customer applications," in *Xth International Aerosol Conference*, 2018.

Kuuluvainen, H., Arffman, A., Saukko, E., Virtanen, A., and Keskinen, J., "A newmethod for characterizing the bounce and charge transfer properties of nanoparticles," *Journal of Aerosol Science*, vol. 55, pp. 104–115, 2013.

Liu, B. Y. H. and Lee, K. W., "An aerosol generator of high stability," *American Industrial Hygiene Association Journal*, vol. 36, no. 12, pp. 861–865, 1975, pMID: 1211356.

Liu, B. Y. and Pui, D. Y., "A submicron aerosol standard and the primary, absolute calibration of the condensation nuclei counter," *Journal of Colloid and Interface Science*, vol. 47, no. 1, pp. 155 – 171, 1974.

Mädler, L., "Liquid-fed aerosol reactors for one-step synthesis of nano-structured particles," *KONA Powder Part. J.*, vol. 22, pp. 107–120, 2004.

Mädler, L., Krumeich, F., Burtscher, P., and Moszner, N., "Visibly transparent & radiopaque inorganic organic composites from flame-made mixed-oxide fillers," *Journal of Nanoparticle Research*, vol. 8, no. 3, pp. 323–333, Aug 2006.

Magnusson, M. H., Deppert, K., Malm, J.-O., Bovin, J.-O., and Samuelson, L., "Gold nanoparticles: Production, reshaping, and thermal charging," *Journal of Nanoparticle Research*, vol. 1, no. 2, pp. 243–251, Jun 1999.

Maile, F. J., Pfaff, G., and Reynders, P., "Effect pigments–past, present and future," *Progress in Organic Coatings*, vol. 54, no. 3, pp. 150 – 163, 2005.

Mäkelä, J. M., Aromaa, M., Rostedt, A., Krinke, T., Janka, K., Marjamäki, M., and Keskinen, J., "Liquid flame spray for generating metal and metal oxide nanoparticle test aerosol," *Human & Experimental Toxicology*, vol. 28, no. 6-7, pp. 421–431, 2009, pMID: 19755455.

Mäkelä, J., Haapanen, J., Harra, J., Juuti, P., and Kujanpää, S., "Liquid flame spray – A hydrogen-oxygen flame based method for nanoparticle synthesis and functional nanocoatings," *KONA Powder and particle journal*, vol. 34, pp. 141–154, 2017.

Maness, P.-C., Smolinski, S., Blake, D. M., Huang, Z., Wolfrum, E. J., and Jacoby, W. A., "Bactericidal activity of photocatalytic tio2 reaction: toward an understanding of its killing mechanism," *Applied and Environmental Microbiology*, vol. 65, no. 9, pp. 4094–4098, 1999.

Marjamäki, M., Keskinen, J., Chen, D.-R., and Pui, D. Y., "Performance evaluation of the electrical low-pressure impactor (ELPI)," *Journal of Aerosol Science*, vol. 31, no. 2, pp. 249 – 261, 2000.

Marple, V. A. and Willeke, K., "Impactor design," *Atmospheric Environment (1967)*, vol. 10, no. 10, pp. 891 – 896, 1976.

McMurry, P. H., "The history of condensation nucleus counters," *Aerosol Science and Technology*, vol. 33, no. 4, pp. 297–322, 2000.

Mock, J. J., Barbic, M., Smith, D. R., Schultz, D. A., and Schultz, S., "Shape effects in plasmon resonance of individual colloidal silver nanoparticles," *The Journal of Chemical Physics*, vol. 116, no. 15, pp. 6755–6759, 2002.

Morones, J. R., Elechiguerra, J. L., Camacho, A., Holt, K., Kouri, J. B., Ramírez, J. T., and Yacaman, M. J., "The bactericidal effect of silver nanoparticles," *Nanotechnology*, vol. 16, no. 10, pp. 2346–2353, aug 2005.

Niemelä-Anttonen, H., Koivuluoto, H., Tuominen, M., Teisala, H., Juuti, P., Haapanen, J., Harra, J., Stenroos, C., Lahti, J., Kuusipalo, J., Mäkelä, J. M., and Vuoristo, P., "Icephobicity of slippery liquid infused porous surfaces under multiple freeze-thaw and ice accretion-detachment cycles," *Advanced Materials Interfaces*, vol. 5, no. 20, p. 1800828, 2018.

Nikkanen, J.-P., Heinonen, S., Saarivirta, E. H., Honkanen, M., and Levänen, E., "Photocatalytically active titanium dioxide nanopowders: Synthesis, photoactivity and magnetic separation," *IOP Conference Series: Materials Science and Engineering*, vol. 47, p. 012066, dec 2013.

Okuyama, K. and Lenggoro, I. W., "Preparation of nanoparticles via spray route," *Chemical Engineering Science*, vol. 58, no. 3, pp. 537 – 547, 2003, 17th International Symposium of Chemical Reaction Engineering (IS CRE 17).

Onasch, T. B., Trimborn, A., Fortner, E. C., Jayne, J. T., Kok, G. L., Williams, L. R., Davidovits, P., and Worsnop, D. R., "Soot particle aerosol mass spectrometer: Development, validation, and initial application," *Aerosol Science and Technology*, vol. 46, no. 7, pp. 804–817, 2012.

Pitkänen, A., Mäkelä, J. M., Nurminen, M., Oksanen, A., Janka, K., Keskinen, J., Keskinen, H., Liimatainen, J. K., S., H., and Määttä, T., "Numerical study of silica particle formation in turbulent h2/o2 flame," *IFRF Combustion journal*, vol. 200509, p. 29, 2005.

Pratsinis, S. E., "Flame aerosol synthesis of ceramic powders," *Progress in Energy and Combustion Science*, vol. 24, no. 3, pp. 197 – 219, 1998.

Rayleigh, F., "On the equilibrium of liquid conducting masses charged with electricity," *The London, Edinburgh, and Dublin Philosophical Magazine and Journal of Science*, vol. 14, no. 87, pp. 184–186, 1882.

Ristimäki, J., Virtanen, A. Marjamäki, M., Rostedt, A., and Keskinen, J., "On-line measurement of size distribution and effective density of submicron aerosol particles," *Journal of Aerosol Science*, vol. 33, no. 11, pp. 1541–1557, 2002.

Rosebrock, C. D., Riefler, N., Wriedt, T., Mädler, L., and Tse, S. D., "Disruptive burning of precursor/solvent droplets in flame-spray synthesis of nanoparticles," *AIChE J.*, vol. 59, pp. 4553–4566, 2013.

Rostedt, A., Marjamäki, M., and Keskinen, J., "Modification of the ELPI to measure mean particle effective density in real-time," *J. Aerosol Sci.*, vol. 40, pp. 823–831, 2009.

Rostedt, A., Ntziachristos, L. D., Simonen, P., Rönkkö, T., Samaras, Z. C., Hillamo, R., Janka, K., and Keskinen, J., "A new miniaturized sensor for ultra-fast on-board soot concentration measurements," *SAE International Journal of Engines*, vol. 10, no. 4, 3 2017.

Ruppecht, E., Meyer, M., and Patashnick, H., "The tapered element oscillating microbalance as a tool for measuring ambient particulate concentrations in real time," *Journal of Aerosol Science*, vol. 23, pp. 635 – 638, 1992, proceedings of the 1992 European Aerosol Conference.

Sahu, M. and Biswas, P., "Size distributions of aerosols in an indoor environment with engineered nanoparticle synthesis reactors operating under different scenarios," *Journal of Nanoparticle Research*, vol. 12, no. 3, pp. 1055–1064, Mar 2010.

Schaefer, D. W. and Hurd, A. J., "Growth and structure of combustion aerosols: fumed silica," *Aerosol Science and Technology*, vol. 12, no. 4, pp. 876–890, 1990.

Scheibel, H. and Porstendörfer, J., "Generation of monodisperse ag- and nacl-aerosols with particle diameters between 2 and 300 nm," *Journal of Aerosol Science*, vol. 14, no. 2, pp. 113 – 126, 1983.

Sciau, P., "Nanoparticles in ancient materials: The metallic lustre decorations of medieval ceramics," in *The Delivery of Nanoparticles*, Hashim, A. A., Ed. Rijeka: IntechOpen, 2012, ch. 25.

Shin, W. G., Pui, D. Y. H., Fissan, H., Neumann, S., and Trampe, A., *Calibration and numerical simulation of Nanoparticle Surface Area Monitor (TSI Model 3550 NSAM)*. Dordrecht: Springer Netherlands, 2007, pp. 61–69.

Sirelkhatim, A., Mahmud, S., Seeni, A., Kaus, N. H. M., Ann, L. C., Bakhori, S. K. M., Hasan, H., and Mohamad, D., "Review on zinc oxide nanoparticles: Antibacterial activity and toxicity mechanism," *Nano-Micro Letters*, vol. 7, no. 3, pp. 219–242, Jul 2015.

Skillas, G., Künzel, S., Burtscher, H., Baltensperger, U., and Siegmann, K., "High fractal-like dimension of diesel soot agglomerates," *Journal of Aerosol Science*, vol. 29, no. 4, pp. 411–419, 1998.

Sorvali, M., Vuori, L., Pudas, M., Haapanen, J., Mahlberg, R., Ronkainen, H., Honkanen, M., Valden, M., and Mäkelä, J., "Fabrication of ultrathin multilayered superomniphobic nanocoatings by liquid flame spray, atomic layer deposition and silanization," *Nanotechnology*, vol. 29, p. 185708, feb 2018.

Sotiriou, G. A. and Pratsinis, S. E., "Antibacterial activity of nanosilver ions and particles," *Environmental Science & Technology*, vol. 44, no. 14, pp. 5649–5654, 2010.

Stark, W. J., Stoessel, P. R., Wohlleben, W., and Hafner, A., "Industrial applications of nanoparticles," *Chem. Soc. Rev.*, vol. 44, pp. 5793–5805, 2015.

Stark, W. J. and Pratsinis, S. E., "Aerosol flame reactors for manufacture of nanoparticles," *Powder Technology*, vol. 126, no. 2, pp. 103 – 108, 2002.

Steinle, S., Reis, S., Sabel, C. E., Semple, S., Twigg, M. M., Braban, C. F., Leeson, S. R., Heal, M. R., Harrison, D., Lin, C., and Wu, H., "Personal exposure monitoring of pm2.5 in indoor and outdoor microenvironments," *Science of The Total Environment*, vol. 508, pp. 383 – 394, 2015.

Stepien, M., Chinga-Carrasco, G., Saarinen, J. J., Teisala, H., Tuominen, M., Aromaa, M., Haapanen, J., Kuusipalo, J., Mäkelä, J. M., and Toivakka, M., "Wear resistance of nanoparticle coatings on paperboard," *Wear*, vol. 307, no. 1, pp. 112 – 118, 2013.

Strobel, R. and Pratsinis, S. E., "Effect of solvent composition on oxide morphology during flame spray pyrolysis of metal nitrates," *Phys. Chem. Chem. Phys.*, vol. 13, pp. 9246–9252, 2011.

Strobel, R., Alfons, A., and Pratsinis, S. E., "Aerosol flame synthesis of catalysts," *Advanced Powder Technology*, vol. 17, no. 5, pp. 457 – 480, 2006.

Suja, F., Pramanik, B. K., and Zain, S. M., "Contamination, bioaccumulation and toxic effects of perfluorinated chemicals (PFCs) in the water environment: a review paper," *Water Science and Technology*, vol. 60, no. 6, pp. 1533–1544, 09 2009.

Sun, J., Zhang, J., Zhang, M., Antonietti, M., Fu, X., and Wang, X., "Bioinspired hollow semiconductor nanospheres as photosynthetic nanoparticles," *Nature Communications*, vol. 3, pp. 1139 EP –, Oct 2012.

Talbot, L., Cheng, R. K., Schefer, R. W., and Willis, D. R., "Thermophoresis of particles in a heated boundary layer," *Journal of Fluid Mechanics*, vol. 101, no. 4, pp. 737 – 758, 1980.

Tammet, H., Mirme, A., and Tamm, E., "Electrical aerosol spectrometer of Tartu University," *Atmospheric Research*, vol. 62, no. 3, pp. 315 – 324, 2002.

Teisala, H., Geyer, F., Haapanen, J., Juuti, P., Mäkelä, J., Vollmer, D., and Butt, H.-J., "Ultrafast processing of hierarchical nanotexture for a transparent superamphiphobic coating with extremely low roll-off angle and high impalement pressure," *Advanced materials*, vol. 30, p. 1706529, 2018.

Tenover, F. C., "Mechanisms of antimicrobial resistance in bacteria," *The American Journal of Medicine*, vol. 119, no. 6, Supplement 1, pp. S3 – S10, 2006, antimicrobial Resistance Prevention Initiative: Proceedings of an Expert Panel on Resistance.

Tikkanen, J., Gross, K. A., Berndt, C. C., Pitkänen, V., Keskinen, J., Raghu, S., Rajala, M., and Karthikeyan, J., "Characteristics of the liquid flame spray process," *Surf. Coat. Technol.*, vol. 90, pp. 210 – 216, 1997.

van Gulijk, C., Marijnissen, J., Makkee, M., and Moulijn, J., "Oil-soaked sintered impactors for the elpi in diesel particulate measurements," *Journal of Aerosol Science*, vol. 34, no. 5, pp. 635 – 640, 2003.

Virtanen, A., Ristimäki, J., and Keskinen, J., "Method for measuring effective density and fractal dimension of aerosol agglomerates," *Aerosol Science and Technology*, vol. 38, no. 5, pp. 437 – 446, 2004.

Waldmann, L. and Schmitt, K., "Thermophoresis and diffusiophoresis of aerosols," in *Aerosol science*. Academic Press New York, 1966, vol. 137.

Wang, S. C. and Flagan, R. C., "Scanning electrical mobility spectrometer," *Aerosol Sci. Technol.*, vol. 13, pp. 230 – 240, 1990.

Wiedensohler, A. and Fissan, H. J., "Bipolar charge distributions of aerosol particles in high-purity argon and nitrogen," *Aerosol Science and Technology*, vol. 14, no. 3, pp. 358 – 364, 1991.

Winklmayr, W., Wang, H.-C., and John, W., "Adaptation of the twomey algorithm to the inversion of cascade impactor data," *Journal of Aerosol Science*, vol. 13, no. 3, pp. 322 – 331, 1990.

Yli-Ojanperä, J., Mäkelä, J. M., Marjamäki, M. Rostedt, A., and Keskinen, J., "Towards traceable particle number concentration standard: Single charged aeerosol reference (scar)," *Journal of Aerosol Science*, vol. 40, no. 8, pp. 719 – 728, 2010.

Young, T., "Iii. an essay on the cohesion of fluids," *Philosophical Transactions of the Royal Society of London*, vol. 95, pp. 65 – 87, Jan 1805.

Zheng, J., Zhang, C., and Dickson, R. M., "Highly fluorescent, water-soluble, size-tunable gold quantum dots," *Phys. Rev. Lett.*, vol. 93, p. 077402, Aug 2004.

Publications

Paper
I

Real-time effective density monitor (DENSMO) for aerosol nanoparticle production

Juuti, P., Arffman, A., Rostedt, A., Harra, J., Mäkelä, J.M. & Keskinen, J.

Aerosol Science and Technology, 2016, 50:5, 487 – 496
DOI: 10.1080/02786826.2016.1168511

I

Real-time effective density monitor (DENSMO) for aerosol nanoparticle production

Paxton Juuti*, Anssi Arffman, Antti Rostedt, Juha Harra, Jyrki M. Mäkelä, Jorma Keskinen

Department of Physics, Aerosol Physics Laboratory, Tampere University of Technology, P.O. Box 692, 33101 Tampere, Finland

Abstract

A new instrument, Density monitor (DENSMO), for aerosol particle size distribution characterization and monitoring has been developed. DENSMO is operationally simple and capable of measuring the effective density as well as the aerodynamic and the mobility median diameters with a time resolution of one second, from unimodal particle size distributions. The characterization is performed with a zeroth order mobility analyzer in series with a low pressure impactor and a filter stage. The operation of DENSMO was investigated with sensitivity analysis and, based on the results, optimal operation parameters were determined. DENSMO was also compared, in lab test measurements, against a reference method with several particle materials with bulk densities from 0.92 to 10.5 g/cm^3. The results show that the deviation from the reference method was less than 25% for suitable materials.

1. Introduction

The use of aerosol nanoparticles in functional materials and commercially available products has increased as production routes, especially those employing the gas phase, have become more viable and more improved properties have been discovered (Aitken et al., 2006). The production of nanoparticles requires some form of quality control as well as analysis methods. This ensures the produced materials are up to standard. Control and analysis can be achieved with both offline and online methods. From these two, the online methods give access to immediate information on desired aspects of the process. When aerosol routes are being utilized, one suitable property to be monitored is the effective density. In situations where the value of the effective density changes, the monitored aerosol particles have

*Corresponding author
Email address: paxton.juuti@tut.fi (Paxton Juuti)

undergone morphological or chemical changes. For example, the change in the effective density has been recently used to determine the coating thickness of core-shell particles (Weis et al., 2015). These kind of shifts in the produced material do not necessarily exhibit changes in mass or diameter of the individual particles. For a more in-depth theoretical overview on the subject of the effective density, see DeCarlo et al. (2004). Typically, in order to determine the effective density, a set of two properties from the aerosol is required, such as the mobility and the aerodynamic median diameters.

One of the first approaches to measure the effective density was presented by Kelly & McMurry (1992), which consisted of impacting mobility selected particles. This paved the way for using multiple instruments in series in order to measure the effective density. The introduction of instruments capable of measuring mobility diameter, aerodynamic diameter, surface area and mass have further advanced the measurement routes for the effective density. Good examples of these kinds of instruments are Scanning Mobility Particle Sizer (SMPS; Wang & Flagan, 1990), Electrical Low Pressure Impactor (ELPI; Keskinen et al., 1992), Nanoparticle Surface Area Monitor (NSAM; TSI Inc.), Aerosol Particle Mass Analyzer (APM; Ehara et al., 1996) and Single Particle Laser Ablation Time-of-Flight Mass Spectrometer (SPLAT I; Zelenyuk & Imre, 2005). The measurement accurary and performance of these instruments have been improved since their introduction, for example by ELPI+ (Järvinen et al., 2014), SPLAT II (Zelenyuk et al., 2009) and Couette Centrifugal Particle Mass Analyzer (CPMA; Olfert & Collings, 2005). Various combinations of these devices and methods implementing them have been introduced. The background for this work originates from the SMPS+ELPI method presented by Ristimäki et al. (2002). There are various other methods, some of which are basing their operation on measuring mobility size and mass, e.g., Tandem Differential Mobility Analyzer (TDMA)+APM (McMurry et al., 2002), on mobility size and surface area, e.g., Condensation Particle Counter (CPC)+DMA+NSAM (Universal NanoParticle Analyzer; UNPA) (Wang et al., 2010), on mobility selection with supersonic impaction (e.g., Hering & Stolzenburg, 1995) and on mobility selection followed by aerodynamic characterization, e.g., DMA+SPLAT (Zelenyuk et al., 2005).

These complex and often expensive methods (as you need several standalone instruments) are not ideal for use in production facilities where it would be preferable to have monitoring on each individual production line. Some simplified versions of the previously mentioned methods have been introduced. For example, the SMPS+ELPI method has been a starting point for several simplifications, such as a modified ELPI, where several impactor stages were replaced with a mobility analyzer (Rostedt et al., 2009) and commercially available Dekati Mass Monitor (DMM, Dekati Ltd.), which focuses on the mass

measurement rather than the effective density. The DMM employs a similar construction as the modified ELPI, with the difference of having one impactor stage fewer and no filter stage. The main difference arises in the information given by these instruments: DMM provides the user with a mass and a number concentration, whereas the modified ELPI provides a mobility median and an aerodynamic current size distribution from the measured aerosol.

Here we present DENSMO (DENSity MOnitor). It was developed to be even simpler in construction and operational principle than the earlier SMPS+ELPI method variations and thus to be cheaper to manufacture and more suitable for widespread use. The aim was to reduce the amount of functional parts without losing much of the information acquirable and without compromising the reliability of the information. After introducing the operational principle and the construction of DENSMO, detailed calibration and sensitivity analysis results are presented. Fully characterized and calibrated DENSMO is then compared against the SMPS+ELPI method. Lastly, an example case of a real time measurement of silver nanoparticle sintering is presented.

2. Principle of operation

In order to quantify the effective density (ρ_{eff}), indirect measurements are needed. One route becomes apparent from the definition of the effective density, which relates aerodynamic (d_a) and mobility (d_b) diameters with the following equation:

$$\rho_{eff} = \rho_0 \frac{C_c(d_a) d_a^2}{C_c(d_b) d_b^2}, \tag{1}$$

where ρ_0 is the unit density (1 g/cm^3) and C_c is the Cunningham slip correction factor of the denoted characteristic diameter (Kelly & McMurry, 1992; Ristimäki et al., 2002). The mobility and aerodynamic diameters can be determined by utilizing a zeroth order mobility analyzer, a low pressure impactor and a filter stage. Utilization of these methods requires the aerosol to be unipolarly charged prior to the characterization and measurement of the three obtainable currents I_{1-3}, which is achieved here by utilizing a corona charger. The operation of the charger is quantified with its charging efficiency

$$Pn(d_b) = \frac{I(d_b)}{eQN(d_b)}, \tag{2}$$

where $I(d_b)$ is the produced current distribution, e is the elementary charge, Q is the volumetric flow of the aerosol and $N(d_b)$ is the number size distribution. This process is presented in a schematic view of DENSMO, which is shown in Figure 1.

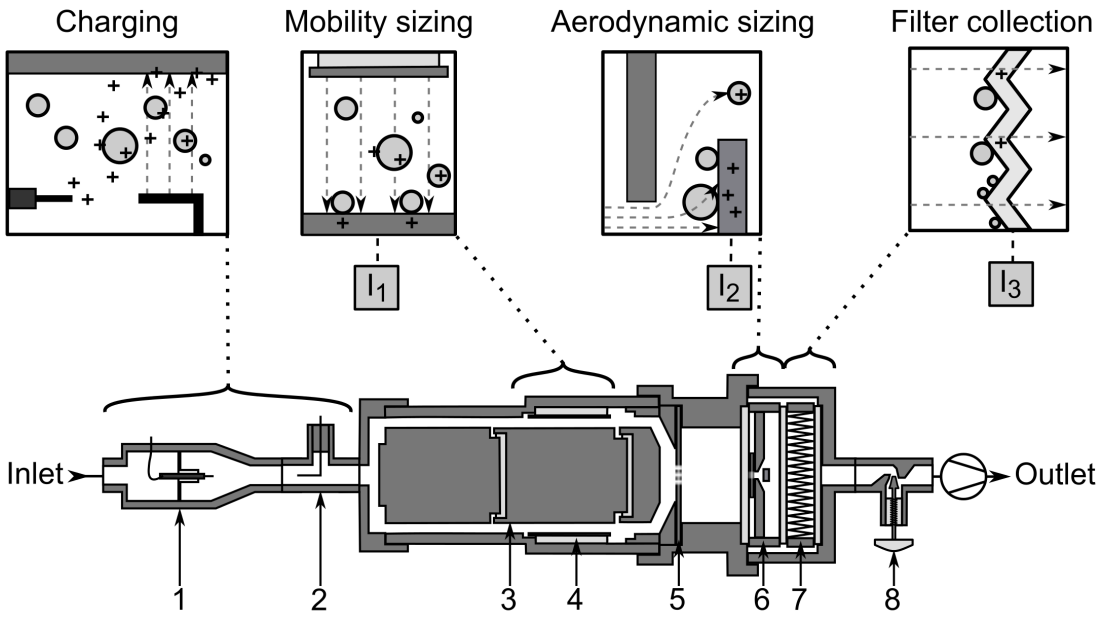

Figure 1: The upper part of the figure shows schematically how DENSMO operates from charging to mobility sizing and aerodynamic sizing and finally residual collection by the filter stage. Each of the measured currents has been depicted with the associated part of the process. The lower part of the figure illustrates a cross section of DENSMO with eight labeled operational sections: 1. Mini corona charger, 2. ion trap, 3. mobility analyzer collection cylinder, 4. mobility analyzer voltage cylinder, 5. critical orifice plate, 6. low pressure impactor, 7. filter and 8. needle valve.

Based on the previously presented approach and the schematic view in Figure 1, the measured aerosol, and the characterization of it, can be seen to follow the steps described below, where step 5 summarizes the rest of this section.

1. Unipolar charging of the aerosol
2. Mobility sizing with a constant electric field (current I_1)
3. Aerodynamic sizing with a low pressure impactor (current I_2)
4. Collecting the remaining particles with a filter stage (current I_3)
5. Calculation of collection efficiencies from I_{1-3}, followed by conversion to d_b, d_a and ρ_{eff}

In order to retrieve the diameter information from the mobility analyzer and the low pressure im-

pactor, the collection efficiencies (η) are needed, as a function of their respective characteristic diameters. Collection efficiency of the mobility analyzer (η_{ma}) can be theoretically formulated using its dimensions (length L, inner radius r_i and outer radius r_o; for values see Table 1), the voltage (U) being applied across the electrodes, the volumetric flow of the aerosol (Q) and the electrical mobility of the aerosol particles (Z) (Fuchs, 1964):

$$\eta_{ma}(d_b) = \frac{2\pi Z(d_b) U L}{Q ln\left(\frac{r_o}{r_i}\right)}. \tag{3}$$

The included electrical mobility is

$$Z(d_b) = \frac{n_{ave}(d_b)\, eC_c(d_b)}{3\pi\mu d_b}, \tag{4}$$

where n_{ave} is the average number of elementary charges on the aerosol particle with a diameter d_b and μ is the gas viscosity (Hinds, 1999). A commonly used fit function (Dzubay & Hasan, 1990) has been taken to characterize the collection efficiency of the low pressure impactor (η_{lpi}). The function is modified to include an offset factor to take into account the collection of sub-cut particles, enhanced by flow penetration into a porous collection surface:

$$\eta_{lpi}(d_a) = (1-\lambda)\left[1 + \left(\frac{d_{50}}{d_a}\right)^{2s}\right]^{-1} + \lambda, \tag{5}$$

where d_{50} is the cutpoint diameter of the collection efficiency curve, s is its steepness and λ is the offset factor (numerical value from 0 to 1), that sets the minimum collection efficiency value for the fit function (Dzubay & Hasan, 1990; Rao & Whitby, 1978a,b).

DENSMO measures number median diameters from aerosol particle distributions, which are integral quantities, therefore no information is gained from the finer structure of the distribution. This poses the following limitations to the measured aerosol particle distribution: unimodal log-normality and beforehand known or assumed geometric standard deviation (GSD). The determined characteristic diameters are thus the mobility equivalent median diameter and the aerodynamic median diameter.

The first of the three used integral values that can be obtained is the total current

$$I_{tot} = I_1 + I_2 + I_3 = \int Pn(d_b) eQN(d_b)\, dd_b = \int I(d_b)\, dd_b, \tag{6}$$

where I_1, I_2 and I_3 are the currents measured from the mobility analyzer, the low pressure impactor and the filter, respectively. The current fractions collected from the total available current distribution by the characterization zones can be calculated by utilizing the collection efficiencies of the mobility

analyzer and the low pressure impactor. The current fraction collected by the mobility analyzer is the second integral value and can be written as follows:

$$\eta_{ma,ave}(d_b) = \frac{I_1}{I_{tot}} = \frac{\int I(d_b)\,\eta_{ma}(d_b)\,dd_b}{\int I(d_b)\,dd_b}, \tag{7}$$

which links the median mobility size to the measured current fraction. A similar equation can be written for the third integral value, the current fraction of the low pressure impactor, and is as follows:

$$\begin{aligned}\eta_{lpi,ave}(d_b, \rho_{eff}) &= \frac{I_2}{I_2 + I_3} = \frac{I_2}{I_{tot} - I_1} \\ &= \frac{\int [I(d_b) - I(d_b)\eta_{ma}(d_b)]\,\eta_{lpi}(d_b, \rho_{eff})\,dd_b}{\int [I(d_b) - I(d_b)\eta_{ma}(d_b)]\,dd_b} \\ &= \frac{\int I(d_b)\,(1 - \eta_{ma}(d_b))\,\eta_{lpi}(d_b, \rho_{eff})\,dd_b}{\int I(d_b)\,(1 - \eta_{ma}(d_b))\,dd_b},\end{aligned} \tag{8}$$

which in turn links the median aerodynamic diameter to the corresponding current fraction. For the data processing, these relations are simulated to produce unique solutions for a certain parameter set of a geometric standard deviation, a low pressure impactor pressure and a mobility analyzer collection voltage.

By measuring the effective density with the method described above, utilizing three electrometers to measure the presented currents, one is able to retrieve median diameters from the measured currents in real-time. Section 3 contains a detailed description of the construction of DENSMO, including the mobility analyzer and the low pressure impactor, which are used for the main characterization.

3. Construction of DENSMO

DENSMO has been constructed so that the measured aerosol is conducted through one flow channel, where its charge state is first conditioned and then particle size characterized. A cross-sectional view of DENSMO is presented in Figure 1. After the inlet of DENSMO, the measured aerosol is charged with a small form factor unipolar corona charger, which has been designed to charge effectively in the nanometer scale. The charger is driven with a constant 1 µA current with a positive voltage around 2.5 kV. This charging approach is similar to the one implemented by Arffman et al. (2014). The excess ions are scavenged with the subsequent ion trap operating at 20 V, which creates a radial electric field from the electrode positioned on the centerline of the flow channel.

The characterization of the aerosol starts with the mobility analyzer, which collects aerosol particles based on their electrical mobility. The mobility analyzer has a radial electric field, which is produced by

applying a positive voltage in the outer electrode. This electric field guides the charged aerosol particles to an electrically floating collection cylinder from which the first current signal (I_1) is measured. After the mobility analyzer, the aerosol flow is choked with a plate with three critical 0.3 mm in diameter orifices, so that the volumetric flow rate stays at constant 1.65 lpm, even when the pressure of the low pressure impactor is altered. The next portion of the aerosol particles is collected with the low pressure impactor, which collects the aerosol particles based on their aerodynamic diameter. The aerosol particles are accelerated towards a sintered collection surface with 12 nozzles, each 0.3 mm in diameter. The collection stage is also in a floating potential to accommodate the measurement of the second current signal (I_2). The critical dimensions of the low pressure impactor have been designed specifically for this use, as the collection efficiency is desired to rise slowly over a wide particle size range. This has been achieved by a high jet-to-plate distance (S) to the nozzle diameter (W) ratio and with the utilization of sintered collection surface (Arffman et al., 2011). These critical dimensions, as well as those of the mobility analyzer, are presented in Table 1. The residual of the aerosol particles after the

Table 1: Critical dimensions and operational parameter ranges of the mobility analyzer (MA) and the low pressure impactor (LPI). From the MA, the collection volume length (L), inner diameter (r_i), outer diameter (r_o) and the range of collection voltage are listed. From the LPI, the jet-to-plate distance (S), nozzle throat length (T), individual nozzle diameter (W) and the range of upstream pressure are listed.

MA			LPI		
L	3.13	cm	S	3	mm
r_i	4.27	cm	W	0.3	mm
r_o	5.31	cm	T	0.1	mm
U	$10 - 150$	V	P	$200 - 300$	mbar

two characterization sections and the charge carried by the particles is collected on a high efficiency metal filter (Marjamäki et al., 2002). The third and last current signal (I_3) is measured from the filter, which is also electrically floating in its housing. The last operational section of DENSMO is a needle valve positioned after the filter, which is used to control the absolute pressure above and below the low pressure impactor. The control over the pressure is achieved by introducing another pressure drop in the valve, similar to the ones produced by the critical orifice plate and the low pressure impactor. These

operational sections create a stepwise drop in pressure from the atmospheric pressure to the applied low pressure in the outlet.

4. Calibration

The device functions of DENSMO were calibrated using SCAR (Single Charged Aerosol Reference) (Yli-Ojanperä et al., 2010), which produces monodisperse singly charged reference aerosol distributions from dioctyl sebacate (DOS). The calibration setup is depicted in Figure 2. The calibration was only

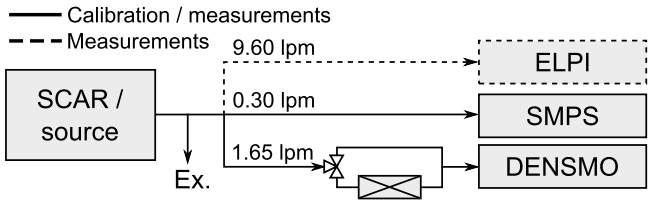

Figure 2: Calibration and measurement setups. The calibration setup includes, along with DENSMO, particle production by SCAR and a reference measurement with SMPS. During laboratory measurements, ELPI is also used.

performed against SMPS as the density of liquid DOS is known to be 0.92 g/cm^3 (CRC, 2009), and thus the aerodynamic diameter can be calculated from Equation 1. The charging efficiency (Pn) of the corona charger was calibrated as described by Marjamäki et al. (2000). It is the product of the particle penetration and charge state of the aerosol after the charger and is used here to simulate current distributions from number size distributions. The calibration results can be seen in Figure 3. The value of Pn can be seen dropping rapidly for particle sizes smaller than 35 nm. Because of this significantly weaker charging efficiency in this particle size range, these particles have only a small impact on the total collected current. When singly charged monodisperse aerosol is charged using the corona charger and measured by the mobility analyzer, n_{ave} is the only unknown parameter in Equation 3. These calibration results are also shown in Figure 3. A set of power functions were fitted to these calibration results and are as follows:

$$Pn(d_b) = \begin{cases} 3.07 \times 10^{-10} \times d_b^{6.086}, & d_b \leq 35 \text{ nm}, \\ 7.05 \times 10^{-4} \times d_b^{1.90}, & 35 \text{ nm} < d_b \leq 71 \text{ nm}, \\ 3.96 \times 10^{-3} \times d_b^{1.496}, & 71 \text{ nm} < d_b, \end{cases} \tag{9}$$

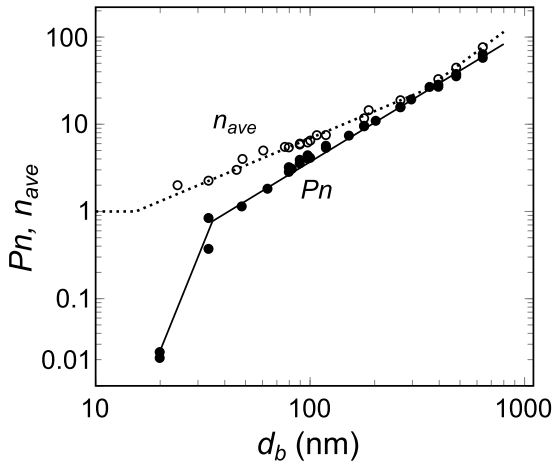

Figure 3: Charging efficiency of the mini corona charger and the average number of charges on a charged aerosol particle as a function of mobility diameter.

and

$$n_{ave}(d_b) = \begin{cases} 1, & d_b \leq 15.6 \text{ nm}, \\ 5.93 \times 10^{-2} \times d_b^{1.033}, & 15.6 < d_b \leq 361.0 \text{ nm}, \\ 6.30 \times 10^{-4} \times d_b^{1.812}, & 361.0 \text{ nm} \leq d_b. \end{cases} \tag{10}$$

The average number of charges is always greater in value than the Pn for a certain diameter, as the particle penetration of a charger can not exceed unity without it producing particles. The average number of charges is also limited to values higher than one as only charged particles are detected.

The calibration results of the mobility analyzer and the low pressure impactor are depicted in Figure 4. The mobility analyzer was calibrated using two different collection voltage (U) values: 50 and 150 V. Equation 3 was plotted alongside these calibration measurements, with the value of n_{ave} set to one. With these measurements, the functioning and scalability of the mobility analyzer, as predicted by theory, was verified with different collection voltages. The low pressure impactor was likewise calibrated for two different values, namely, upstream pressure (P) values at 200 and 300 mbar. Equation 5 was fitted to these calibration measurements and the parameter values are shown in Table 2. As hinted above, the collection efficiency of the low pressure impactor does not reach zero as the particle size decreases.

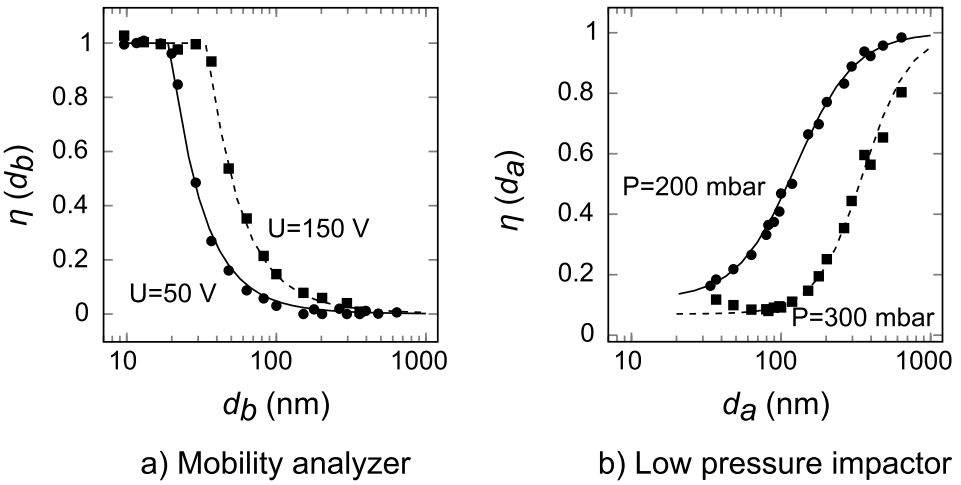

Figure 4: Collection efficiency measurement points for the mobility analyzer and the low pressure impactor. Solid and dashed lines show the theoretical collection efficiency curves of the mobility analyzer for 50 V and 150 V collection voltages, respectively. The curves fitted to the mobility analyzer measurements are from theory and only have one scaling parameter: the collection voltage. The solid and dashed curves fitted to the low pressure impactor measurements are from the fit function with pressure as the scaling parameter, 200 mbar and 300 mbar respectively, and three fitting parameters: slope, baseline offset and cutoff diameter.

This is due to secondary collection mechanisms, enhanced by flow penetration into the porous collection surface (see, e.g., Rao & Whitby, 1978a,b; Marjamäki & Keskinen, 2004). The secondary collection is expected to be increased for the smallest particles. In practice, however, they do not reach the impactor but are collected by the mobility analyzer. Therefore, the offset of Equation 5 was found to be sufficient to give good correlation with the measured data.

Unique sets of solutions can be calculated based on these calibrations and using Equations 7 and 8. One set of unique solutions as a function of the mobility median diameter for different effective densities is shown in Figure 5. Current measurements, and especially the collection efficiencies based on them, can now be linked explicitly to mobility and aerodynamic median diameters. The aerodynamic median diameter can be determined from the line corresponding to the unit density; alternatively, the effective density can be determined by identifying the line that crosses the collection efficiency value

Table 2: Fitting parameters of the collection efficiency curves of the low pressure impactor, where P is the used upstream pressure, s the steepness, d_{50} the cutpoint diameter and λ the baseline offset factor.

P (mbar)	s	d_{50}(nm)	λ
200	1.1	120.2	0.12
300	1.4	353.4	0.07

of the low pressure impactor at the measured mobility median diameter. For example, at a mobility median diameter of 90 nm, 60% collection efficiency results from the effective density value of 5 g/cm^3.

5. Results

5.1. Sensitivity analysis

The data inversion of the DENSMO currents to the characteristic diameters and the effective density relies on the robustness of the collection efficiency curves of the mobility analyzer and the low pressure impactor. If the geometric standard deviation of the log normal number size distribution is as assumed and the signals of the electrometers have no or negligible noise levels, the correlation between measured currents and the characteristic diameters is unambiguous. In some scenarios, though, this is not the case. For example, the noise of the electrometers can overpower the signal measured from distributions with small total number concentrations. The sensitivity analysis was conducted to study the effects these unwanted deviations have on the data inversion.

The method to resolve characteristic diameters from the measured current fractions described before was used inversely to simulate the current signals from the initial number size distribution with a certain effective density. The effective density of the particles was kept at 2.0 g/cm^3, the GSD of the initial distribution was kept at 1.6, while the CMD was varied from 20 to 300 nm (30 different values). For each CMD value, random noise was added to the simulated current values and 100 noise-affected current sets were generated. The noise level was $\pm$5 fA and $\pm$10% for absolute and relative noise, respectively. These noise levels are expected to cover the overall uncertainty within the current, flow and pressure measurements, as well as the thermal noise and drift of the electrometers. These uncertainty sources were not investigated separately and only a combined effect on the measurements was estimated based on various measurement data acquired from DENSMO.

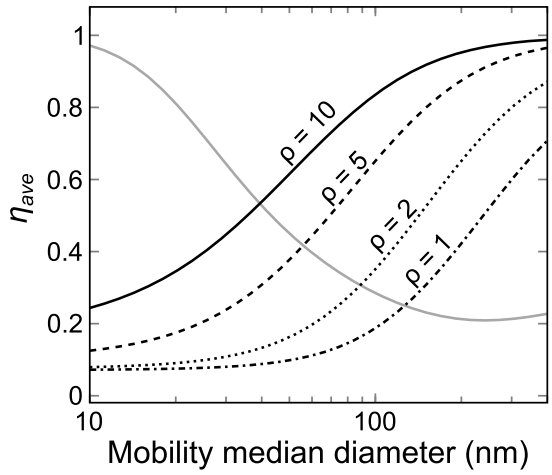

Figure 5: Current ratios of the mobility analyzer (gray line) and the low pressure impactor (black lines) as a function of the mobility median diameter for different effective densities. The figure presents a unique set of solutions for a number size distribution with a GSD of 1.6 and operational parameter values of 50 V and 300 mbar.

The noise-affected simulated current sets were used to calculate the effective density. The effect of wrongly assumed distribution GSD was studied by the same simulated dataset by calculating the density using both the correct initial GMD value of 1.6 and also values of 1.4 and 1.8. Figure 6 shows the results of the sensitivity analysis. The calculated effective density values are plotted, for the three GSD values, as a function of the initial CMD. The solid lines show the mean value of the calculated effective density for the set of 100 noise-affected current values. The darker and lighter gray areas indicate the standard deviation of the calculated density values for the correctly and wrongly assumed GSD values, respectively.

When the assumed GSD was set as 1.4 and 1.8, the calculation deviates from the initial effective density value and even averaging over a longer sample does not improve the result. The uncertainty of the effective density resolved from these simulations is ±7.5% due to aforementioned uncertainty sources and 12% per 0.2 change in assumed GSD. Comparably, with similar simulation Ristimäki et al. (2002) simulated an uncertainty of 4% for the SMPS+ELPI method.

The optimized operation of DENSMO was determined to be achieved when both current ratios

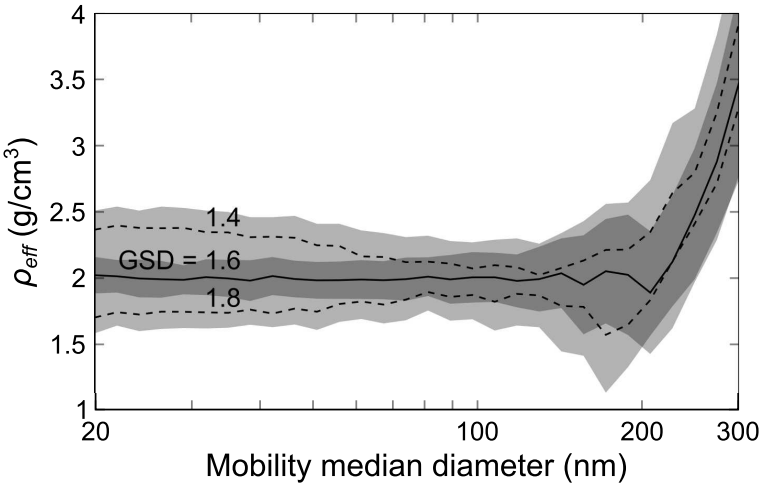

Figure 6: Sensitivity of the measured effective density with different assumed geometric standard deviations (GSD). The simulated GSD was kept at 1.6 and the assumed GSD was varied from 1.4 to 1.8. The effective density was kept at 2.0 g/cm^3, collection voltage at 50 V, pressure at 200 mbar and total number concentration at 10^8 #/cm^3 in all of these simulations. The solid line and the darker gray area denote the mean and standard deviation from the simulation with both assumed and simulated GSD values of 1.6. Additionally, the dashed lines denote the mean of the simulations where the assumed GSD was ± 0.2 from the simulated one and the lighter gray area its combined standard deviation.

and minimum current per electrometer are limited. Current ratios of the mobility analyzer and the low pressure impactor should be in the range of 30 – 90 %. If, however, this is not the case, some adjustments can be done to remedy this by altering the collection voltage (U) and the pressure of the low pressure impactor (P_1). This is of use only if the measured aerosol complies with the other requirements set by DENSMO. The used charger and the mobility analyzer also limit the measurable mobility median diameter range from around 20 nm to 240 nm. The lower limit comes from the charging efficiency of the corona charger used and its inability to charge particle distributions which fall well below 35 nm, which can be seen from Figure 3. The upper limit comes from the fact that the collection efficiency of the mobility analyzer has a minimum at 240 nm, which can be seen in Figure 5. If this upper limit was not set, the current ratio of the mobility analyzer could not be unambiguously resolved to a single mobility equivalent median diameter.

Similar behavior can be observed with other mobility based instruments, like Fast Mobility Particle

Sizer Spectrometer (FMPS; Levin et al., 2015). Exceeding the point of minimum collection efficiency leads to an underestimation of the mobility diameter and an overestimation of the effective density. In some applications, this situation can therefore be detected as unphysically high effective density values, such as those exceeding the bulk material density of the particles. To be on the safe side, low collection efficiency values of the mobility analyzer are to be avoided. The operation was determined to be optimal within collection efficiency values of 30 - 90%.

5.2. Measurements

DENSMO was tested with test aerosols in laboratory conditions with the following materials: dioctyl sebacate (0.92 g/cm^3), sulphuric acid (1.80 g/cm^3), sodium chloride (2.17 g/cm^3), titanium dioxide (rutile, 4.23 g/cm^3) and silver (10.49 g/cm^3) (CRC, 2009). These materials were synthesized in the size range of 23 to 151 nm in the mobility median diameter with mostly spherical morphologies. DOS and H_2SO_4 having their melting temperatures below room temperature were, by default, spherical and assumed to have their effective densities equal to their bulk densities. NaCl is known to exhibit particle bouncing and charge transfer by contact charging in the low pressure impactor based on previous studies (e.g., Kuuluvainen et al., 2013). It was selected as one of the materials to give insight on how particle bounce effects the measured median diameters. Titanium dioxide and silver were measured in their agglomerated state as well as in spherical form in order to see if these two states could be distinguished from each other.

The results from the measurements are shown in Figure 7. The reference effective density values were obtained by a method utilizing SMPS and ELPI distributions, where the effective density functions as a fitting parameter between these distributions (Ristimäki et al., 2002). The measurements of the liquid aerosol particles were found to correlate well with the bulk densities of the materials, just as the agglomerates did with the reference method. Note that the shape factor of the particles is incorporated into the effective density values and should affect both DENSMO and the reference method alike. Measurements from both sintered and agglomerated silver particles and TiO_2 agglomerates yielded results comparable to the reliability of the reference method across the whole range of measured effective densities. The results from the NaCl particles were off as anticipated, most probably due to unwanted particle bounce from the collection plate of the low pressure impactor. This effect also caused the deviation between the measurements of sintered TiO_2 particles and the respective reference measurements, as also reported by Harra et al. (2015). Although the reference method also utilizes low pressure impactor stages, the

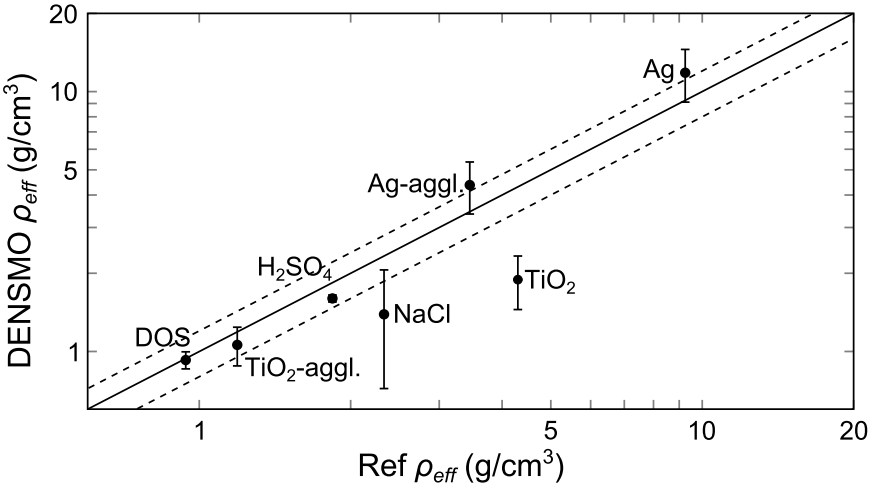

Figure 7: Effective density measurements with SMPS+ELPI density method as a reference. Aerosol particles were synthesized from multiple materials and with a wide range of diameters. The ±20% uncertainty of the reference method has been denoted with the dashed lines on both sides of the unity line (Ristimäki et al., 2002).

bounce probability is lower because of the limited size ranges of the individual impactor stages.

The measurement capabilities of DENSMO were also tested in transient conditions. A transient measurement of silver agglomerate sintering is presented in Figure 8. The silver agglomerates were sintered using a tubular furnace and the measurements made while the temperature increased from 20 ^{o}C to 300 ^{o}C. As the temperature rises, both the aerodynamic and mobility equivalent median diameters deviate from their initial values. The effective density of the silver particles increases from around 4 g/cm^3, where the particles are clearly agglomerated, to around 11.5 g/cm^3, which is within 10% from the bulk density and can be presumed to be fully sintered.

6. Conclusions

We introduced DENSMO, a real-time instrument with a simple construction and the ability to measure effective density as well as aerodynamic and mobility median diameters from unimodal aerosol distributions. A sensitivity analysis was conducted in order to determine the operational ranges of

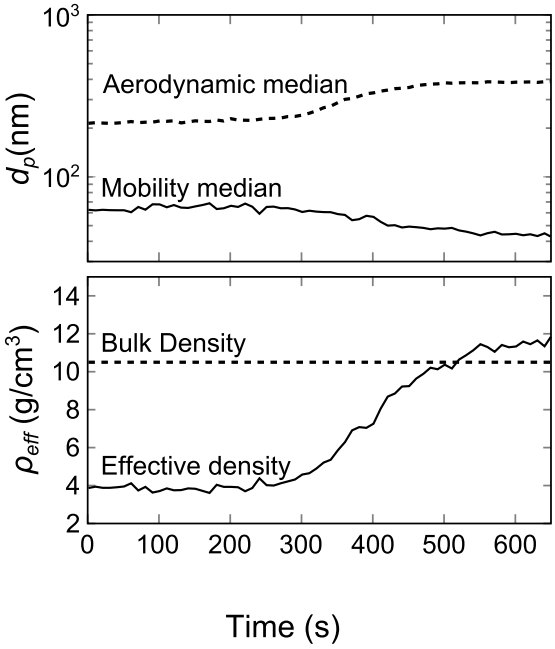

Figure 8: Transient measurement of silver agglomerate sintering with temperature change from 20 ^{o}C to 300 ^{o}C .

the device in terms of total number concentration and characteristic diameters. The effect of wrongly assuming the GSD of the measured distribution was also investigated, as the need for the assumption is inbuilt into the method described, and was determined to be 12% per 0.2 absolute change in the assumed GSD. Overall, the uncertainty of DENSMO was assessed to be $\sim 25\%$. This entails that if the desired value is, for example, coating thickness on spherical 100 nm silica nanoparticles (2.2 g/cm^3), DENSMO can detect, e.g., titania (4.2 g/cm^3), silver (10.5 g/cm^3) and platinum (21.5 g/cm^3) coatings with 18, 3.5 and 1.5 nm resolutions, respectively.

The functionality of DENSMO was investigated with laboratory measurements and it was shown to give good correlation with the chosen reference method. Based on these test measurements, the accuracy of DENSMO is reasonable for quantitative measurements, when the criteria for optimal operation are met. Comparing the results given by DENSMO to the previously available methods, the further

simplifications have not reduced the accuracy significantly and the results were in good agreement.

The most suitable application for DENSMO and similar methods, which are restricted to unimodal aerosol distributions, is to be used in production monitoring, where the stability of the produced material is essential. In these kind of production environments, DENSMO could also be used as a reference while process parameters are being changed, to determine when the desired values are met and the production is again stabilized.

Acknowledgement

This research was funded by the European Union's Seventh Framework Programme (FP7/2007-2013) under the Grant Agreement n^{o}280765 (BUONAPART-E). This publication reflects only the authors' views, and the Community is not liable for any use made of the information contained therein.

References

Aitken, R. J., Chaudhry, M. Q., Boxall, A. B. A., & Hull, M. (2006). Manufacture and use of nanomaterials: current status in the UK and global trends. *Occupational Medicine*, *56*, 300–306. doi:10.1093/occmed/kql051.

Arffman, A., Marjamäki, M., & Keskinen, J. (2011). Simulation of low pressure impactor collection efficiency curves. *Journal of Aerosol Science*, *42*, 329–340. doi:10.1016/j.jaerosci.2011.02.006.

Arffman, A., Yli-Ojanperä, J., Kalliokoski, J., Harra, J., Pirjola, L., Karjalainen, P., Rönkkö, T., & Keskinen, J. (2014). High-resolution low-pressure cascade impactor. *Journal of Aerosol Science*, *78*, 97–109. doi:10.1016/j.jaerosci.2014.08.006.

CRC (2009). *CRC Handbook of Chemistry and Physics, 89th Edition (Internet Version 2009)*. CRC Press/Taylor and Francis, Boca Raton, FL.

DeCarlo, P. F., Slowik, J. G., Worsnop, D. R., Dovidovits, P., & Jimenez, J. L. (2004). Particle morphology and density characterization by combined mobility and aerodynamic diameter measurements. part 1: Theory. *Aerosol Science and Technology*, *38*, 1185–1205. doi:10.1080/027868290903907.

Dzubay, T. G., & Hasan, H. (1990). Fitting multimodal lognormal size distributions to cascade impactor data. *Aerosol Science and Technology*, *13*, 144–150. doi:10.1080/02786829008959432.

Ehara, K., Hagwood, C., & Coakley, K. J. (1996). Novel method to classify aerosol particle according to their mass-to-charge ratio–aerosol particle mass analyser. *Journal of Aerosol Science*, *27*, 217–234. doi:10.1016/0021-8502(95)00562-5.

Fuchs, N. A. (1964). *The Mechanics of Aerosols*. Oxford: Pergamon press.

Harra, J., Juuti, P., Haapanen, J., Sorvali, M., Roumeli, E., Honkanen, M., Vippola, M., Yli-Ojanperä, J., & Mäkelä, J. M. (2015). Coating of silica and titania aerosol nanoparticles by silver vapor condensation. *Aerosol Science and Technology*, *49*, 767–776. doi:10.1080/02786826.2015.1072263.

Hering, S. V., & Stolzenburg, M. R. (1995). On-line determination of particle size and density in the nanometer size range. *Aerosol Science and Technology*, *23*, 155–173.

Hinds, W. (1999). *Aerosol Technology. Properties, Behavior, and Measurement of Airborne Particles.*. John Wiley & Sons, Inc., 2nd Edition, 483p.

Järvinen, A., Aitomaa, M., Rostedt, A., Keskinen, J., & Yli-Ojanperä, J. (2014). Calibration of the new electrical low pressure impactor (elpi+). *Journal of Aerosol Science*, *69*, 150–159. doi:10.1016/j.jaerosci.2013.12.006.

Kelly, W. P., & McMurry, P. H. (1992). Measurement of particle density by inertial classification of differential mobility analyzer-generated monodisperse aerosols. *Aerosol Science and Technology*, *17*, 199–212. doi:10.1080/02786829208959571.

Keskinen, J., Pietarinen, K., & Lehtimäki, M. (1992). Electrical low pressure impactor. *Journal of Aerosol Science*, *23*, 353–360.

Kuuluvainen, H., Arffman, A., Saukko, E., Virtanen, A., & Keskinen, J. (2013). A newmethod for characterizing the bounce and charge transfer properties of nanoparticles. *Journal of Aerosol Science*, *55*, 104–115. doi:10.1016/j.jaerosci.2012.08.007.

Levin, M., Gudmundsson, A., Pagels, J. H., Fierz, M., Mølhave, K., Löndahl, J., & Jensen, I. K., K. A.and Koponen (2015). Limitations in the use of unipolar charging for electrical mobility sizing instruments: A study of the fast mobility particle sizer. *Aerosol Science and Technology*, *49*, 556–565. doi:10.1080/02786826.2015.1052039.

Marjamäki, M., & Keskinen, J. (2004). Effect of impaction plate roughness and porosity on collection efficiency. *Journal of Aerosol Science*, *35*, 301–308. doi:doi:10.1016/j.jaerosci.2003.09.001.

Marjamäki, M., Keskinen, J., Chen, D.-R., & Pui, D. Y. H. (2000). Performance evaluation of the electrical low-pressure impactor. *Journal of Aerosol Science*, *31*, 249–261. doi:10.1016/S0021-8502(99)00052-X.

Marjamäki, M., Ntziachristos, L., Virtanen, A., Ristimäki, J., Keskinen, J., Moisio, M., Palonen, M., & Lappi, M. (2002). *Electrical Filter Stage for the ELPI*. Technical Report SAE Technical Paper 2002-01-0055. doi:10.4271/2002-01-0055.

McMurry, P. H., Wang, X., Park, K., & Ehara, K. (2002). The relationship between mass and mobility for atmospheric particle: A new technique for measuring particle density. *Aerosol Science and Technology*, *36*, 227–238.

Olfert, J., & Collings, N. (2005). New method for particle mass classification–the coulette centrifugal particle mass analyzer. *Journal of Aerosol Science*, *36*, 1338–1352. doi:doi:10.1016/j.jaerosci.2005.03.006.

Rao, A. K., & Whitby, K. T. (1978a). Non-ideal collection characteristics of inertial impactors–I. *Journal of Aerosol Science*, *9*, 77–86. doi:10.1016/0021-8502(78)90069-1.

Rao, A. K., & Whitby, K. T. (1978b). Non-ideal collection characteristics of inertial impactors–II. *Journal of Aerosol Science*, *9*, 87–100. doi:10.1016/0021-8502(78)90070-8.

Ristimäki, J., Virtanen, M., A. Marjamäki, Rostedt, A., & Keskinen, J. (2002). On-line measurement of size distribution and effective density of submicron aerosol particles. *Journal of Aerosol Science*, *33*, 15411557. doi:10.1016/S0021-8502(02)00106-4.

Rostedt, A., Marjamäki, M., & Keskinen, J. (2009). Modification of the ELPI to measure mean particle effective density in real-time. *Journal of Aerosol Science*, *40*, 823–831. doi:10.1016/j.jaerosci.2009.05.002.

Wang, J., Shin, W. G., Mertler, M., Sachweh, B., Fissan, H., & Pui, D. Y. H. (2010). Measurement of nanoparticle agglomerates by combined measurement of electrical mobility and unipolar charging properties. *Aerosol Science and Technology*, *44*, 97–108. doi:10.1080/02786820903401427.

Wang, S. C., & Flagan, R. C. (1990). Scanning electrical mobility spectrometer. *Journal of Aerosol Science*, *13*, 230–240. doi:10.1080/02786829008959441.

Weis, F., Seipenbusch, M., & Kasper, G. (2015). Coating thickness measurements on gas-borne nanoparticles by combined mobility and aerodynamic spectrometry. *Journal of Nanoparticle Research*, *17*. doi:10.1007/s11051-014-2824-1.

Yli-Ojanperä, J., Mäkelä, J. M., Marjamäki, A., M. Rostedt, & Keskinen, J. (2010). Towards traceable particle number concentration standard: Single charged aerosol reference (SCAR). *Journal of Aerosol Science*, *40*, 719–728. doi:10.1016/j.jaerosci.2010.04.012.

Zelenyuk, A., Cai, J., Chieffo, L., & Imre, D. (2005). High precision density measurements of single particles: The density of metastable phases. *Aerosol Science and Technology*, *39*, 972–986.

Zelenyuk, A., & Imre, D. (2005). Single particle laser ablation time-of-flight mass spectrometer: An introduction to splat. *Aerosol Science and Technology*, *39*, 554–568. doi:10.1080/027868291009242.

Zelenyuk, A., Yang, J., Choi, E., & Imre, D. (2009). Splat ii: An aircraft compatible, ultra-sensitive, high precision instrument for in-situ characterization of the size and composition of fine and ultrafine particles. *Aerosol Science and Technology*, *43*, 411–424.

Paper
II

Aerosol analysis of residual and nanoparticle fraction from spray pyrolysis of poorly volatile precursors

Harra, J., Kujanpää, S., Haapanen,. J., Juuti, P., Hyvärinen, L., Honkanen, M. & Mäkelä, J.M.

AIChE Journal, 2016, 63:3, 881 – 892
DOI: 10.1002/aic.15449

II

Aerosol Analysis of Residual and Nanoparticle Fractions from Spray Pyrolysis of Poorly Volatile Precursors

Juha Harra, Sonja Kujanpää, Janne Haapanen, Paxton Juuti, and Jyrki M. Mäkelä
Dept. of Physics, Tampere University of Technology, P.O. Box 692, 33101 Tampere, Finland

Leo Hyvärinen and Mari Honkanen
Dept. of Materials Science, Tampere University of Technology, P.O. Box 589, 33101 Tampere, Finland

DOI 10.1002/aic.15449
Published online August 29, 2016 in Wiley Online Library (wileyonlinelibrary.com)

The quality of aerosol-produced nanopowders can be impaired by micron-sized particles formed due to non-uniform process conditions. Methods to evaluate the quality reliably and fast, preferably on-line, are important at industrial scales. Here, aerosol analysis methods are used to determine the fractions of nanoparticles and micron-sized residuals from poorly volatile precursors. This is accomplished using aerosol instruments to measure the number and mass size distributions of Liquid Flame Spray-generated alumina and silver particles produced from metal nitrates dissolved in ethanol and 2-ethylhexanoic acid (EHA). The addition of EHA had no effect on silver, whereas, 5% EHA concentration was enough to shift the alumina mass from the residuals to nanoparticles. The size-resolved aerosol analysis proved to be an effective method for determining the product quality. Moreover, the used on-line techniques alone can be used to evaluate the process output when producing nanopowders, reducing the need for tedious off-line analyses. © 2016 American Institute of Chemical Engineers *AIChE J*, 63: 881–892, 2017
Keywords: aerosol flame synthesis, particle-size distribution, gas-to-particle, droplet-to-particle, effective density

Introduction

Aerosol produced nanoparticles and powders have been utilized in various different applications, including catalysts, sensors, and electronics,[1–3] which demand high quality homogeneous products. However, the non-uniform process conditions found in different aerosol synthesis methods, for example, laser ablation,[4] electrical discharges,[5] and flames[6] can lead to the formation of large, in some cases, micron-sized particle contaminants. This can be observed as a bimodal particle size distribution, decrease in the surface-to-volume ratio, as well as, varying crystal structures within the produced powder,[6–8] thus, hindering the industrial realization of such production methods.

For an industrial perspective, aerosol flame synthesis techniques are attractive for nanoparticle production due to the inexpensiveness, purity and scalability of the processes, as well as, a multitude of available precursors.[2,9,10] In such techniques, the precursor material can be dissolved in a liquid solvent and sprayed into a high-temperature flame.[11] Ideally, the solvent and the precursor in the sprayed liquid droplets vaporize entirely in the flame. This is followed by the thermal decomposition and nucleation of the gaseous components to form solid nanoparticles through the gas-to-particle aerosol route.[3,12] However, incomplete droplet vaporization can lead to the formation of micron-sized residual particles by the direct decomposition of the precursor material within the droplet via the droplet-to-particle route. The latter particle formation route is utilized in the classic spray pyrolysis technique for the production of ceramic powders.[13] However, if the goal is to produce homogeneous nanosized material, due to the formation of the residual particles, precursor material is wasted, and the quality of the nanopowder product is impaired. Thus, it is highly important to develop simple methods to reliably and fast characterize the quality of the produced nanopowders, preferably on-line during the production process.

The formation of the unwanted residual particles have been observed during the aerosol flame synthesis of different metal, metal oxide, and composite nanoparticles, such as, alumina,[8,14,15] bismuth oxide,[16,17] ceria,[18] cobalt oxide,[8] iron oxide,[8,15] magnesium oxide,[8] titania,[7,19] lanthanum cobalt oxide,[20] silver–palladium,[21] silver–silica,[22] platinum–titania,[23] and yttria-stabilized zirconia.[24] Especially, metal nitrate precursors have been found to produce residual particles due to their poor volatility and relatively low decomposition temperatures,[25] and thus, metal organic precursors are often preferred. However, as the precursor and solvents account a majority, up to approximately 80%, of the production costs,[26] metal nitrates are considered economically more attractive for industrial scale applications.

In a few recent studies, 2-ethylhexanoic acid (EHA) has been added to the metal nitrate precursor solution, resulting in the generation of homogenous nanoparticles.[8,15,24,27] In an extensive research, Strobel and Pratsinis[8] studied the effect of the solvent composition on the metal oxide particles produced from different nitrate precursors with the flame spray pyrolysis (FSP) technique, which employs a methane–oxygen flame.

Correspondence concerning this article should be addressed to J. Harra at juha.harra@tut.fi.

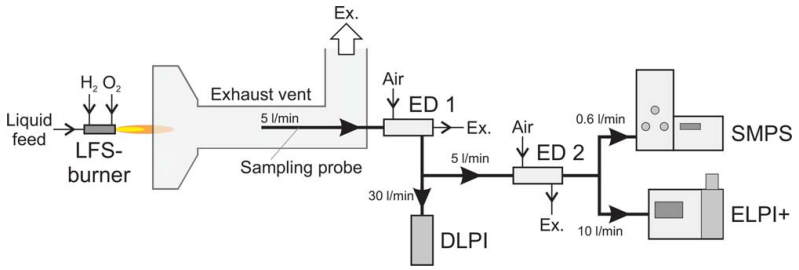

Figure 1. A schematic illustration of the experimental setup.

The particles were produced with the Liquid Flame Spray (LFS) and the aerosol measurements were conducted using a Dekati low pressure impactor (DLPI), a scanning mobility particle sizer (SMPS) and an electrical low pressure impactor (ELPI+). ED stands for an ejector diluter. [Color figure can be viewed in the online issue, which is available at wileyonlinelibrary.com.]

They found that the addition of EHA to an ethanol-based (EtOH) solvent (EtOH/EHA 1:1 and EtOH/diethyleneglycol monobutyl ether (DEGBE)/xylene/EHA 1:1:1:1) reduced the amount of the residual particles due to the formation of volatile carboxylate in the solution or in the sprayed droplets. This lead to a substantial increase in the specific surface area of the produced powders. More recently, Rosebrock et al.[15,28] ignited and imaged single droplets and showed that the addition of EHA (EtOH/xylene/DEGBE/EHA 1:1:1:1) to the solvent resulted in microexplosions that lead to the nanoparticle formation. Furthermore, by comparing electron microscope images of the produced particulate matter, they concluded that their findings are also applicable to the large scale production of particles by the FSP. In previous publications, the residual particles have been analyzed, for example, by electron microscopy, nitrogen absorption, X-ray diffraction, and X-ray disc centrifugation. In these off-line methods, the aerosol particles are typically collected into a powder, and possibly redispersed into a liquid, thus, potentially losing information on the individual particles dispersed in the gas-phase during the production. Moreover, some of these methods are only qualitative or require crystalline particles.

Some conclusions on the presence of the residual particles have been made by measuring the number size distribution of the particles using aerosol instruments. An extensive study on the effect of different process parameters on the aerosol flame synthesized titania nanoparticles was conducted by Aromaa et al.[7] They measured the number size distributions of the produced nanoparticles with on-line aerosol instruments and suggested that in the absence of residual particles, larger agglomerates were formed, as there is more material undergoing the gas-to-particle conversion. However, as the nanoparticles formed via the gas-to-particle route practically always dominate the number size distribution of the flame-generated aerosol particles, it is difficult to obtain quantitative information on the amount of the residual particles using only on-line measurement instruments, which are usually sensitive to the particle number concentration. Conversely, due to their large size compared to the nanoparticles, the residual particles can have a considerable contribution on the total mass of the synthesized particles. Thus, a direct measurement of the mass size distribution could be a viable method to investigate the residual particles quantitatively, and can be accomplished with a gravimetric analysis of particles collected with a cascade impactor.[29] Moreover, a combination of the as mentioned gravimetric analysis and on-line aerosol measurements has a potential to provide quantitative information on the quality of the nanopowders, as well as, the fundamental process conditions.

In this study, we take advantage of aerosol analysis methods to determine the quality of nanopowders by measuring the fractions of residual and nanoparticles produced with a hydrogen–oxygen flame from poorly volatile nitrate precursors. This is accomplished by complementary aerosol measurement instruments used to determine the number and mass size

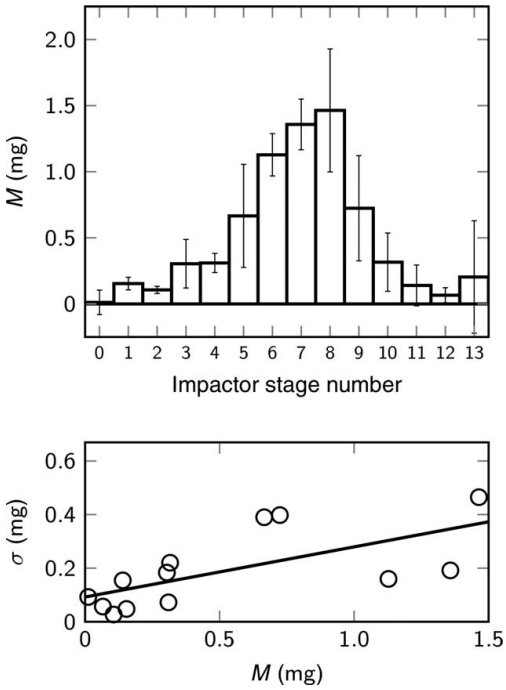

Figure 2. The average particle mass on each impactor stage (top panel) for five alumina particle collections and the standard deviation of the mass as a function of the mass (bottom panel).

In the top panel, the stage number 0 corresponds to a reference measurement where no particles were collected and the error bars correspond to the standard deviation of 5 measurements (12 for the reference). The expression of the linear fit in the bottom panel is $y = 0.187x + 0.092$.

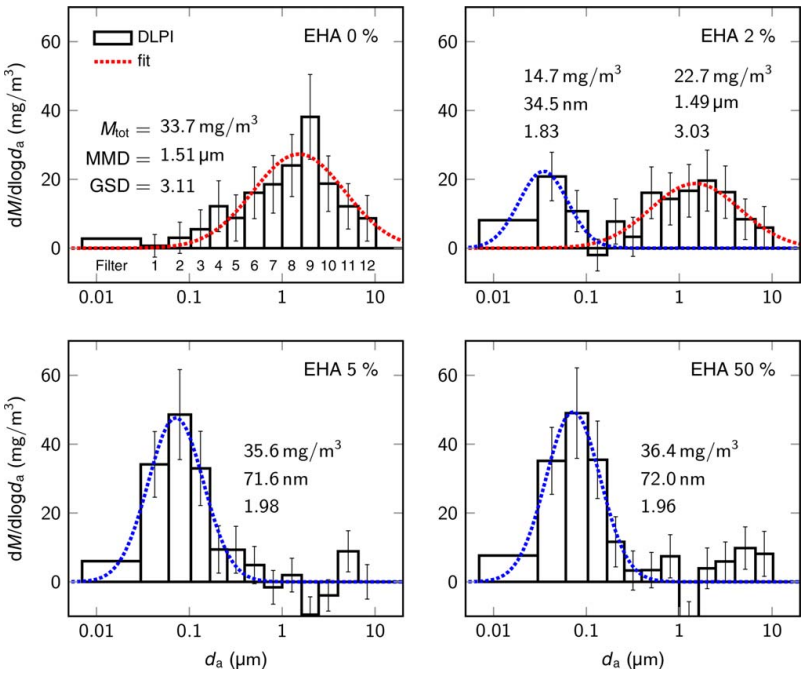

Figure 3. The mass size distributions of alumina particles produced with different EHA volume concentrations (0, 2, 5, and 50%).

The particles were collected with the DLPI and the mass was determined by a gravimetric analysis. The numbering of the impactor stages (and the filter) is shown in the top left panel. The parameters, the total mass concentration (M_{tot}), mass median diameter (MMD) and geometric standard deviation (GSD), of the log-normal fits for the nanoparticles (blue dotted line) and the residual particles (red dotted line) are presented next to the distributions. [Color figure can be viewed in the online issue, which is available at wileyonlinelibrary.com.]

distributions of the particles in the aerosol phase. The particle materials chosen for this study, alumina (Al_2O_3) and silver (Ag), differ considerably in terms of, for example, bulk density (3.99 g/cm^3 and 10.5 g/cm^3, respectively) and boiling point (3250 K and 2435 K, respectively).[30] Thus, we are able to establish a relatively broad perspective on the application of aerosol measurement instruments on the determination of the particle number and mass size distributions of the flame-generated aerosol residual and nanoparticles. Previous studies have suggested that silver nitrate precursor potentially produces residual particles.[21,22] In regards of aluminum nitrate, even though it has been qualitatively shown that the addition of EHA reduces the amount of the residual particles,[8,15] the required minimum amount of EHA in the solution is still unknown. Furthermore, by reducing the amount of the EHA in the solution, it would be possible to lower the nanoparticle production costs, especially, in industrial scale facilities.[26] In this study, we find that with the aluminum nitrate, the addition of EHA shifts the particle mass practically entirely from the residual mode to the nanoparticle mode already at an EHA volume concentration of 5%, whereas, with silver nitrate, no residual particles were observed, and the addition of EHA had no effect on the number and mass size distribution of silver nanoparticles. Moreover, this study demonstrates that with a well-planned experimental system, the on-line measurements alone can give valuable information on the process details of aerosol synthesis, such as, the presence of residual particles, thus, reducing the need for tedious off-line analyses for the quality control of nanopowders.

Materials and Methods

The particles were generated with the Liquid Flame Spray (LFS) technique[31] that employs a hydrogen–oxygen flame, used recently, for instance, for producing functional nanoparticle coatings,[32,33] nanopowders,[34,35] and test aerosols.[36,37] A detailed description of the LFS technique can be found from previous publications, including the dimensions of the used burner (the LR burner),[7] gas velocities,[38] and flame temperatures.[19,31] The maximum temperature in the employed hydrogen–oxygen flame is approximately 3000 K, and according to Mäkelä et al.,[39] the addition of EtOH solvent to the flame has a slight increasing effect on the temperature. In this study, aluminum nitrate nonahydrate ($Al(NO_3)_3{\cdot}9H_2O$, Merck, 98.5%) and silver nitrate ($AgNO_3$, Strem Chemicals, 99.9%) dissolved in a liquid solvent, 80 and 17 mg/mL (0.2 and 0.1 M), were used as precursors for alumina and silver particles, respectively. The solvent composed of EtOH (Altia, 99.5%) and EHA (Acros Organics, 99%) at different volume concentrations from pure EtOH to EtOH/EHA 1:1 (i.e., EHA 0–50%). The liquid feed rate in the LFS-burner was set to 8 mL/min, resulting in a calculated production rate of approximately 5 g/h for both particle materials. The gas flow rates in the burner for hydrogen and oxygen were 40 L/min and 20 L/min, respectively.

A schematic presentation of the experimental setup is shown in Figure 1. The LFS-burner was placed horizontally at the opening of an exhaust vent with an inner diameter of 16 cm. The LFS-produced aerosol was quickly diluted by the ambient air drawn into the exhaust vent. The air velocity in

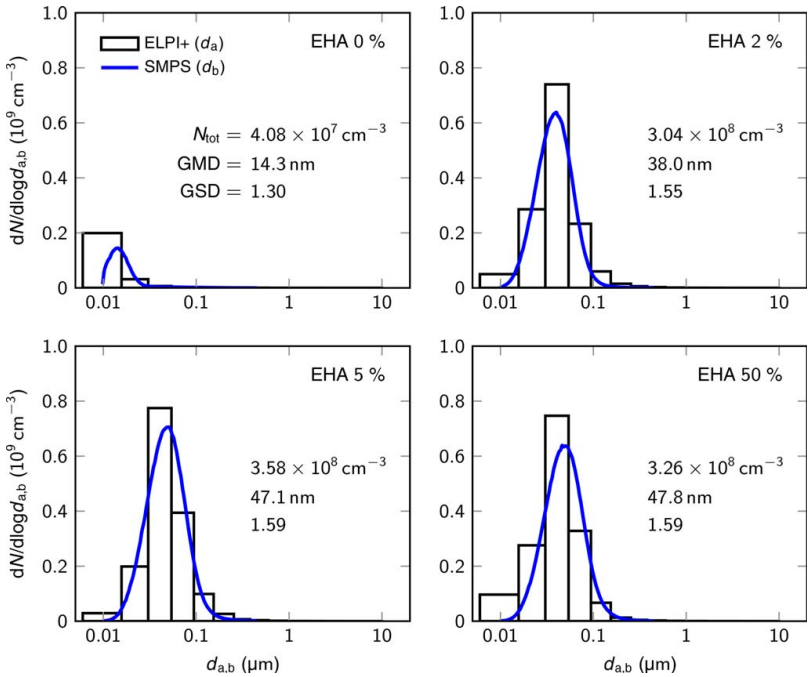

Figure 4. The number size distributions of alumina nanoparticles produced with different EHA volume concentrations (0, 2, 5, and 50%).

Note that the ELPI+ measures the aerodynamic diameter and the SMPS measures the mobility diameter. The total number concentration (N_{tot}), geometric mean diameter (GMD), and geometric standard deviation (GSD) of the distribution measured by the SMPS are presented. [Color figure can be viewed in the online issue, which is available at wileyonlinelibrary.com.]

the exhaust vent, approximately 1.6 m/s, was measured with a pitot tube, corresponding to a flow rate of approximately 2000 L/min, and thus, a dilution ratio of approximately 30. At a distance of 60 cm from the burner, an aerosol sample was drawn into a steel probe, with an inner diameter of 8 mm and a gas flow rate of 5 L/min. To ensure a representative aerosol sample, the sampling was performed isokinetically, meaning that the probe was aligned parallel to the gas streamlines and the gas velocity in the probe equaled the free-stream velocity.[40] Based on a previous study,[19] we estimate that at the sampling point, the temperature was approximately 200°C. As the LFS produces water vapor as a by-product due to the hydrogen–oxygen flame, the possible condensation of the water during the sampling must be discussed. This feature of the LFS has been previously utilized in the collection of the produced particles directly into a liquid suspension.[41] However, in this study, due to the fast dilution with the ambient air and the relatively high sampling temperature, no water condensation occurs during the sampling.

After the sampling, the aerosol was diluted with particle-free air using a Dekati ejector diluter (ED 1 in Figure 1) with a dilution ratio of approximately 8. A Dekati low pressure impactor (DLPI), placed directly below the diluter to minimize the losses of large particles due to the gravitational force, was used to determine the mass size distributions of the produced particles. The DLPI is a cascade impactor, with a nominal flow rate of 30 L/min, and a design based on the electrical low pressure impactor (ELPI).[42] Moreover, it classifies the aerosol particles according to their aerodynamic diameter on 13 impactor stages with cutpoints of 30 nm–10 μm followed by a back-up filter, which collects the remaining nanoparticles. The particles were collected on aluminum foils, greased with Apiezon vacuum grease dissolved in toluene, to prevent possible particle rebound from the substrates.[43] The greased aluminum substrates were weighed before and after the particle collection with an analytical balance (Mettler Toledo AE163, readability 0.01 mg). Before the first weighing, the greased substrates were heated in an oven at a temperature of 100°C for 60 min, to vaporize possible volatile compounds. The mass of an individual greased aluminum foil substrate was approximately 19 mg, while the maximum collected particle mass on an individual substrate was approximately 1 mg. Moreover, the particle collection time with the DLPI was set to 30 min, corresponding to an estimated total collected particle mass of approximately 4 mg. It should be noted that as the collection of a sufficient particle mass and the subsequent weighing of the substrates takes a relatively long time, here overall in the order of an hour, the DLPI must be considered as an off-line measurement technique, and thus, it might not be suitable in process control applications which require real-time measurement data.

Besides gravimetric measurements, the particles that were size classified and collected on the DLPI impactor stages were also analyzed with a scanning electron microscope (SEM, Zeiss ULTRAplus) and an X-ray diffractometer (XRD, PANalytical Empyrean). As the collected particle mass on the individual substrates was low, the XRD pattern was recorded from the as-collected particles on top of the aluminum foils. For the

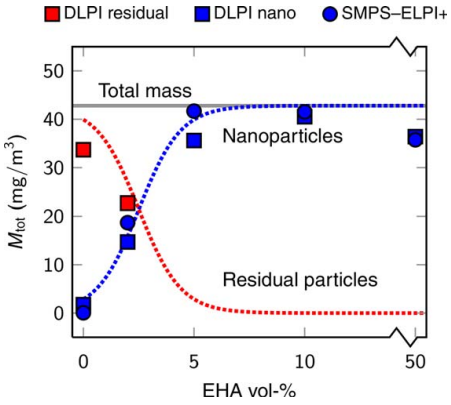

Figure 5. The total mass concentration of the residual particles (red markers) and the nanoparticles (blue markers) determined from the DLPI (square markers) and the SMPS–ELPI+ (round markers) measurements as a function of the EHA volume concentration.

The solid gray line represents the total mass concentration calculated from the precursor concentration, liquid feed rate, and gas flow rate in the exhaust vent. Note the discontinuity on the horizontal axis. The red and blue dotted lines, for residual and nanoparticles, respectively, are guides for an eye, with the red line obtained by subtracting the blue line from the gray line. [Color figure can be viewed in the online issue, which is available at wileyonlinelibrary.com.]

SEM, a particle sample was scraped off from the foil, dispersed in EtOH, and deposited onto a carbon film on a copper grid. Furthermore, for a reference, powder samples were collected directly from the aerosol on holey carbon films on copper grids and imaged with the SEM and a transmission electron microscope (TEM, Jeol JEM-2010).

Two on-line aerosol measurement instruments, a scanning mobility particle sizer (SMPS),[44] composed of a radioactive charger (Krypton-85), a differential mobility analyzer (TSI 3081), and a condensation particle counter (TSI 3025), as well as, an electrical low pressure impactor (ELPI+),[45] were used to determine the number size distributions of the produced particles. For these instruments, the aerosol was diluted again with another ejector diluter (ED 2 in Figure 1, dilution ratio ~8). The nominal particle size ranges for the used SMPS and ELPI+ were 10–450 nm and 6 nm–10 μm, respectively. However, a tubing with a length of approximately 8 m, including a vertical climb, separated the on-line instruments from the sampling probe, thus, resulting to substantial losses for the micron-sized particles due to the gravitational settling. Conversely, the diffusion dominates the losses of the nanosized particles in the tubing, which were estimated to be approximately 17 and 1% for 10 and 100 nm particles, respectively.[3] Therefore, we expect to measure only the number size distribution of the nanoparticle mode.

It should be noted that the two on-line aerosol instruments measure different equivalent particle diameters, that is, the SMPS classifies the particles according to their mobility diameter (d_b), while the ELPI+ measures the aerodynamic diameter (d_a). Detailed information on the different equivalent diameters can be found from the literature.[3] Essential to our work, for a spherical particle, the mobility diameter equals the geometric diameter, whereas, the aerodynamic diameter depends on the density of the particle. Furthermore, the information on these two particle diameters can be combined to obtain the effective density (ρ_{eff}) of the particles according to the following equation[3,46]

$$\rho_{eff} = \rho_0 \frac{C_c(d_a) d_a^2}{C_c(d_b) d_b^2}, \quad (1)$$

where ρ_0 is the unit density (1 g/cm^3) and $C_c(d_{a,b})$ is the slip correction factor[40] of the corresponding equivalent diameter. Both the material density and the particle shape affect the effective density. For spherical non-hollow particles, the effective density corresponds to the bulk density of the particle material, whereas, lower effective density is an indication of non-spherical, typically agglomerated, aerosol particles.

Results and Discussion

Uncertainties in the mass size distribution

Before performing the measurements described in the previous section, five mass size distributions of identically produced alumina particles were determined gravimetrically using the DLPI. It should be noted that these tests were performed with a similar experimental setup but with a different LFS-burner. In addition, the alumina particles were produced from a different precursor and solvent than described earlier. Also, no back-up filter was used in the DLPI and the particle collection time was 45 min. Due to all these differences, these tests are only meant to estimate the uncertainty of our method in the determination of the mass size distribution. Furthermore, the tests take into account only the combined effect of the individual sources for the uncertainties arising from the particle production, experimental system, and gravimetric analysis.

The average total collected mass of the alumina particles in the five measurements was 6.9 ± 1.1 mg. Furthermore, the average mass collected on each impactor stage of the DLPI is shown in the top panel of Figure 2. In the figure, the impactor stage number 0 corresponds to a reference measurement were there were no gas flow going into the DLPI, and thus no particles were collected. The error bars correspond to the standard deviation of the five measurements, and 12 measurements in the case of the reference. The average mass of the reference measurement was close to zero, as it should be. The stages containing more mass have larger standard deviation. However, relatively large standard deviations can be seen on stages 5 and 9, where the gradient of the mass size distribution is the largest. This is understandable, as minor changes in the pressures and flow rates can slightly shift the particle size distribution or the cutpoints of the cascade impactor. Stage 13 is used only as a precut impactor, and thus it is vulnerable to possible contamination.

The bottom panel of Figure 2 shows the standard deviation of the collected particle mass on an individual stage as a function of the mass. According to a linear fit to the data points, we can estimate that the absolute uncertainty of the used method in this study is approximately 0.09 mg, while the relative uncertainty is approximately 20%. These values have been used to calculate the error bars shown in the mass size distributions of alumina and silver particles presented in Figures 3 and 9, respectively.

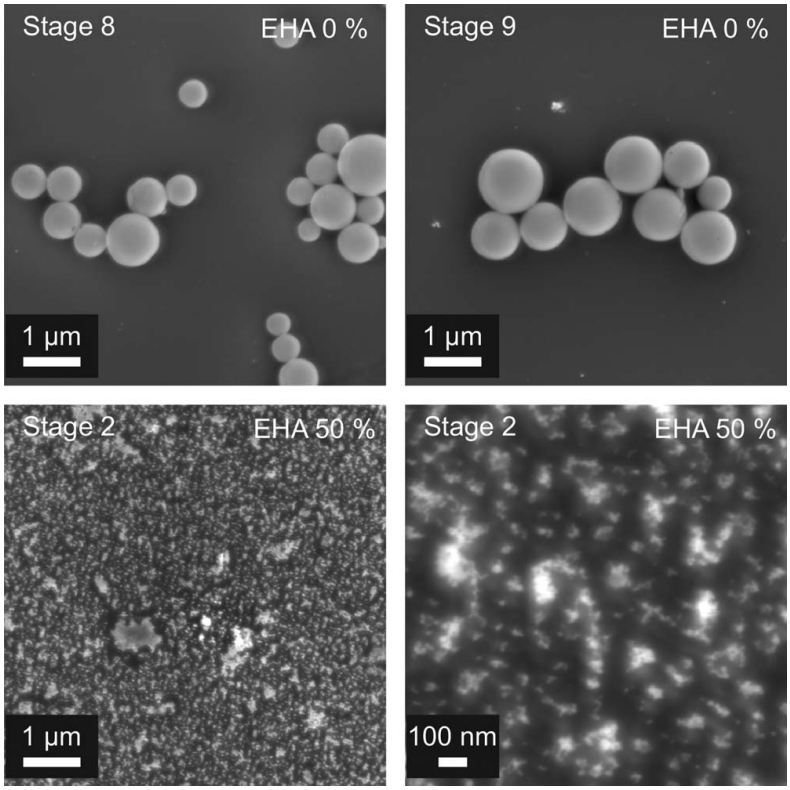

Figure 6. SEM images of alumina residual particles (top panels) and nanoparticles (bottom panels) at different magnifications.

The residual particles were produced without EHA and collected on the DLPI impactor stage number 8 and 9, with aerodynamic cutpoint diameters of 1.0 µm and 1.62 µm, respectively. The apparent agglomeration of the residual particles is an artifact caused by the sample preparation for the SEM. The nanoparticles were produced with a 50% EHA volume concentration and collected on the stage number 2, with an aerodynamic cutpoint diameter of 60 nm.

Alumina particles

Alumina particles were produced using five different EHA volume concentrations (0, 2, 5, 10, and 50%). Figure 3 presents the mass size distributions of the alumina particles produced with four different EHA concentrations. The shown DLPI measurements were corrected with the dilution ratio, and log-normal functions were fitted to the obtained results, with the total mass concentration (M_{tot}), mass median diameter (MMD), and geometric standard deviation (GSD) as the fitting parameters. The effect of the addition of EHA is evident from the results. Without EHA, only the residual particles contribute to the measured mass, with the MMD at 1.5 μm. With an EHA concentration of 2%, a bimodal mass size distribution was obtained. Both the MMD and GSD of the residual particle mode remain constant. However, the total mass of the residual particles decreases, as a part of the material undergoes the gas-to-particle route, and a nanoparticle mode with an MMD of 35 nm emerges. As the EHA content is increased to 5% and over, the MMD of the nanoparticles increases to 72 nm due to the increased agglomeration, as more material undergoes the gas-to-particle route.

At EHA concentrations of 5% and above, only the nanoparticle mode can be resolved. The error bars in the mass size distributions are calculated based on the estimated uncertainty of the used gravimetric method (absolute 0.09 mg, relative 20%), as discussed earlier. In the bottom panels of Figure 3, we can see that the measured mass for the larger particles (>1 μm), in general, remains below the detection limit, and no clear size distribution for residual particles emerges. In addition, due to the experimental uncertainties, the measured mass of some of the substrates has even decreased between the two weighings. Thus, with this method alone, we are unable to completely rule out the existence of possible residual particles.

The mass size distribution results are consistent with the findings of Rosebrock et al.[15] on the microexplosions of the droplets. That is, a single droplet either explodes, followed by the gas-to-particle process, or a particle is formed within the droplet via the droplet-to-particle route. In specifically, the constant MMD of the residual mode at low EHA concentrations (0 and 2%) suggests that a partial evaporation of the precursor material from the droplet is not an option. Moreover, it is likely that at low EHA concentrations, only droplets passing the hottest part of the flame will explode. Homogeneous alumina nanoparticles have been successfully synthesized from aluminum nitrate precursor in previous studies using the FSP technique,[8,15] which has a slightly lower maximum flame temperate than the LFS, approximately 2600 K, according to

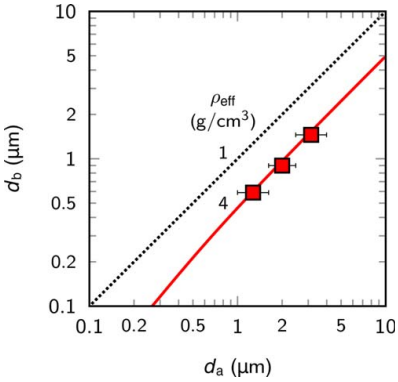

Figure 7. The mobility diameter (d_b) of the alumina residual particles collected on the DLPI stage number 8, 9, and 10 as a function of the aerodynamic diameter (d_a).

The aerodynamic diameter is the geometric mean of two adjacent stage cutpoints, represented by the error bars. As the particles were spherical, the mobility diameter equals the geometric diameter, and thus, was determined from the SEM images. The lines corresponding to constant effective densities were calculated using Eq. 1. [Color figure can be viewed in the online issue, which is available at wileyonlinelibrary.com.]

Mädler et al.[47] Furthermore, the volume concentration of the EHA in an otherwise pure EtOH-based solution containing 0.5 M of aluminum nitrate has previously been 50%.[8] Here, we have quantitatively shown that with the hydrogen–oxygen flame of the LFS, a volume concentration of as low as 5% is enough to shift practically the entire mass of 0.2 M precursor solution from the residual particles to the nanoparticles. This is an important result, especially, concerning the industrial scale aerosol flame synthesis of nanoparticles, where the precursor and solvents account a majority of the production costs.[26]

The dilution corrected number size distributions of alumina particles produced with four different EHA concentrations are shown in Figure 4. In general, the SMPS and ELPI+ measurements were very consistent with each other. However, we can see that the aerodynamic diameter of the particles, measured by the ELPI+, was slightly smaller than the mobility diameter, measured by the SMPS, meaning that the effective density of the particles was under the unit density. For the particles in the nanoparticle mode, mean effective densities of 0.7–0.9 g/cm^3, approximately 20% of the bulk density of alumina, were acquired with the computational SMPS–ELPI fitting method introduced by Ristimäki et al.[48] This suggests that the alumina nanoparticles were highly agglomerated. It should be noted that a more detailed analysis using the same computational method could allow to determine the effective density as a function of the particle size.[49]

The total number concentration (N_{tot}), geometric mean diameter (GMD) and GSD of the SMPS measurements are presented along with the number size distributions in Figure 4. Without EHA, the concentration and diameter (14 nm) of the particles was relatively small. With the addition of only 2% EHA, the concentration increased approximately an order of magnitude and the particle size increased to 38 nm. After the EHA concentration exceeded 5%, the number size distribution remained approximately constant with the GMD at 47 nm.

The total mass concentration of the nanoparticles and the residual particles as a function of the EHA volume concentration is presented in Figure 5. Besides the DLPI measurements, the mass concentrations of the nanoparticle mode was also determined from the number size distributions measured by the SMPS using the mobility diameter to calculate the particle volume and the effective density, calculated from the SMPS–ELPI+ fitting, to obtain the particle mass. The results show relatively good comparability between the SMPS–ELPI+ method and the DLPI measurements. Furthermore, the total mass concentration of the produced alumina particles, calculated using the precursor concentration, the liquid feed rate and the gas flow rate in the exhaust vent, was estimated to be 43 mg/m^3. The measured particle mass concentration values are close to this, suggesting that the material losses in the experimental system were not significant for alumina particles. Furthermore, we see that the on-line measurements of the number size distributions alone can give indirect information on the existence of the residual particles, as also suggested in an earlier study.[7] Thus, in some cases, tedious off-line measurements, such as gravimetric analysis or microscopy, are unnecessary.

SEM micrographs of the alumina nanoparticles and residual particles collected with the DLPI are presented in Figure 6. The residual particles in the figure (top panels) were collected on the DLPI stage number 8 and 9, with aerodynamic cutpoint diameters of 1.0 μm and 1.62 μm, respectively (see the numbering of the stages in the top left panel of Figure 2). The micrographs show that the particles were spherical, as expected from the droplet-to-particle transformation, as well as, from the results in the recent literature.[8,15] The apparent agglomeration of the residual particles is most likely an artifact caused by the sample preparation for the SEM. This is supported by the fact that the micrographs show both individual particles, as well as, "agglomerates." If the agglomeration had occurred in the aerosol phase, the two types of particles would have very different aerodynamic diameters, and would not be found from the same impactor stage.

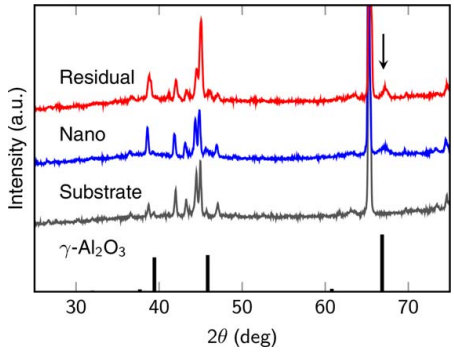

Figure 8. The X-ray diffraction pattern of alumina residual particles (EHA 0%, stage 9) and nanoparticles (EHA 50%, stage 2) on the collection substrate.

The pattern of a plain substrate and the γ-alumina reference[52] are shown alongside. Both particle modes show a peak, indicated with an arrow, that corresponds to the (440) lattice plain of γ-alumina. [Color figure can be viewed in the online issue, which is available at wileyonlinelibrary.com.]

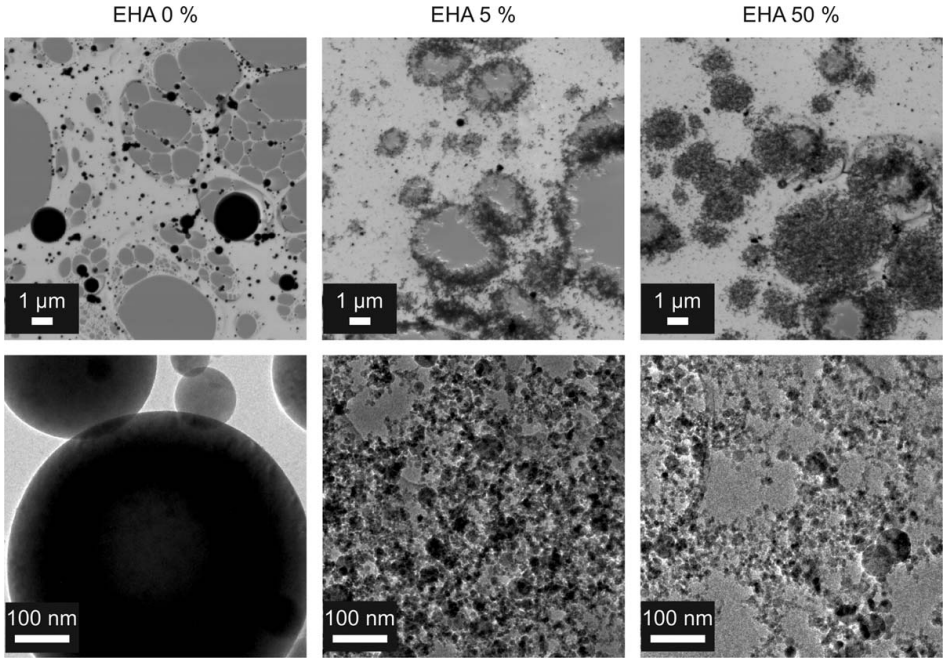

Figure 9. SEM (top panels) and TEM (bottom panels) micrographs of alumina powder samples produced with different EHA volume concentrations (0, 5, and 50%) and collected directly from the aerosol on holey carbon films.

The geometric diameter of the residual particles was calculated from the SEM images and compared to the aerodynamic diameter, latter of which is assumed to be the geometric mean of two adjacent stage cutpoints, to estimate the density of the residual particles. In Figure 7, the aerodynamic diameter of the particles is presented as a function of the geometric diameter, which also equals the mobility diameter, as the particles are spherical. A density of approximately 4 g/cm^3 fits well with the acquired data. This density is close to the bulk density of alumina, supporting the earlier claim that no agglomeration between the residual particles occurs in the aerosol phase. Moreover, the obtained density suggests that the particles are non-hollow, in contrast to some studies where also partially hollow alumina particles were formed via the droplet-to-particle aerosol route.[8,13–15,50]

The nanoparticles in the SEM micrographs (bottom panels of Figure 6) were collected on the DLPI stage number 2, with an aerodynamic cutpoint diameter of 60 nm. The particles are homogenous and appear to be highly agglomerated, as expected from the gas-to-particle transformation and the following particle agglomeration process, as well as, from previous studies with similar synthesis methods and precursors.[8,15] In this study, the agglomeration is also supported by the measured low effective density. However, it should be noted that these micrographs alone are unable to reveal the actual agglomeration state due to the sample preparation method for the SEM.

As the residual particles are spherical, and assuming that the precursor decomposes to alumina without evaporation, as suggested by the results, we can calculate the MMD of the sprayed droplets. For this calculation backwards, information on the density of the residual particles and the concentration of the precursor solution is required. Using the MMD of the residual particles, approximately 0.7 μm (corresponding to the aerodynamic diameter of 1.5 μm), the MMD of the droplets receives a value of approximately 5 μm. The droplet diameter in a flame spray has been studied in previous publications by direct optical measurements.[47,51] However, comparison to earlier studies is not straightforward, as the droplet diameter depends on, for example, the atomizer and burner design, used solvent and liquid, and gas flow rates. A similar LFS-burner that was employed in this study was used previously by Keskinen et al.[38] In their study, the mass size distribution of water droplets generated by a non-burning liquid spray peaked at approximately 10 μm, according to the results obtained from a gravimetric analysis. In the same study, it was concluded that the sprayed droplets were approximately 25% larger for water than for EtOH, giving results that our comparable to our calculations.

The size dependent collection of the synthesized aerosol particles with the DLPI allows also size selective characterization using off-line methods, such as electron microscopy for imaging, as shown earlier, and X-ray diffraction (XRD) for determining the crystal structure of the particles. An XRD pattern of the nanoparticles (stage 2, EHA 50%) and the residual particles (stage 9, EHA 0%), as well as, the plain substrate is shown in Figure 8. The used substrate was clearly not ideal for the XRD measurements due to the material (alumina particles on aluminum substrate) and the relatively large background. However, some conclusions can be made, as the XRD pattern of both particle modes shows a peak at approximately $2\theta = 67°$, which is missing from the XRD pattern of the plain

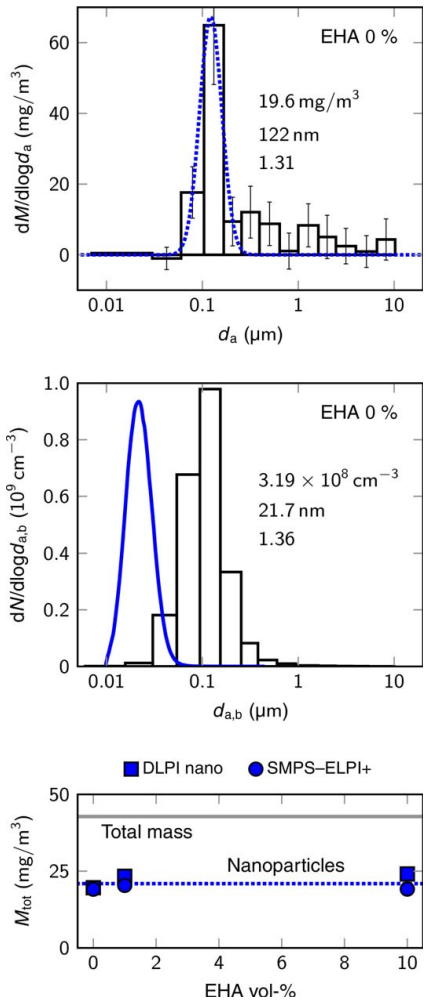

Figure 10. Mass (top panel) and number (middle panel) size distribution of silver particles produced without EHA, along with the total mass concentration of the nanoparticles as a function of the EHA volume concentration (bottom panel).

The mass distribution was measured with the DLPI (bars) and the number distribution with the SMPS (solid line) and the ELPI+ (bars). The parameters, the total mass/number concentration, MMD/GMD and GSD, correspond to the log-normal fit (dotted line) and the SMPS measurement. Note that the DLPI and the ELPI+ measure the aerodynamic diameter (d_a) and the SMPS measures the mobility diameter (d_b). [Color figure can be viewed in the online issue, which is available at wileyonlinelibrary.com.]

substrate. This peak corresponds to the (440) lattice plain of γ-alumina.[52] In a recent study, Nikkanen et al.[53] detected no crystalline alumina in the LFS-generated iron oxide doped alumina–zirconia nanopowder, whereas, the alumina particles produced by Strobel et al.[54] were slightly amorphous γ-phase, as is most likely the case with the alumina residual and nanoparticles produced in this study. However, we cannot rule out the existence of other alumina crystal structures.[55] Based on the previously measured temperature profile of the flame[19] and the gas velocity,[38] we estimate that the cooling rate in the LFS is in the order of 10^5-10^6 K/s. Such rapid cooling favors the formation of amorphous and γ-phase,[56] which is also the most stable nanocrystalline phase of alumina.[57] In case of some particle materials synthesized using aerosol flame synthesis methods, the residual and nanoparticles have had different crystal structures. For example, in previous studies, the crystal structures of flame-generated titania residual and nanoparticles were rutile and anatase,[7] whereas, for cobalt oxide, they were CoO and Co_3O_4,[8] respectively. The results of this study suggest that the LFS-generated alumina residual and nanoparticles have same crystal structures.

As a reference, alumina powder samples were collected directly from the aerosol on holey carbon films and imaged with the electron microscopes. Figure 9 shows SEM (top panels) and TEM (bottom panels) micrographs of the powders produced with EHA concentrations of 0, 5, and 50%. Large spherical residual particles dominate the sample produced without EHA. Furthermore, there is no indication of hollow or agglomerated residual particles in the TEM images, thus, supporting our earlier claims. No observable differences were detected with the powders produced with EHA concentrations of 5 and 50%. Both samples show homogenous nanosized agglomerates with a substantial decrease in the number of the large spherical residual particles. It should be noted that from both of the samples containing EHA, a few individual residual particles, typically smaller in size compared to the situation without EHA, were observed. All in all, the reference powder samples were very consistent with our results and conclusions presented in this study.

Silver particles

Silver particles were produced with three different EHA volume concentrations (0, 1, and 10%). Figure 10 shows the mass and number size distributions of the particles synthesized without EHA. The mass size distribution peaks at an aerodynamic diameter of 122 nm, and contains no indication of a residual particle mode. This is contrary to some previous studies, where bimodal size distributions have been observed when producing composite particles composed of palladium[21] or silica,[22] and silver from silver nitrate. The reason for this discrepancy can be speculated: in the former study, water was used as a solvent, whereas, in the latter study, the flame temperature was likely somewhat lower than in this study. Furthermore, the role of the other materials, palladium and silica, in the formation of the residual particles cannot be ruled out. In the number size distribution (middle panel of Figure 10), we see that the mobility size of the particles (22 nm) is considerably smaller than the aerodynamic size, resulting to an effective density of 7.3 g/cm,[3] which is close to a value determined in a previous study for LFS-generated silver particles.[37] This density is approximately 70% of the bulk density, suggesting that the particle shape deviates only slightly from a sphere.

The addition of EHA to the solution had no observable effect on the mass and number size distribution of silver particles produced from silver nitrate. The bottom panel of Figure 10 shows the total mass concentration of the silver nanoparticles as a function of the EHA volume concentration. The results measured with the DLPI and calculated using the SMPS–ELPI+ method are consistent with each other.

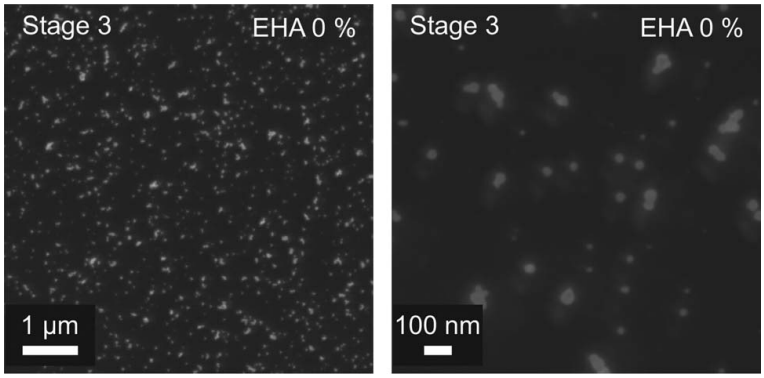

Figure 11. SEM images of silver nanoparticles at different magnifications produced without EHA and collected on the DLPI impactor stage number 3, which has an aerodynamic cutpoint diameter of 108 nm.

However, we see that the measured mass concentration is only approximately half of the concentration estimated from the production rate. This can be contributed to the wall losses in the experimental system caused by silver vapor condensation. Similar losses with alumina were not observed due to its lower vapor pressure. That is, alumina particles are formed earlier in the hot flame, whereas, silver will readily vaporize in the flame, and thus, also produce no residual particles. In evaporation–condensation type aerosol nanoparticle generators the wall losses for silver vapor have also been substantial.[35,58,59] SEM micrographs of silver nanoparticles collected on the stage number 3 of the DLPI, with an aerodynamic cutpoint diameter of 108 nm, are shown in Figure 11. The observed particles were spherical or highly sintered, which is in agreement with the relatively high effective density.

Conclusions

Aerosol analysis methods were explored for the quantitative evaluation of the quality of nanopowders produced from poorly volatile precursors. An aerosol flame synthesis technique, LFS, was used to produce alumina and silver particles from the corresponding metal nitrate precursors dissolved in ethanol and EHA with different volume concentrations. The produced particulate matter consisted of homogenous nanoparticles formed via the gas-to-particle route, as well as, unwanted micron-sized residual particles formed via the droplet-to-particle route. Quantitative information on both of these particle modes were acquired using complementary on-line and off-line aerosol measurement instruments. The mass size distributions of the residual and nanoparticles were obtained by a gravimetric analysis of particles collected with a cascade impactor. Furthermore, the number size distributions of the nanoparticles were measured with two on-line aerosol instruments (SMPS and ELPI+), operating at different physical principles, thus, giving also information on the effective density, in this case the shape, of the particles.

The size distributions obtained with the different instruments were consistent with each other. Furthermore, they showed that silver nitrate precursor produced no residual particles, and the addition of EHA had no effect on the size distributions. Conversely, when using aluminum nitrate precursor dissolved in pure ethanol, the residual particles dominated the mass size distribution. However, only 5 volume percent of EHA in the solvent was required to shift the mass practically entirely to the nanoparticle mode. Such information is important, especially, when considering the production costs of nanoparticles at an industrial scale. As there are no previous studies on the effect of the EHA concentration, we can only speculate whether the low EHA requirement is solely a property of the hydrogen–oxygen flame due to its higher temperature compared to for example, methane–oxygen flame. Thus, additional research on this specific subject is required. In the current study, size dependent information on the produced particles was obtained due to the used measurement techniques. For example, the measured effective density of the alumina residual particles was approximately 4 g/cm,^{3} corresponding to spherical and non-hollow particles, while, for the nanoparticles, the mean effective density was below 1 g/cm,^{3} suggesting a high agglomeration state. These conclusions were supported by the electron microscopy images. Furthermore, the XRD analysis suggested that the residual and nanoparticles had the same crystal structure of γ-alumina.

This study demonstrates that measurements using aerosol analysis methods are an extremely viable method to study and evaluate the process output when producing nanopowders. Furthermore, we have shown that with a well-planned experimental system, the on-line measurements alone give valuable information on the process details of aerosol synthesis, including indirect information on the presence of unwanted residual particles, thus, in some situations, reducing the need for tedious off-line analyses. All in all, the methods described here can be adopted to both laboratory and industrial scale production of particles by different aerosol methods. The measurement techniques can be used for monitoring the particle production, as well as, studying novel precursors or the effect of different operational parameters.

Acknowledgments

Juha Harra acknowledges the TUT's graduate school for financial support. The authors thank Mr. Markus Nikka for assisting with the measurements.

Literature Cited

1. Kruis FE, Fissan H, Peled A. Synthesis of nanoparticles in the gas phase for electronic, optical and magnetic applications—a review. *J Aerosol Sci.* 1998;29(5–6):511–535.
2. Strobel R, Pratsinis SE. Flame aerosol synthesis of smart nanostructured materials. *J Mater Chem.* 2007;17(45):4743–4756.

3. Kulkarni P, Baron PA, Willeke K, editors. *Aerosol Measurement: Principles, Techniques, and Applications*, 3rd ed. Hoboken, NJ: Wiley, 2011.
4. Camata RP, Hirasawa M, Okuyama K, Takeuchi K. Observation of aerosol formation during laser ablation using a low-pressure differential mobility analyzer. *J Aerosol Sci.* 2000;31(4):391–401.
5. Hontañón E, Palomares JM, Stein M, Guo X, Engeln R, Nirschl H, Kruis FE. The transition from spark to arc discharge and its implications with respect to nanoparticle production. *J Nanopart Res.* 2013; 15(9):1957.
6. Ehrman SH, Friedlander SK. Bimodal distributions of two component metal oxide aerosols. *Aerosol Sci Technol.* 1999;30(3):259–272.
7. Aromaa M, Keskinen H, Mäkelä JM. The effect of process parameters on the Liquid Flame Spray generated titania nanoparticles. *Biomol Eng.* 2007;24(5):543–548.
8. Strobel R, Pratsinis SE. Effect of solvent composition on oxide morphology during flame spray pyrolysis of metal nitrates. *Phys Chem Chem Phys.* 2011;13(20):9246–9252.
9. Pratsinis SE. Flame aerosol synthesis of ceramic powders. *Prog Energy Combust Sci.* 1998;24(3):197–219.
10. Teoh WY, Amal R, Mädler L. Flame spray pyrolysis: An enabling technology for nanoparticles design and fabrication. *Nanoscale* 2010; 2(8):1324–1347.
11. Mädler L. Liquid-fed aerosol reactors for one-step synthesis of nanostructured particles. *KONA Powder Part J.* 2004;22:107–120.
12. Gurav A, Kodas T, Pluym T, Xiong Y. Aerosol processing of materials. *Aerosol Sci Technol.* 1993;19(4):411–452.
13. Messing GL, Zhang SC, Jayanthi GV. Ceramic powder synthesis by spray pyrolysis. *J Am Ceram Soc.* 1993;76(11):2707–2726.
14. Hinklin T, Toury B, Gervais C, Babonneau F, Gislason JJ, Morton RW, Laine RM. Liquid-feed flame spray pyrolysis of metalloorganic and inorganic alumina sources in the production of nanoalumina powders. *Chem Mater.* 2004;16(1):21–30.
15. Rosebrock CD, Wriedt T, Mädler L, Wegner K. The role of microexplosions in flame spray synthesis for homogeneous nanopowders from low-cost metal precursors. *AIChE J.* 2016;62(2):381–391.
16. Mädler L, Pratsinis SE. Bismuth oxide nanoparticles by flame spray pyrolysis. *J Am Ceram Soc.* 2002;85(7):1713–1718.
17. Jossen R, Pratsinis SE, Stark WJ, Mädler L. Criteria for flame-spray synthesis of hollow, shell-like, or inhomogeneous oxides. *J Am Ceram Soc.* 2005;88(6):1388–1393.
18. Mädler L, Stark WJ, Pratsinis SE. Flame-made ceria nanoparticles. *J Mater Res.* 2002;17(6):1356–1362.
19. Keskinen H, Mäkelä JM, Aromaa M, Ristimäki J, Kanerva T, Levänen E, Mäntylä T, Keskinen J. Effect of silver addition on the formation and deposition of titania nanoparticles produced by liquid flame spray. *J Nanopart Res.* 2007;9(4):569–588.
20. Chiarello GL, Rossetti I, Forni L, Lopinto P, Migliavacca G. Solvent nature effect in preparation of perovskites by flame pyrolysis: 2. Alcohols and alcohols + propionic acid mixtures. *Appl Catal B.* 2007;72:227–232.
21. Keskinen H, Mäkelä JM, Vippola M, Nurminen M, Liimatainen J, Lepistö T, Keskinen J. Generation of silver/palladium nanoparticles by liquid flame spray. *J Mater Res.* 2004;19(5):1544–1550.
22. Sotiriou GA, Teleki A, Camenzind A, Krumeich F, Meyer A, Panke S, Pratsinis SE. Nanosilver on nanostructured silica: Antibacterial activity and Ag surface area. *Chem Eng J.* 2011;170(2–3):547–554.
23. Schulz H, Mädler L, Strobel R, Jossen R, Pratsinis SE, Johannessen T. Independent control of metal cluster and ceramic particle characteristics during one-step synthesis of Pt/TiO_2. *J Mater Res.* 2005; 20(9):2568–2577.
24. Jossen R, Mueller R, Pratsinis SE, Watson M, Akhtar MK. Morphology and composition of spray-flame-made yttria-stabilized zirconia nanoparticles. *Nanotechnology* 2005;16(7):S609.
25. Yuvaraj S, Fan-Yuan L, Tsong-Huei C, Chuin-Tih Y. Thermal decomposition of metal nitrates in air and hydrogen environments. *J Phys Chem B.* 2003;107:1044–1047.
26. Wegner K, Schimmöller B, Thiebaut B, Fernandez C, Rao TN. Pilot plants for industrial nanoparticle production by flame spray pyrolysis. *KONA Powder Part J.* 2011;29:251–265.
27. Mädler L, Krumeich F, Burtscher P, Moszner N. Visibly transparent & radiopaque inorganic organic composites from flame-made mixed-oxide fillers. *J Nanopart Res.* 2006;8(3):323–333.
28. Rosebrock CD, Riefler N, Wriedt T, Mädler L, Tse SD. Disruptive burning of precursor/solvent droplets in flame-spray synthesis of nanoparticles. *AIChE J.* 2013;59:4553–4566.
29. Marple VA. History of impactors—The first 110 years. *Aerosol Sci Technol.* 2004;38:247–292.
30. Haynes WM, editor. *CRC Handbook of Chemistry and Physics*, 96th ed. Boca Raton, FL: CRC Press/Taylor and Francis, 2016.
31. Tikkanen J, Gross KA, Berndt CC, Pitkänen V, Keskinen J, Raghu S, Rajala M, Karthikeyan J. Characteristics of the liquid flame spray process. *Surf Coat Technol.* 1997;90:210–216.
32. Mäkelä JM, Aromaa M, Teisala H, Tuominen M, Stepien M, Saarinen JJ, Toivakka M, Kuusipalo J. Nanoparticle deposition from liquid flame spray onto moving roll-to-roll paperboard material. *Aerosol Sci Technol.* 2011;45(7):827–837.
33. Haapanen J, Aromaa M, Teisala H, Tuominen M, Stepien M, Saarinen JJ, Heikkilä M, Toivakka M, Kuusipalo J, Mäkelä JM. Binary TiO_2/SiO_2 nanoparticle coating for controlling the wetting properties of paperboard. *Mater Chem Phys.* 2015;149–150:230–237.
34. Harra J, Nikkanen JP, Aromaa M, Suhonen H, Honkanen M, Salminen T, Heinonen S, Levänen E, Mäkelä JM. Gas phase synthesis of encapsulated iron oxide–titanium dioxide composite nanoparticles by spray pyrolysis. *Powder Technol.* 2013;243:46–52.
35. Harra J, Juuti P, Haapanen J, Sorvali M, Roumeli E, Honkanen M, Vippola M, Yli-Ojanperä J, Mäkelä JM. Coating of silica and titania aerosol nanoparticles by silver vapor condensation. *Aerosol Sci Technol.* 2015;49:767–776.
36. Mäkelä JM, Aromaa M, Rostedt A, Krinke TJ, Janka K, Marjamäki M, Keskinen J. Liquid flame spray for generating metal and metal oxide nanoparticle test aerosol. *Hum Exp Toxicol.* 2009;28(6–7): 421–431.
37. Rostedt A, Marjamäki M, Keskinen J. Modification of the ELPI to measure mean particle effective density in real-time. *J Aerosol Sci.* 2009;40(9):823–831.
38. Keskinen H, Aromaa M, Heine MC, Mäkelä JM. Size and velocity measurements in sprays and particle-producing flame sprays. *Atomization Sprays.* 2008;18(7):619–644.
39. Mäkelä JM, Hellstén S, Silvonen J, Vippola M, Levänen E, Mäntylä T. Collection of liquid flame spray generated TiO_2 nanoparticles on stainless steel surface. *Mater Lett.* 2006;60(4):530–534.
40. Hinds WC. *Aerosol Technology: Properties, Behavior, and Measurement of Airborne Particles*, 2nd ed. New York, NY: Wiley, 1999.
41. Keskinen H, Mäkelä JM, Heikkinen R, Suopanki A, Keskinen J. Synthesis of Pd–alumina and Pd–lanthana suspension for catalytic applications by one-step Liquid Flame Spray. *Catal Lett.* 2007; 119(1):172–178.
42. Keskinen J, Pietarinen K, Lehtimäki M. Electrical low pressure impactor. *J Aerosol Sci.* 1992;23:353–360.
43. Arffman A, Kuuluvainen H, Harra J, Vuorinen O, Juuti P, Yli-Ojanperä J, Mäkelä JM, Keskinen J. The critical velocity of rebound determined for sub-micron silver particles with a variable nozzle area impactor. *J Aerosol Sci.* 2015;86:32–43.
44. Wang SC, Flagan RC. Scanning electrical mobility spectrometer. *Aerosol Sci Technol.* 1990;13(2):230–240.
45. Järvinen A, Aitomaa M, Rostedt A, Keskinen J, Yli-Ojanperä J. Calibration of the new electrical low pressure impactor (ELPI+). *J Aerosol Sci.* 2014;69:150–159.
46. Juuti P, Arffman A, Rostedt A, Harra J, Mäkelä JM, Keskinen J. Real-time effective density monitor (DENSMO) for aerosol nanoparticle production. *Aerosol Sci Technol.* 2016;50(5):487–496.
47. Mädler L, Kammler HK, Mueller R, Pratsinis SE. Controlled synthesis of nanostructured particles by flame spray pyrolysis. *J Aerosol Sci.* 2002;33(2):369–389.
48. Ristimäki J, Virtanen A, Marjamäki M, Rostedt A, Keskinen J. On-line measurement of size distribution and effective density of submicron aerosol particles. *J Aerosol Sci.* 2002;33(11):1541–1557.
49. Virtanen A, Ristimäki J, Keskinen J. Method for measuring effective density and fractal dimension of aerosol agglomerates. *Aerosol Sci Technol.* 2004;38(5):437–446.
50. Tani T, Watanabe N, Takatori K, Pratsinis SE. Morphology of oxide particles made by the emulsion combustion method. *J Am Ceram Soc.* 2003;86(6):898–904.
51. Heine MC, Pratsinis SE. Droplet and particle dynamics during flame spray synthesis of nanoparticles. *Ind Eng Chem Res.* 2005;44:6222–6232.
52. Zhou RS, Snyder RL. Structures and transformation mechanisms of the η, γ and θ transition aluminas. *Acta Crystallogr B.* 1991;B47(5): 617–630.
53. Nikkanen JP, Harju M, Järn M, Linden J, Rintala J, Messing ME, Huttunen-Saarivirta E, Saarinen T, Kanerva T, Honkanen M, Aromaa M, Levänen E, Pettersson M, Mäkelä JM, Deppert K, Mäntylä T. Synthesis of carbon nanotubes on Fe_xO_y doped Al_2O_3–ZrO_2 nanopowder. *Powder Technol.* 2014;266:106–112.

54. Strobel R, Stark WJ, Mädler L, Pratsinis SE, Baiker A. Flame-made platinum/alumina: Structural properties and catalytic behaviour in enantioselective hydrogenation. *J Catal.* 2003;213(2): 296–304.
55. Karthikeyan J, Berndt CC, Tikkanen J, Wang JY, King AH, Herman H. Nanomaterial powders and deposits prepared by flame spray processing of liquid precursors. *Nanostruct Mater.* 1997; 8(1):61–74.
56. Levi CG, Jayaram V, Valencia JJ, Mehrabian R. Phase selection in electrohydrodynamic atomization of alumina. *J Mater Res.* 1988;3: 969–983.
57. McHale JM, Auroux A, Perrotta AJ, Navrotsky A. Surface energies and thermodynamic phase stability in nanocrystalline aluminas. *Science* 1997;277(5327):788–791.
58. Backman U, Jokiniemi JK, Auvinen A, Lehtinen KE. The effect of boundary conditions on gas-phase synthesised silver nanoparticles. *J Nanopart Res.* 2002;4(4):325–335.
59. Harra J, Mäkitalo J, Siikanen R, Virkki M, Genty G, Kobayashi T, Kauranen M, Mäkelä JM. Size-controlled aerosol synthesis of silver nanoparticles for plasmonic materials. *J Nanopart Res.* 2012;14(6):870

Manuscript received Apr. 15, 2016, and revision received July 12, 2016.

Paper

III

Achieving a slippery, liquid-infused porous surface with anti-icing properties by direct deposition of flame synthesized aerosol nanoparticles on a thermally fragile substrate

Juuti, P., Haapanen, J., Stenroos, C., Niemelä-Anttonen, H., Harra, J., Koivuluoto, H., Teisala, H., Lahti, J., Tuominen, M., Kuusipalo, J., Vuoristo, P. & Mäkelä, J.M.

Applied Physics Letters, 2017, 110, 161603
DOI: 10.1063/1.4981905

III

Achieving a slippery, liquid-infused porous surface with anti-icing properties by direct deposition of flame synthesized aerosol nanoparticles on a thermally fragile substrate

Paxton Juuti,[1,a)] Janne Haapanen,[1] Christian Stenroos,[2] Henna Niemelä-Anttonen,[2] Juha Harra,[1] Heli Koivuluoto,[2] Hannu Teisala,[3] Johanna Lahti,[3] Mikko Tuominen,[4] Jurkka Kuusipalo,[3] Petri Vuoristo,[2] and Jyrki M. Mäkelä[1]

[1]*Aerosol Physics, Laboratory of Physics, Tampere University of Technology, P.O. Box 692, 33101 Tampere, Finland*

[2]*Surface Engineering Research Team, Laboratory of Materials Science, Tampere University of Technology, P.O. Box 589, 33101 Tampere, Finland*

[3]*Packaging Technology Research Team, Laboratory of Materials Science, Tampere University of Technology, P.O. Box 589, 33101 Tampere, Finland*

[4]*SP Technical Research Institute of Sweden, Drottning Kristinas Väg 45, 11428 Stockholm, Sweden*

(Received 6 February 2017; accepted 6 April 2017; published online 20 April 2017)

Slippery, liquid-infused porous surfaces offer a promising route for producing omniphobic and anti-icing surfaces. Typically, these surfaces are made as a coating with expensive and time consuming assembly methods or with fluorinated films and oils. We report on a route for producing liquid-infused surfaces, which utilizes a liquid precursor fed oxygen-hydrogen flame to produce titania nanoparticles deposited directly on a low-density polyethylene film. This porous nanocoating, with thickness of several hundreds of nanometers, is then filled with silicone oil. The produced surfaces are shown to exhibit excellent anti-icing properties, with an ice adhesion strength of ~12 kPa, which is an order of magnitude improvement when compared to the plain polyethylene film. The surface was also capable of maintaining this property even after cyclic icing testing. *Published by AIP Publishing.* [http://dx.doi.org/10.1063/1.4981905]

Slippery, liquid-infused porous surfaces (SLIPSs) are nature inspired surfaces that are designed to repel liquid and solid materials.[1] These surfaces have been shown to pose anti-icing properties,[2] which broadens the available end-uses from the chemical industry to arctic transportation and energy production. The method behind repellency of SLIPSs relies on preventing outside liquids from penetrating the surface structure to the Wenzel state. Instead, the slippery liquid within the porous solid supports the Cassie-Baxter state (instead of air, here the porous structure is filled with lubricant), where the reduced area of the porous solid surface is available to interact with the liquid or ice to be repelled.[3] The difference between Wenzel and Cassie-Baxter states is illustrated in Figure 1. This phenomenon is exploited in many superhydrophobic surfaces where an air cushion is entrapped within the porous solid surface. As a result, spherical water drops easily roll off the surface (and have static contact angles larger than 150° [4]).

The porous structure can be achieved, for example, with nanoposts or with a fibrous material, such as the PTFE-fibre film. We propose an alternative route for producing a SLIPS via direct nanoparticle surface coating utilizing Liquid Flame Spray (LFS[5,6]) LFS is a promising method as it enables *in-situ* processing and is more readily scalable on various substrate materials than other methods, both chemical and mechanical,[7] and is more cost efficient than most approaches reported in the literature to process porous surfaces.

The preparation of the SLIPS samples in this work consists of two distinct phases: first, coating of a substrate with titania (TiO_2) nanoparticles and second, infusing the porous layer with oil. This process is schematically illustrated in Figure 2.

A 20 μm thick low-density polyethylene (LDPE) film was used as the substrate for the SLIPS. This material was chosen for its wide spread use and inexpensiveness. Also, LDPE being thin and thermally fragile, it can be easily substituted with more robust materials like metals and glasses. The required porous layer was achieved by coating the substrate with titanium-oxide agglomerates with 20–30 nm primary particle size. The nanoparticle synthesis was carried out with LFS by introducing a 12 ml/min liquid precursor feed of titanium(IV) isopropoxide (TTIP, Alfa Aesar, 97+) and isopropyl alcohol (VWR, HPLC grade), with a titanium mass concentration of 50 mg/ml, into a turbulent oxygen-hydrogen flame ($H_2/O_2 = 50/15$ lpm). The substrate was passed through the flame (15 cm from the base of the burner), with a velocity of 50 m/min, 10 times.[5] This repeated coating process produces a 0.5–1 μm thick coating

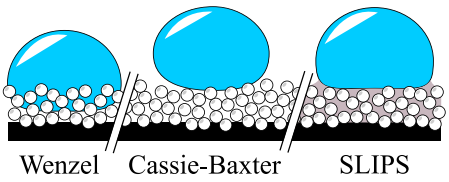

FIG. 1. The manifestation of Wenzel and Cassie-Baxter states on a surface coated with nanoparticles. In SLIPS, the Cassie-Baxter state is favored due to oil filled pores.

a)Author to whom correspondence should be addressed. Electronic mail: paxton.juuti@tut.fi

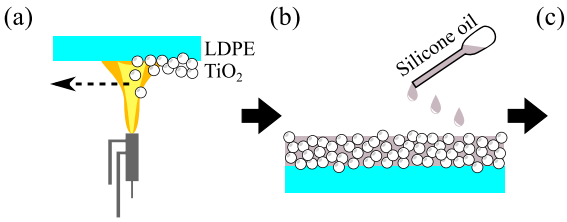

FIG. 2. Schematic illustration of the preparation of SLIPS. Sub-figures depict: (a) nanoparticle synthesis with LFS and subsequent deposition on LDPE, (b) filling the porous structure with oil, and (c) the final surface exhibiting icephobicity and water repellency.

with excess of 90% porosity.[8] This porous structure was then pipetted full with silicone oil with a viscosity of 50 cSt (25 °C, Sigma Aldrich). A great deal of care was taken not to overfill the samples with the oil, by letting the oil infiltrate into the structure on its own, as not to only test the oil surface in the following tests.[9] For reference purposes, additional surfaces were prepared with only a porous non-oiled nanoparticle coating and a plain LDPE film surface with added silicone oil.

The surfaces were tested with a contact angle meter (KSV Instruments CAM 200) to characterize the static water contact (WCA) and dynamic sliding (WSA) angles. The WCA and WSA testing was carried out with automatic dispensing of 5 and 10 μl water droplets, respectively. The sliding angles were measured in the range of 0 to ~90°, and if no sliding was observed, the droplet was deemed pinned to the surface.

Next, icing behavior was evaluated by accreting ice on the surface in an icing wind tunnel located in a cold climate room.[10] The temperature was kept at –10 °C, and the air flow velocity was set to 25 m/s. The mixed ice was accreted from supercooled water droplets, with a volume median diameter of 31 μm. Ice adhesion strength values were measured through centrifugal force required to detach the ice from the surface. The sample, with accumulated ice of mass m and contact surface area of A, is attached to a radial arm of length r that spins with a constant angular acceleration α (300 rpm/s), which yields a following ice adhesion strength via shear stress at detachment time t.

$$\tau = \frac{F}{A} = \frac{mr\omega^2}{A} = \frac{mr(\alpha t)^2}{A}. \quad (1)$$

This cycle of water behavior testing followed by the ice adhesion strength testing was carried out for four times followed by final WCA and WSA measurements.

Furthermore, the produced nanocoating was imaged using a field-emission scanning electron microscope (FESEM, Zeiss ULTRAplus) to ascertain the uniformity of the coating and verify the primary particle size of the agglomerates. SEM micrographs of the surface are shown in Figure 3.

Measurements were performed for three different surfaces: LFS treated, which consists of TiO_2 nanoparticle coated LDPE, oiled plain LDPE, and the complete SLIPS, which has both TiO_2 nanostructures and oil. For reference purposes, also commercially available PTFE-tape was tested in the ice adhesion strength measurements.

The WCA measurements indicate that the apparent contact angles between the water droplet and both oiled surfaces are similar. However, to balance the interfacial tensions between the solid and the liquids, oil forms an annular wetting ridge around the water droplet (Figure 1), preventing us from seeing the real water-solid contact angles, which are higher than the apparent ones.[11,12] These results are shown in Figure 4. The superhydrophobicity of the initial TiO_2 surface is also clear with its WCA value being over 150°. The WCA values decrease as the titania nanocoating is stressed over the cyclic buildup and removal of ice, which can be

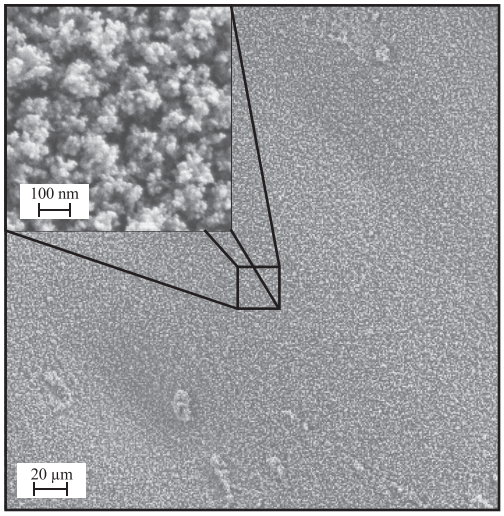

FIG. 3. FESEM micrographs of LFS coated LDPE. The layer has not been infused with oil here.

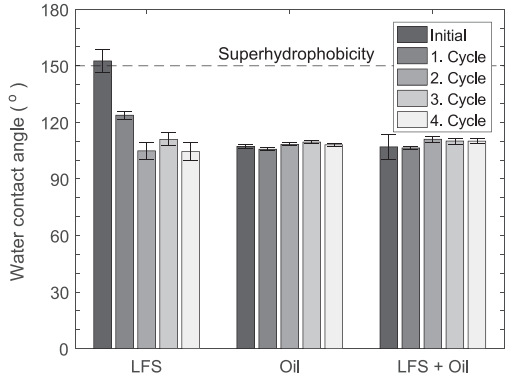

FIG. 4. Apparent water contact angle measurements before and after each of the four ice adhesion tests. The inset shows the superhydrophobicity of the initial LFS coating. Error bars denote standard deviation between four parallel measurements.

caused by the pressure and shear forces affecting the structure or the coating losing its surface hydrocarbons.[13]

The WSA measurements show that even though the nanocoating is initially superhydrophobic based on its contact angle, the droplets are pinned to the surface, which can be tilted upside down without losing the droplet from the surface. This is explained by water's ability to penetrate into the porous structure (the droplet resides partially in the Wenzel state).[14] The initial surface of the oil-infused structure displays a complete opposite behavior with a water sliding angle value of ~3°, which satisfies the additional requirement for superhydrophobicity of WSA lower than 10°. This value shows an increase in the level of the plain oiled surface after the first cycle of the ice adhesion testing. The results of these measurements are given in Figure 5. The change in the WSA after the first testing cycle indicates a change in the surface caused by the icing and de-icing process. Either the surface roughness is reduced, which has been shown to affect wetting properties,[15] or the oil coverage is affected over the topmost peaks of the porous nanoparticle structure.

The ice adhesion measurements reveal a significant difference in the anti-icing capabilities of the oil-infused surface when compared to a surface without oil impregnation. As can be seen in Figure 6, the nanoporous coating is capable of holding the oil at the solid-ice interface and thus reducing the ice adhesion. The SLIPS exhibits values averaging at 12 kPa, which has improved by almost a factor of three compared to the plain oiled LDPE film surfaces averaging at 34 kPa. Comparably, the non-oiled nanoparticle coating alone cannot replicate the results either. As is highly probable based on the WSA measurements, water droplets get pinned to the surface, and thus, the ice will have a mechanical hold on the surface, resulting in mechanical interlocking effect[16] and an increased ice adhesion strength. All of the oiled samples were also notably better icephobic surfaces than the reference PTFE-tape (WCA = 110°, WSA = 10°), which can be clearly seen in the lowest ice adhesion strength values of the PTFE-tape and the SLIPS, 44 and 9 kPa, respectively.

The results from the cyclic ice adhesion testing show excellent performance, which can be attributed to the ideal

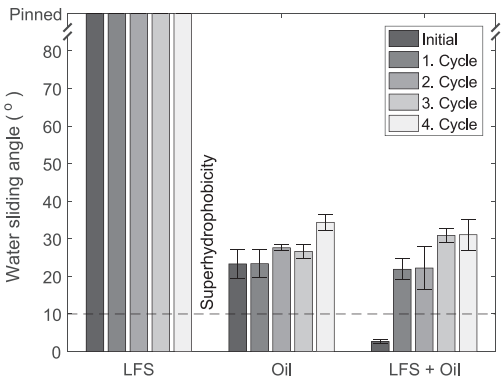

FIG. 5. Water sliding angle measurements before and after each of the four ice adhesion tests. Insets show the pinning of the water droplet on the initial LFS coating and the sliding angle on silicone oil coated smooth LDPE (~25°). Error bars denote standard deviation between four parallel measurements.

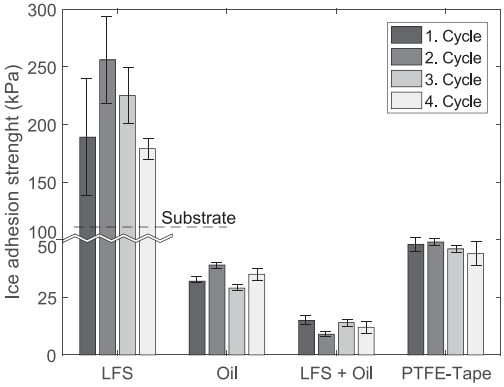

FIG. 6. Ice adhesion measurement results. Ice adhesion strength of the plain LDPE surface is 110 kPa. Error bars denote standard deviation between four independent measurements.

testing of new samples. For further study, these samples should be tested cyclically or in climate conditions until some form of aging can be observed, e.g., due to lubricant loss in dynamic water-air-lubricant interfaces[17] or restructuring of the nanoparticle layer.[13]

Slippery, liquid-infused porous surfaces were prepared by introducing silicone oil into porous TiO_2 nanoparticle coating, generated with flame based aerosol synthesis method, LFS. These surfaces were shown to exhibit excellent anti-icing properties in cyclic ice adhesion testing. The substrate material of LDPE was transformed into SLIPS, and in the process, its ice adhesion strength decreased an order of magnitude from 110 kPa to 12 kPa, which lasted for several testing cycles. Furthermore, after performing the process on a thermally fragile material, it can be performed on other materials with better confidence. These results were also obtained without the typically used fluorinated compounds and with a scalable method.

The authors acknowledge the Finnish Funding Agency for Technology and Innovation (Tekes) for funding this study under the project "Roll-to-roll fabrication of advanced slippery liquid-infused porous surfaces for anti-icing applications" (Grant No. 40365/14, ROLLIPS). H.T. acknowledges Walter Ahlström foundation for the financial support.

[1]T.-S. Wong, S. Kang, S. Tang, E. Smythe, B. Hatton, A. Grinthal, and J. Aizenberg, Nature **477**, 443 (2011).
[2]P. Kim, T.-S. Wong, J. Alvarenga, M. Kreder, W. Adorno-Martinez, and J. Aizenberg, ACS Nano **6**, 6569 (2012).
[3]A. Cassie and S. Baxter, Trans. Faraday Soc. **40**, 546 (1944).
[4]X.-M. Li, D. Reinhoudt, and M. Crego-Calama, Chem. Soc. Rev. **36**, 1350 (2007).
[5]M. Aromaa, A. Arffman, H. Suhonen, J. Haapanen, J. Keskinen, M. Honkanen, J.-P. Nikkanen, E. Levänen, M. Messing, K. Deppert, H. Teisala, M. Tuominen, J. Kuusipalo, M. Stepien, J. Saarinen, M. Toivakka, and J. Mäkelä, J. Aerosol Sci. **52**, 57 (2012).
[6]J. Mäkelä, J. Haapanen, J. Harra, P. Juuti, and S. Kujanpää, KONA Powder Part. J **34**, 141 (2016).
[7]P. Zhang and F. Lv, Energy **82**, 1068 (2015).
[8]L. Mädler, A. Lall, and S. Friedlander, Nanotechnology **17**, 4783 (2006).
[9]S. Subramanyam, K. Rykaczewski, and K. Varanasi, Langmuir **29**, 13414 (2013).

[10]H. Koivuluoto, C. Stenroos, R. Ruohomaa, G. Bolelli, L. Lusvarghi, and P. Vuoristo, in *Proceedings of 16th International Workshop on Atmospheric Icing of Structures* (Uppsala, Sweden, 2015), pp. 183–188.
[11]F. Schellenberger, J. Xie, N. Encinas, A. Hardy, M. Klapper, P. Papadopoulos, H.-J. Butt, and D. Vollmer, Soft Matter **11**, 7617 (2015).
[12]J. Smith, R. Dhiman, S. Anand, E. Reza-Garduno, R. Cohen, G. McKinley, and K. Varanasi, Soft Matter **9**, 1772 (2013).
[13]M. Tuominen, H. Teisala, J. Haapanen, J. Mäkelä, M. Honkanen, S. Vippola, M. Bardage, M. Wålinder, and A. Swerin, Appl. Surf. Sci. **389**, 135 (2016).
[14]H. Teisala, M. Tuominen, M. Aromaa, M. Stepien, J. Mäkelä, J. Saarinen, M. Toivakka, and J. Kuusipalo, Langmuir **28**, 3138 (2012).
[15]M. Stepien, J. Saarinen, H. Teisala, M. Tuominen, J. Haapanen, J. Mäkelä, J. Kuusipalo, and M. Toivakka, Nanoscale Res. Lett. **8**, 444 (2013).
[16]J. Chen, J. Liu, M. He, K. Li, D. Cui, Q. Zhang, X. Zeng, Y. Zhang, J. Wang, and Y. Song, Appl. Phys. Lett. **101**, 111603 (2012).
[17]C. Howell, T. Vu, C. Johnson, X. Hou, O. Ahanotu, J. Alverenga, D. Leslie, O. Uzun, A. Waterhouse, P. Kim, M. Super, M. Aizenberg, D. Ingber, and J. Aizenberg, Chem. Mater. **27**, 1792 (2015).

Paper

IV

Fabrication of fiber filters with antibacterial properties for VOC and particle removal

Juuti, P., Nikka, M., Gunell, M., Eerola, E., Saarinen, J.J., Omori, Y., Seto, T. & Mäkelä, J.M.

Aerosol and Air Quality Research, 2019, 19: 1892 – 1899
DOI: 10.4209/aaqr.2018.12.0474

Aerosol and Air Quality Research, 19: 1892–1899, 2019

ISSN: 1680-8584 print / 2071-1409 online
doi: 10.4209/aaqr.2018.12.0474

Fabrication of Fiber Filters with Antibacterial Properties for VOC and Particle Removal

Paxton Juuti[1*], Markus Nikka[1], Marianne Gunell[2,3], Erkki Eerola[2,3] Jarkko J. Saarinen[4], Youichi Omori[5], Takafumi Seto[6], Jyrki M. Mäkelä[1]

[1] *Aerosol Physics, Faculty of Engineering and Natural Sciences, Tampere University, 33720 Tampere, Finland*
[2] *Department of Clinical Microbiology, Turku University Hospital, 20521 Turku, Finland*
[3] *Department of Medical Microbiology and Immunology, University of Turku, 20500 Turku, Finland*
[4] *Department of Chemistry, University of Eastern Finland, Joensuu, Finland*
[5] *Sanzen Seishi Co. Ltd., Kanazawa, Ishikawa 920-0338, Japan*
[6] *School of Natural System, College of Science and Engineering, Kanazawa University, Kanazawa, Ishikawa 920-1192, Japan*

IV

ABSTRACT

The use of filters to control air quality has been implemented widely in all types of structures. Unfortunately, filters risk becoming platforms for the growth of bacteria, which can then be dispersed further in the air stream. To combat this, antibacterial materials are being incorporated into filter media. In this work, we tested two routes for introducing nanoscale silver into filters containing activated carbon fibers (ACF): first, by adding silver nanofibers directly to the fiber fabrication process and second, by coating a pre-existing filter with silver nanoparticles generated by a liquid flame spray (LFS). The resultant filters were evaluated for methanol adsorption, particle penetration and antibacterial activity. The results show that both methods are suitable for producing antibacterial filters as well as being highly tailorable and scalable for specific needs.

Keywords: Air filtration; Liquid flame spray; Nanoscale silver; Adsorption.

INTRODUCTION

Indoor air quality has an important role on human health (Jones, 1999), and, worryingly, its impacts can be seen in institutes such as schools (Daisey *et al.*, 2003) and hospitals (Saad, 2002). One way to improve the quality of indoor air is to utilize filtration in the air conditioning system. However, filters are susceptible to becoming growing platforms for microbes, especially in humid conditions (Möritz *et al.*, 2001; Forthomme *et al.*, 2014). Furthermore, biocompatible carbon-based adsorptive materials can also be used if volatile organic compounds (VOCs), such as formaldehyde (Rumchev *et al.*, 2002), are desired to be filtered from air alongside with the particulate matter. Unfortunately, due to their good biocompatibility, carbon-based materials could make the filters more susceptible to microbes (Yoon *et al.*, 2008). To combat these problems, antimicrobial materials have been widely adopted in material functionalization. Arguably, the most widely used material for this purpose currently is silver (Oya *et al.*, 1993; Jung *et al.*, 2011; Brobbey *et al.*, 2017), but also metal oxides, such as zinc oxide (Gordon *et al.*, 2011) and copper oxide (Hassan *et al.*, 2014), are being utilized. In humid conditions where bacterial growth might pose a risk, the use of silver nanoparticles should be very effective against bacterial growth, due to the transfer of silver ions and whole nanoparticles, which can disrupt the vital functions of the bacterial cells (Sotiriou and Pratsinis, 2010).

Here, we take a closer look at fabricating fiber filters containing activated carbon fibers (ACF) and adding antibacterial silver in two different morphologies: (1) fibers and (2) particles. The silver fibers will be added during the filter fabrication process, whereas the particles will be added to an already fabricated filter as a coating. For the nanoparticle coating, the liquid flame spray (LFS; Tikkanen *et al.*, 1994; Mäkelä *et al.*, 2017) method will be implemented. It has been used quite extensively for introducing nanoparticle coatings on a wide range of materials, most recently on paper (Haapanen *et al.*, 2018), glass (Teisala *et al.*, 2018) and plastic (Juuti *et al.*, 2017). The LFS method can produce other metal and metal-oxide particles and is readily scalable, so the process investigated here has

* Corresponding author.
Tel.: +358 40 1981026
E-mail address: paxton.juuti@tuni.fi

potential for future antibacterial materials as well. In essence, we introduce a scalable and tailorable approach for fabricating filters containing fibrous and particulate nanoscale silver and compare their antibacterial activities against *Staphylococcus aureus* (*S. aureus*) and *Escherichia coli* (*E. coli*). Furthermore, the filters will be tested for particle penetration and methanol adsorption capability to ascertain their functionality as a proper and usable filtration medium.

MATERIALS AND METHODS

Filter Media Fabrication

Three different kinds of fiber filter media were produced by mixing known mass ratios (see Table 1) of select fiber materials. The fiber filters were prepared by first premixing the appropriate amount of micro- and nanofibers into 500 cm^3 of water to make a 0.28% slurry, which was then mixed for 2 min at 3000 rpm. The premixed slurry was then diluted to 0.019% in paper processing equipment by introducing an additional 7000 cm^3 of water. To make the filter discs, the slurry was filtered with mesh, leaving a thin filter medium on top. Lastly, to remove the residual water from the filter structure, the filter discs were dried at 80°C for 25 min. The three prepared filter media all have the same base composition of glass fibers, binding polyvinyl alcohol (PVA) fibers and activated carbon fibers (ACF), with diameters of 10.5, 10 and 18 μm respectively. The second and third filter media get an addition of ~300 nm glass nanofibers in the fiber mixture. Lastly, only the third filter medium has 1 m-% of silver nanofibers (30 nm; Sanzen Seishi Co., Ltd.) substituting equal mass of the glass nanofibers. These filter media have the following denotations: F0 is the microfiber filter, F1 is the glass nanofiber filter and F2 is the silver nanofiber filter, noting that the addition of a different fiber material is cumulative through the series, which can be seen clearly from Table 1.

Coating of the Filter Media

Another route for adding the nanoscale silver to the filter media was utilized by coating an already prepared F1 filter media with the LFS method. The coating setup can be seen in Fig. 1(a). The LFS produced nanoscale silver from an aqueous silver nitrate ($AgNO_3$) precursor (silver nitrate, ACS, 99.9+% [metals basis]; Alfa Aesar) solution with a concentration of 125 mg mL^{-1} of pure silver, which was fed with a flow rate of 4 mL min^{-1}. The precursor was thermally decomposed and evaporated in a hydrogen-oxygen flame with a gas-ratio of 20 to 10 L min^{-1}, respectively, with an additional collar flow of 5 L min^{-1} of nitrogen. The silver condensed and the final particle shape was formed fully in the following residence tube (Sorvali *et al.*, 2017), from where it was sampled with an inlet connected to an ejector diluter (ED), further diluted and cooled, and guided to be deposited on the filter media. A similar synthesis protocol was implemented recently in the work of Harra *et al.* (2017) for silver and aluminum oxide. This produced the fourth filter medium studied in this work and is denoted as F3, and the mass fractions of its constituent fibers can be seen in Table 1.

For comparable results, the mass loading of the deposited silver coating was kept constant between the as-prepared silver nanofiber filter and the silver-coated filter. To achieve this, the measurement of the process is required in addition to the penetration characteristics of the filter being coated, which is discussed in the next chapter. The instruments require additional dilution of the sample, so an additional ejector diluter was used. The number size distribution of the nanoscale silver was measured using a Scanning Mobility Particle Sizer (SMPS; Model 3938; TSI Inc.), which was paired with the aerodynamic sizing of an Electrical Low Pressure Impactor (ELPI+; Dekati) in order to get additional information on the effective density (ρ_{eff}). The effective density can be calculated using the following equation (Kulkarni *et al.*, 2011):

$$\rho_{eff} = \rho_0 \frac{C_c(d_a) d_a^2}{C_c(d_b) d_b^2}, \quad (1)$$

where ρ_0 is the unit density, C_c is the slip correction factor, and d_b and d_a are mobility and aerodynamic diameters measured by SMPS and ELPI+, respectively. For real-time monitoring purposes, DENSMO (Juuti *et al.*, 2016) was used in parallel with the previous instruments. It also utilizes Eq. (1) for characterizing the effective density. DENSMO operates based on the series measurement of mobility median and aerodynamic median diameters. The measurements are done electrically, so the aerosol particles are first charged with a corona charger.

For mass characterization, a Tapered Element Oscillating Microbalance (TEOM; Rupprecht & Patashnick Co., Inc.) and a Quartz Crystal Microbalance Micro-Orifice Uniform Deposition Impactor (QCM-MOUDI; TSI Inc.) were used for measuring the total mass concentration and the mass-size distribution, respectively. Additional estimation of the

Table 1. Composition of fabricated filters.

	Microfibers F0	Nanofibers F1	Ag-fibers F2	Ag-particles F3	
Glass fibers	60	50	50	49.5	m-%
PVA fibers	25	25	25	24.8	m-%
Activated carbon fibers	15	15	15	14.9	m-%
Glass nanofibers		10	9	9.9	m-%
Ag nanofibers			1	-	m-%
Ag nanoparticles				1	m-%

mass-size distribution was obtained through the number-size and effective density measurements described above.

Methanol Adsorption

The performance of the ACF in the filters against VOCs were tested with the adsorption of methanol, which is a typical VOC. Measurements were done with a similar apparatus as described by Kumita *et al.* (2018); the measurement setup is shown in Fig. 1(b). The apparatus consists of three temperature-controlled chambers: one with liquid methanol, one for storing the methanol vapor and the last with the tested sample in it. The adsorption of methanol was measured as a function of relative pressure, which is a proportion of the saturated vapor pressure of methanol at 30°C. First, a vacuum was pulled to the second and third chambers to remove all of the present water. Then, increasing pressures of methanol vapor were introduced to the second chamber. At each pressure point, the sample is allowed to adsorb the VOC vapor by connecting the second and third chambers together. When the pressure stops decreasing, the value is logged. For comparison, the amount of adsorbed methanol, q, as a function of relative pressure for pure ACF was used as reference. The same apparatus was also used for quantifying the volume of each of the filter media to know the space occupied by the filter in the third chamber and thus the pressure drop caused by the connection of the second and third chamber. Additionally, by knowing the dimensions of the filter disk, mass fractions of the utilized filter fibers and the total mass of the filters, packing density (α) values can be calculated. The relevant values are shown in Table 2 and were used for the calculation of the theoretical particle penetration, utilizing the theory described by Choi *et al.* (2017). An overview of the theory is given in the next section.

Particle Penetration

The theoretical penetration, P, of the fiber filters can be calculated, assuming monodisperse fiber diameters, d_f, with the following equation:

$$P = \exp\left\{-\frac{4}{\pi}\frac{\alpha}{(1-\alpha)}\frac{L}{\bar{d}_f}\frac{\eta}{\delta}\right\}, \quad (2)$$

where L is the filter thickness, δ is an inhomogeneity factor

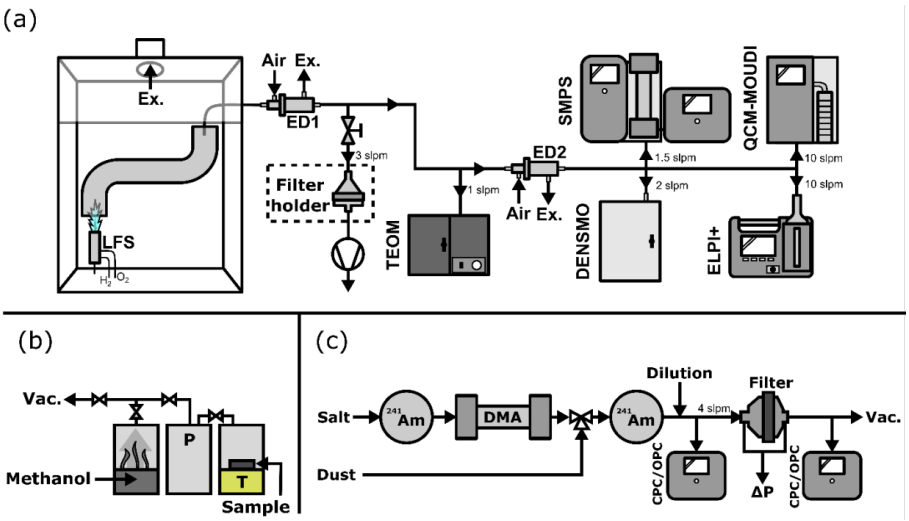

Fig. 1. Experimental setups for (a) the nanoparticle coating process, (b) the methanol adsorption measurements and (c) the particle penetration measurements. In the particle penetration measurements, two particle sources were used: Salt was generated with a tubular furnace and dust particles with a brush generator.

Table 2. Specifications relating to the filter structure and performance.

		Microfibers F0	Nanofibers F1	Ag-fibers F2	
Thickness	L	0.65	0.51	0.48	mm
Diameter		47	47	47	mm
Area density	W	54.4	63.7	62.7	g m^{-2}
Pressure drop (at 3.8 cm s^{-1})	ΔP	4.5	35.1	33.0	Pa
Pressure drop, theoretical	ΔP_t	10.2	38.4	43.1	Pa
Packing density	α	0.145	0.277	0.314	

defined as the ratio between the theoretical and the measured pressure drops and η is the combined collection efficiency of diffusion and interception collection mechanisms, as well as their interaction term. As the prepared filters contained both microfibers and nanofibers, it is considered a mixed fiber filter. The effect the different collection mechanisms have can be first considered separately for these different diameter fibers and then combined later. This penetration is calculated for the micro- and nanofibers separately and then combined with the following equation:

$$P = \exp(\ln P_M + \ln P_N), \quad (3)$$

where the subscripts denote the contributions of micro- M and nano- N fibers.

The particle penetration of the filters was tested by introducing particles in the range of 30 nm–7 µm and measuring the downstream and upstream particle concentrations with a condensation particle counter (CPC; Model 3775; TSI Inc.) or an optical particle counter (OPC; Model 3080; TSI Inc.) based on their measurement ranges. Salt (NaCl) produced by a tubular furnace was used to produce the smaller particles and a fluidized bed aerosol generator (Model 3080; Kanomax) was used to disperse JIS Class 11 test powder (SP3-3, Association of Powder Process Industry and Engineering), generating the larger end of the size range. The test setup is shown in Fig. 1(c), where the whole dust number size distribution is filtered by the test filter and the salt particles are size selected so that only a monodisperse distribution is being filtered at a time. The face velocity of the aerosol penetrating the filter was kept at 3.8 cm s^{-1}.

Antibacterial Testing

Antibacterial capabilities of the prepared filters were tested with a touch test method, described in the work by Gunell *et al.* (2017), against gram-negative *E. coli* (ATCC 25922) and gram-positive *S. aureus* (methicillin-susceptible strain, ATCC 29213) on blood agar plates (Trypticase Soy Agar with 5% Sheep Blood [II]; BD). Here, the reference sample was the filter F1, which contains all the other kinds of fibers excluding silver, which was compared against F2 and F3. The bacteria were incubated on the samples at room temperature for 24 and 48 h, after which the samples were placed on the blood agar plates to transfer any viable bacteria to be calculated the next day. The bacterial growth was estimated based on the amount of colony forming units (CFUs) in the range of 0–3, as per the method definition: 0 meaning no growth and going up to 3, meaning good growth with > 100 colonies.

RESULTS AND DISCUSSION

Coating Mass Loading

The results from the coating process characterization can be seen in Fig. 2, where the results have been split into (a) number and (b) mass concentration plots. The produced silver particles have a count mean diameter (CMD) of 43 nm based on the SMPS measurement and aerodynamic mean diameter of 258 nm based on the ELPI+ measurement. Using Eq. (1), an effective density value of 10.2 g cm^{-3} can be calculated, which tells us that the silver is mostly non-agglomerated and close to spherical in shape. Information about the measured silver nanoparticle number size distribution was needed in the estimation of what part of it is deposited on the filter fibers. To achieve this, the information was combined with the filter particle collection efficiency.

The mass measurements made with the TEOM and QCM-MOUDI give similar results on the total mass concentration with measured values of 15.6 mg m^{-3} and 16.1 mg m^{-3}, respectively. This mass concentration is determined after the first ejector diluter, after which the

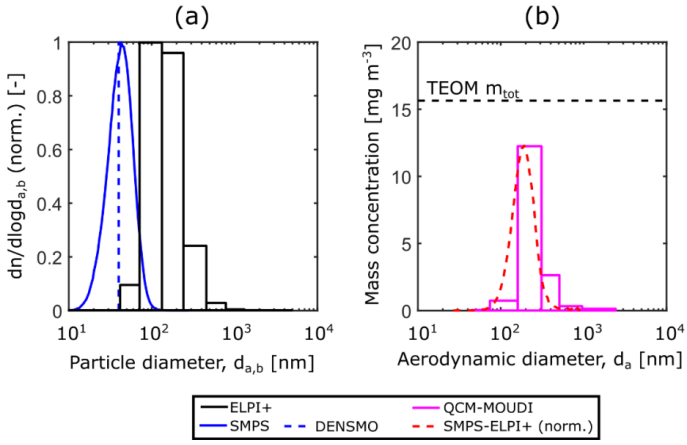

Fig. 2. Aerosol measurements for the mass loading estimation. Left side shows the SMPS- and ELPI+-measured number size distributions of the coating particles as a function of mobility size and aerodynamic size, respectively. Dashed line shows the time averaged CMD value from DENSMO. Right side shows the mass size distribution from QCM-MOUDI and a normalized one from the SMPS-ELPI+ estimation, and the total mass concentration from TEOM.

aerosol is directed to the filter holder; thus, the mass concentration flowing into the filter holder is the same. Another way to estimate the mass distribution is to use the measurement results from the SMPS and ELPI+. This calculated distribution is shown normalized in Fig. 2(b) and yields a total mass concentration of 14.5 mg m^{-3}. In order to achieve the 1 m-% coating of silver, approximately a 25 min coating time was required. To have more even distribution of the silver inside the filter media, the coating was done in two 12.5 min parts, one for each side of the filter media.

Given that the two ejector diluters both have a dilution factor of about 8, an estimate can be made of the dilution factor of the residence tube. The residence tube affects the total mass of the produced silver, with the used parameters, by a factor of 125. This dilution was caused by diffusion and possible impaction of precursor droplets, as well as the convective air flow of the surrounding air. The high flow rate of the generation method enables scaling up, where more of the produced silver could be sampled with parallelizing multiple inlets or just scaling the current one.

The process was also monitored with DENSMO so that the stability of the mobility diameter, aerodynamic diameter and effective density could be observed in real time during the coating. DENSMO measured the CMD to be 40 nm and the effective density value as 11.2 g cm^{-3}, which are both within the measurement range from the 43 nm measured by the SMPS and the effective density of 10.2 g cm^{-3} calculated from the SMPS and ELPI+ measurements.

SEM Micrography

To have a better understanding of the structure and distribution of the fibers in the produced filter media, as well as the result of the nanoparticle coating, a scanning electron microscope (SEM; ULTRA plus; ZEISS) was used. Fig. 3 shows the as-prepared filters F0 and F1, and the coated filter F3. F2 is not shown, due to having identical appearance to F1. The low count and the narrow diameter of the silver nanofibers makes them difficult to find with the used SEM. The three different base materials can be clearly identified from Fig. 3(a) and 3(d) by their distinct interactions with the electron beam. The introduction of the glass nanofibers can be seen in Figs. 3(b) and 3(e) to fill the voids left by the microfibers, which can be attributed to increase the particle interception efficiency. Lastly, in Figs. 3(c) and 3(f), the silver coating can be seen to be distributed homogeneously, at least in the lateral direction.

Performance of the Filter Functionality

The methanol adsorption isotherm at 30°C as a function of the relative pressure can be seen in Fig. 4. The values of adsorbed amounts are similar to those reported by Kumita *et al.* (2017). The amount adsorbed here is related to the mass of ACF in the filter media. The measurements show that the inclusion of other fibers in the filter does not inhibit the adsorption potential of ACF when compared to the bulk material. This means that the amount of ACF can be tailored to suit a specific need.

Particle penetration through filters F0, F1 and F2 are presented in Fig. 5(a). The face velocity during the measurements was kept at 3.8 cm s^{-1}. By introducing glass nanofibers into the filter media, a clear reduction can be seen in the penetration, as is to be expected. However, substituting some of the glass nanofibers with silver nanofibers increases the penetration slightly. This is due to the reduction in the count of nanofibers in the filter media, caused by the higher density of silver compared to glass. In essence, the same mass of nanofibers contains less fibers overall. Theoretical particle penetration curves were calculated based on Eq. (2) with packing density values of 0.145, 0.277 and 0.311, and initial pressure drops of 4.5, 35.1 and 33.0 Pa for filters F0, F1 and F2 respectively. Additionally, the efficiency can be increased by stacking the prepared filter media, as is typically done. The quality factors for these filters are shown in Fig. 5(b). There is no significant improvement on the performance for nanoscale particles, as the increase of the collection efficiency has been achieved with the cost of increased pressure drop. For particle size ranges closer to a micrometer, the interception is increased significantly more, which can also be seen in the increase in the quality factor.

Antibacterial activity against *S. aureus* and *E. coli* is shown in Fig. 6, where an image set of agar plates covering the four test cases are displayed. In some of the test cases the handling and cutting of the filter media has resulted in loose fibers, which then can be seen on the agar plates. These should not be mistaken for bacterial growths. Averaged

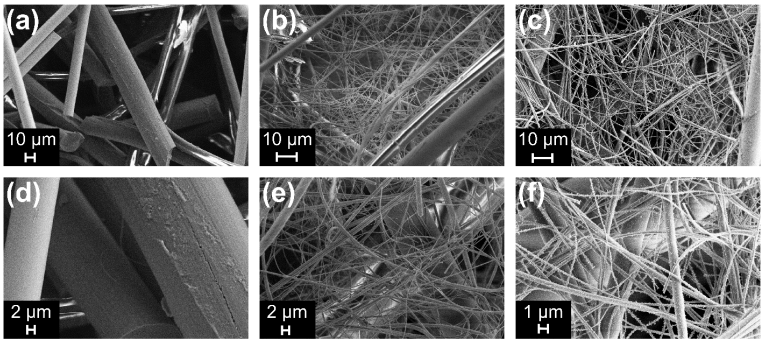

Fig. 3. SEM-micrographs from (a, d) F0, (b, e) F1 and (c, f) F3 filter materials, with two magnifications.

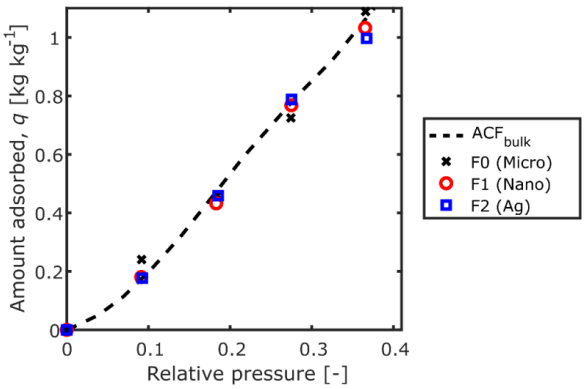

Fig. 4. Results from the methanol adsorption filter tests.

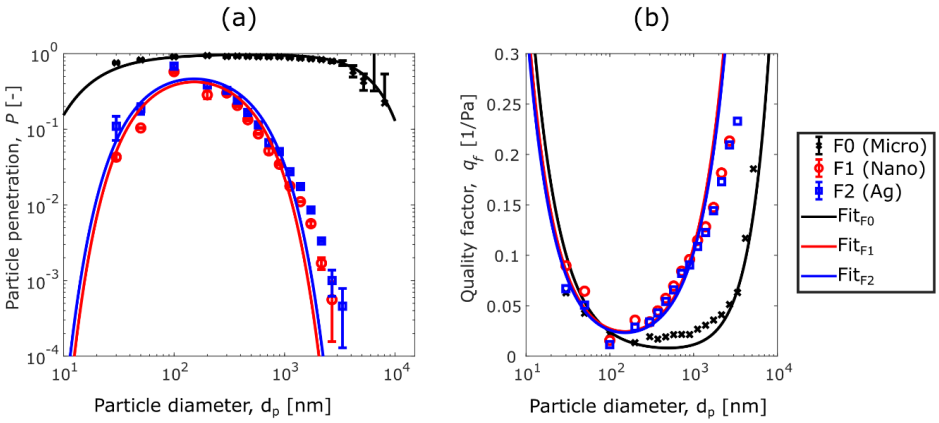

Fig. 5. Filtration performance of the prepared filters: (a) the particle penetration and (b) the quality factors.

set of data from the bacterial growths is shown in Fig. 7. In all of the cases, the bacterial growth was not inhibited by the F1 reference sample, but the addition of nanoscale silver can clearly be seen to increase the antibacterial activity. Both the silver nanofibers and nanoparticles are very effective against *E. coli*, effectively blocking the growth completely on all the studied cases. Minimal growth was found on one silver fiber containing filter after 24 h of incubation. *S. aureus*, on the other hand, is much more resistant against the silver present in the filters. Additionally, the silver particles were slightly more effective as an antibacterial additive in the filters when compared to the nanofibers. Relying on the measurements made in this work, it is difficult to say exactly what causes this disparity between these two materials. It could be their morphologies, being the most obvious difference, or the distribution of silver inside the filter media. In either case, more measurements would be needed to reveal the actual mechanism. Overall, the comparable activity of these materials is probably due to the same mass loading of silver in the filter media. In the work of Gunell *et al.* (2017), the amount of silver needed to inhibit the growth of these same bacteria was studied, and based on their results, by increasing the amount of silver in the filter media of this work, the growth of *S. aureus* could also be suppressed.

CONCLUSIONS

Antibacterial fiber filters containing activated carbon fibers were fabricated using nanoscale silver and tested for particle penetration, methanol adsorption and bacterial growth inhibition. The silver was introduced into the filter media either during the filter fabrication process as silver nanofiber content or after the filter fabrication process as an LFS-generated nanoparticle coating. The performance in terms of particle penetration and methanol adsorption agreed well with the theory and bulk reference, respectively, despite the filter media consisting of mixed materials. Antibacterial activity was successfully generated by both methods. However, the silver nanofibers showed slightly higher activity than the nanoparticles, which cannot be attributed to inconsistent mass loading of the silver between the filter media, as the coating process was monitored rigorously with a wide range of instruments to prevent

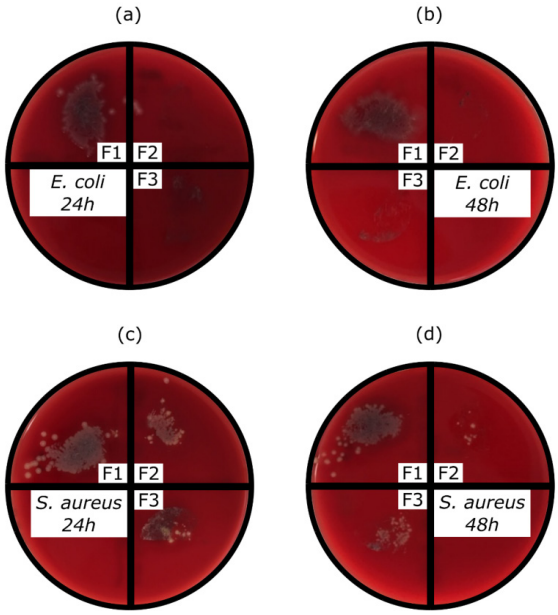

Fig. 6. Images of all four test cases: (a) *E. coli* (24 h), (b) *E. coli* (48 h), (c) *S. aureus* (24 h) and (d) *S. aureus* (48 h), which show the bacterial growths for the reference filter (F1) and the two antibacterial filters (F2 and F3).

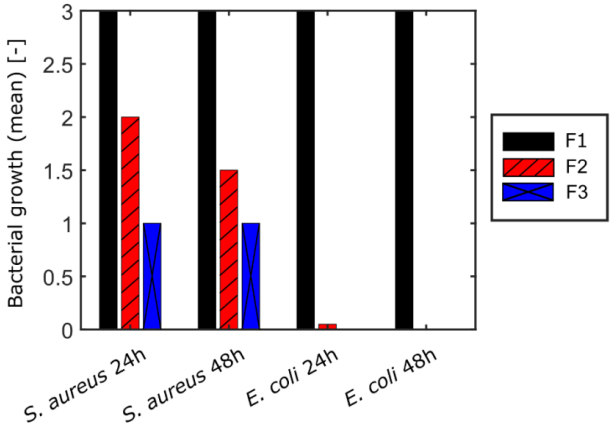

Fig. 7. The overall antibacterial activity of the prepared filter materials.

such a discrepancy. Regardless, with either method, the resultant antibacterial filters can be tuned to specific needs by adjusting the thickness of the filter or the mass fraction of added ACF or silver. Furthermore, the coating process can be applied to existing filters that are already in use, for example, in HVAC systems, which would be the next logical step.

ACKNOWLEDGMENTS

Paxton Juuti acknowledges TUT's graduate school and the Emil Aaltonen Foundation for financial support. The authors would also like to thank Miki Tavast for the QCM-MOUDI and Dr. Mari Honkanen for the SEM imaging.

REFERENCES

Brobbey, K., Haapanen, J., Gunell, M., Mäkelä, J., Eerola, E., Toivakka, M. and Saarinen, J. (2017). One-step flame synthesis of silver nanoparticles for roll-to-roll production of antibacterial paper. *Appl. Surf. Sci.* 420: 558–565.

Choi, H.J., Kumita, M., Hayashi, S., Yuasa, H., Kamiyama, M., Seto, T., Tsai, C.J. and Otani, Y. (2017).

Filtration properties of nanofiber/microfiber mixed filter and prediction of its performance. *Aerosol Air Qual. Res.* 17: 1052–1062.

Daisey, J., Angell, W. and Apte, M. (2003). Indoor air quality, ventilation and health symptoms in schools: An analysis of existing information. *Indoor Air* 13: 53–64.

Forthomme, A., Joubert, A., Andrès, Y., Simon, X., Duquenne, P., Bemer, D. and Coq, L.L. (2014). Microbial aerosol filtration: Growth and release of a bacteria-fungi consortium collected by fibrous filters in different operating conditions. *J. Aerosol Sci.* 72: 32–46.

Gordon, T., Perlstein, B., Houbara, O., Felner, I., Banin, E. and Margel, S. (2011). Synthesis and characterization of zinc/iron oxide composite nanoparticles and their antibacterial properties. *Colloids Surf., A* 374: 1–8.

Gunell, M., Haapanen, J., Brobbey, K., Saarinen, J., Toivakka, M., Mäkelä, J.M., Huovinen, P. and Eerola, E. (2017). Antimicrobial characterization of silver nanoparticle-coated surfaces by "touch test" method. *Nanotechnol. Sci. Appl.*10: 137–145.

Haapanen, J., Aromaa, M., Teisala, H., Juuti, P., Tuominen, M., Sillanpää, M., Stepien, M., Saarinen, J.J., Toivakka, M., Kuusipalo, J. and Mäkelä, J. (2018). On the limit of superhydrophobicity: Defining the minimum amount of TiO_2 nanoparticle coating. *Mater. Res. Express* 14: 035004.

Harra, J., Kujanpää, S., Haapanen, J., Juuti, P., Mäkelä, J. M., Hyvärinen, L. and Honkanen, M. (2017). Aerosol analysis of residual and nanoparticle fractions from spray pyrolysis of poorly volatile precursors. *AIChE J.* 63: 881–892.

Hassan, I., Parkin, I., Nair, S. and Carmalt, C. (2014). Antimicrobial activity if copper and copper(I) oxide thin films deposited via aerosol-assisted CVD. *J. Mater. Chem. B* 2: 2855.

Jones, A. (1999). Indoor air quality and health. *Atmos. Environ.* 33:4535–4564.

Jung, J., Hwang, G., Lee, J. and Bae, G. (2011). Preparation of airborne Ag/CNT hybrid nanoparticles using an aerosol process and their application to antimicrobial air filtration. *Langmuir* 27: 10256–10264.

Juuti, P., Arffman, A., Rostedt, A., Harra, J., Mäkelä, J. and Keskinen, J. (2016). Real-time effective density monitor (DENSMO) for aerosol nanoparticle production. *Aerosol Sci. Technol.* 50:487–496.

Juuti, P., Haapanen, J., Stenroos, C., Niemelä-Anttonen, H., Harra, J., Koivuluoto, H., Teisala, H., Lahti, J., Tuominen, M., Kuusipalo, J., Vuoristo, P. and Mäkelä, J.M. (2017). Achieving a slippery, liquid-infused porous surface with anti-icing properties by direct deposition of flame synthesized aerosol nanoparticles on a thermally fragile substrate. *Appl. Phys. Lett.* 110*:* 161603.

Kulkarni, P., Baron, P. and Willeke, K. (2011). *Aerosol measurement: Principles, techniques, and applications.* Wiley.

Kumita, M., Yamawaki, N., Shinohara, K., Higashi, H., Kodama, A., Kobayashi, N., Seto, T. and Otani, Y. (2018). Methanol adsorption behaviors of compression-molded activated carbon fiber with PTFE. *Int. J. Refrig.* 94: 127–135.

Mäkelä, J.M., Haapanen, J., Harra, J., Juuti, P. and Kujanpää, S. (2017). Liquid flame spray - A hydrogen-oxygen flame based method for nanoparticle synthesis and functional nanocoatings. *Kona Powder Part. J.* 34: 141–154.

Möritz, M., Peters, H., Nipko, B. and Rüden, H. (2001). Capability of air filters to retain airborne bacteria and molds in heating, ventilating and air-conditioning (HVAC) systems. *Int. J. Hyg. Environ. Health* 203: 401–409.

Oya, A., Yoshida, S., Abe, Y., Itzuka, T. and Makiyama, N. (1993). Antibacterial activated carbon fiber derived from phenolic resin containing silver nitrate. *Carbon* 32: 71–73.

Rumchev, K.B., Spickett, J.T., Bulsara, M.K., Phillips, M.R. and Stick, S.M. (2002). Domestic exposure to formaldehyde significantly increases the risk of asthma in young children. *Eur. Respir J.* 20: 403–408.

Saad, S. (2003). Integrated environmental management for hospitals. *Indoor Built Environ.* 12: 93–98.

Sorvali, M., Vuori, L., Pudas, M., Haapanen, J., Mahlberg, R., Ronkainen, H., Honkanen, M., Valden, M. and Mäkelä, J.M. (2018). Fabrication of ultrathin multilayered superomniphobic nanocoatings by liquid flame spray, atomic layer deposition, and silanization. *Nanotechnology* 29:185708.

Sotiriou, G. and Pratsinis, S. (2010). Antibacterial activity of nanosilver ions and particles. *Environ. Sci. Technol.* 44: 5649–5654.

Teisala, H., Geyer, F., Haapanen, J., Juuti, P., Mäkelä, J.M., Vollmer, D. and Butt, H.J. (2018). Ultrafast processing of hierarchical nanotexture for a transparent superamphiphobic coating with extremely low roll-off angle and high impalement pressure. *Adv. Mater.* 30: 1706529.

Tikkanen, J., Gross, K., Berndt, C., Pitkänen, A., Keskinen, J., Raghu, S., Rajala, M. and Karthikeyan, J. (1997). Characteristics of the liquid spray process. *Surf. Coat. Technol.* 90: 210–216.

Yoon, K., Byeon, J., Park, C. and Hwang, J. (2008). Antimicrobial effect of silver particles on bacterial contamination of activated carbon fibers. *Environ. Sci. Technol.* 42: 1251–1255.

Received for review, December 21, 2018
Revised, April 25, 2019
Accepted, June 24, 2019